UC Berkeley
UC Berkeley Electronic Theses and Dissertations

Title
Micro Chemical Vapor Deposition for the Synthesis of Nanomaterials

Permalink
https://escholarship.org/uc/item/2cj533b6

Author
Zhou, Qin

Publication Date
2011

Peer reviewed|Thesis/dissertation

eScholarship.org Powered by the California Digital Library
University of California

Micro Chemical Vapor Deposition for the Synthesis of Nanomaterials

by

Qin Zhou

A dissertation submitted in partial satisfaction of the

requirements of the degree of

Doctor of Philosophy

in

Engineering - Mechanical Engineering

in the

Graduate Division

of the

University of California, Berkeley

Committee in charge:

Professor Liwei Lin, Chair

Professor Albert P. Pisano

Professor Ali Javey

Fall 2011

Micro Chemical Vapor Deposition for the Synthesis of Nanomaterials

Copyright 2011

Qin Zhou

Abstract

Micro Chemical Vapor Deposition for the Synthesis of Nanomaterials

by

Qin Zhou

Doctor of Philosophy in Engineering - Mechanical Engineering
University of California, Berkeley

Professor Liwei Lin, Chair

MEMS (Microelectromechanical Systems) technologies have enabled the construction of a micro chemical vapor deposition (μCVD) system for the synthesis of nanomaterials. By means of localized resistive heating via micro-heaters, unique capabilities of the μCVD systems have been utilized to synthesize carbon nanotubes and graphene in this work, including fast stabilization of temperature; rapid exchange of gas species; laminar gas flow due to small Reynolds number; small diffusion length; and enhanced mass transport.

In the prototype designs, the μCVD system is composed of a suspended microheater and two contact pads constructed from the device layer of a SOI (silicon-on-insulator) substrate. Both heat transfer and fluidic analyses have been conducted to validate and optimize the key features of the system. Experimental results in the synthesis of single-walled carbon nanotubes (SWNTs) have shown that amorphous carbon formation can be deterred and ultra-long SWNTs can be grown using ethylene as the source gas using μCVD system while similar experimental conditions failed to produce SWNTs in a conventional CVD system.

Further applications of the μCVD system have been successfully demonstrated, including direct placement of high-quality, well-aligned SWNTs on temperature sensitive substrates such as thin paper or polymer sheets, and the synthesis of two-dimensional crystalline graphene structure with good uniformity. Specifically, the construction of high-performance CNT-based devices requires high-quality CNTs while conventional transfer and assembly processes often alter and degrade their properties. The localized heating of μCVD allows the direct synthesis of self-aligned SWNTs onto flexible substrates without causing thermal damages. Both Raman spectral and transmission electron microscopy have been used to validate the quality of these SWNTs. This methodology of direct synthesis of nanomaterials could be applicable to other one-dimensional nanostructures for various applications including flexible electronics. In the application to graphene growth, large area graphene with consistent number of layers has been realized on top of a nickel-coated micro platform using the μCVD system. The capability of ultra-fast heating and cooling provided by the MEMS platform is crucial for the successful growth of graphene. In the prototype graphene synthesis experiments, methane is flowed at 1.5% volume ratio with hydrogen to the platform heated to 1000℃ and the heating power is cut off after a 5-min growth process. It has been demonstrated that 1~2 layers of graphene structures can be consistently grown throughout the whole 300×300 m^2 platform.

A man should look for what is, and not for what he thinks should be.

- *Albert Einstein*

Acknowledgements

I would like to thank my research advisor Professor Liwei Lin for introducing me to the field of Micro Electromechanical Systems and Nanomaterials. He gave me all kinds of freedom and encouragement which made my Ph.D. program a smooth and enjoyable one. Several other professors have contributed graciously their time and wisdom on my behalf, including Professor Ali Javey, Professor Feng Wang, Professor Costas Grigoropoulos, Professor Joel Moore, and Professor Dorian Liepmann. I also thank UC Berkeley Microelectronics Laboratory stuff and members for their kind help on the microfabrication. Mick Franssen and Gordon Long in the Mechanical Engineering Student Machine Shop guided me in mechanical machining process. I would also like to thank the following people for their help: Jiming Huang, Baisong Geng, Kaihui Liu, Yingqi Jiang, Ryan Yang, Peter Yang, Armon Mahajerin, Kevin Limkrailassiri, Kedar Shah, Qian Cheng, Shaomin Xiong, Jinglin Zheng, Liang Pan, Jie Yao, Kailiang Huang and Nathan Doornenbal. I would also like to thank the entity that is the University of California at Berkeley which has exposed me to so many different ideas, cultures, opportunities, and resources. Finally I have to thank my parents and my wife for their love and support. The work is partially funded by DARPA and NSF.

Contents

List of Figures v
List of Tables vii
Chapter 1 Introduction 1
1.1 Nanomaterials 1
1.2 Chemical Vapor Deposition 1
1.3 Synthesis of Nanomaterials by Chemical Vapor Deposition 2
1.4 Miniaturization of the Chemical Vapor Deposition System 2
1.5 Dissertation Goals and Structure 3
Chapter 2 Operation Principles and Experimental Setup 6
2.1 Theoretical Analyses 6
2.1.1 Transient Temperature Responses 6
2.1.2 Gas Species Exchange Time 8
2.1.3 Flow Pattern 9
2.1.4 Mass Transport 12
2.2 Design of the μCVD growth chip 14
2.2.1 Folded beam supported platform 14
2.2.2 U-shaped cantilever with embedded microchannels (Type I) 17
2.2.3 Microheater with square-shape platform (Type II) 23
2.3 Fabrication Process of μCVD growth chips 23
2.4 System Architecture and Assembly 28
2.4.1 System Architecture 28
2.4.2 Temperature Monitoring System 28
2.4.3 Electrical Interface and Computer Control 31
Chapter 3 Application Demonstrations of μCVD 33
3.1 Carbon Nanotube Synthesis with Enhanced Mass Transport 33
3.1.1 Introduction 33
3.1.2 Experiments 34
3.1.3 Results and discussion 34
3.2 Direct Growth of Aligned SWNTs on Temperature Sensitive Substrates 36
3.2.1 Introduction 36
3.2.2 Experimental setup 37
3.2.3 SWNT growth procedure 38

3.2.4 Characterization of the as-grown SWNTs 38
3.2.5 Direct growth of SWNTs on temperature sensitive substrates 40
3.3 Uniform Graphene Synthesis with Controlled Layer Number 42
3.3.1 Introduction 42
3.3.2 Experiments 44
3.3.3 Characterization of Synthesized Graphene 45
3.3.4 Discussion 46
Chapter 4 Conclusions and Future Directions 48
4.1 Conclusions 48
4.2 Future Directions 48
4.2.1 Patternize carbon nanotubes 48
4.2.2 The interaction of carbon nanotube and the substrate 49
4.2.3 Relationship between nanotube diameter and growth temperature 50
Appendix A Mechanical Assembly for μCVD system 52
A.1 μCVD Chip Holder and Electrical Interface 52
A.2 Gas Interface 52
A.3 Mechanical Assembly of Nanopositioner 55
A.4 Optical Monitoring Glasses 56
Appendix B Design of the Temperature Monitoring System 57
B.1 Optical Design 57
B.1.1 Direct coupling 57
B.1.2 Optical fiber coupling 61
B.1.3 Adding a lens to regulate light path 61
B.2 Photodetector and the Amplifying Circuit 62
B.2.1 Silicon detector 63
B.2.2 PbS detector 64
B.3 System Calibration 66
Appendix C Signal Processing and Computer Control 67
C.1 General Description of the Construction 67
C.2 AD/DA Module 67
C.3 Signal Amplification and Conditioning Module 68
C.4 Temperature Control Program 69
C.5 Nanopositioner and Its Control Program 71
Bibliography 72

List of Figures

Figure 1.1: Goals of this dissertation. 4
Figure 2.1: ANSYS® simulation on the temperature responses of a typical μCVD chip. 7
Figure 2.2: Simulated temperature responses vs. time for the μCVD system. 8
Figure 2.3: Curly carbon nanotubes indicating the existence of gas flow turbulence. 10
Figure 2.4: Schematic cross-sectional view showing the setup to regulate the gas flow in the vicinity of the μCVD micro heater. 10
Figure 2.5: Optical image of the experimental setup. 11
Figure 2.6: A SEM picture showing experimental growth results of CNTs from μCVD when a quartz cap is applied (top view). 11
Figure 2.7: Mass transport during a CVD process 12
Figure 2.8: The mass transport of a CVD process can be enhanced by miniaturization 13
Figure 2.9: Heater and gas channels design 14
Figure 2.10: Fabricated μCVD chip 15
Figure 2.11: Expected and actual temperature distribution 16
Figure 2.12: Simulated temperature distribution when the heat conduction through 1-μm-thick gas layer is neglected. 16
Figure 2.13: Simulated temperature distribution when heat conduction through the 1-μm-thick gas layer is considered. 17
Figure 2.14: U-shaped cantilever as the heating platform with embedded microchannels. 18
Figure 2.15: Simulated temperature distribution for the U-shaped cantilever heating platform. 18
Figure 2.16: Calibration of the emissivity of the μCVD chip surface. 19
Figure 2.17: Temperature analysis of the μCVD system. 21
Figure 2.18: Gas flow simulations 22
Figure 2.19: A scanning electron microscopic picture showing the fabricated μCVD chip for graphene synthesis. 23
Figure 2.20: Typical fabrication process of a μCVD chip.. 26
Figure 2.21: The scanning electron microscope (SEM) image of a fabricated μCVD array with several μCVD units. 27
Figure 2.22: The system architecture. 28
Figure 2.23: A typical I-V curve from a silicon heater. 29
Figure 2.24: Measured signal strength ratio of Si to PbS detector. 31
Figure 2.25: The electrical interface for μCVD system. 32
Figure 3.1: SEM images showing growth results. 35
Figure 3.2: SWNTs synthesized from μCVD and conventional CVD. 36
Figure 3.3: Schematic diagram illustrating the direct synthesis of self-aligned SWNTs onto an arbitrary substrate.. 38
Figure 3.4: Characterizations of the synthesized SWNTs by μCVD. 39
Figure 3.5: Direct growth of SWNTs on paper and plastic substrates 41
Figure 3.6: A SEM photo showing aligned nanotubes deposited on the top glass substrate. 42
Figure 3.7: The basic concept of graphene synthesis using μCVD. 44
Figure 3.8: Fabrication Process of a μCVD chip for graphene synthesis. 44

Figure 3.9: Raman spectra analyses.. 46
Figure 4.1: The concept of direct writing carbon nanotubes. 49
Figure 4.2: Utilizing μCVD for the study of nanotube-substrate interaction. 50
Figure 4.3: Studying the relation between the CNT diameter and the growth temperature using μCVD. 51
Figure A.1: The assembly of μCVD chip on its chip holder. 52
Figure A.2: Gas flow control diagram. 53
Figure A.3: Direct coupling to reduce the space between the μCVD chip and mainstream gas flow. 54
Figure A.4: Gas control system diagram and an optical photo of the home-built system. 55
Figure A.5: The assembly drawing of the nanopositioner. 56
Figure A.6: Assembly drawing of the top cover of the vacuum chamber. 57
Figure B.1: Schematics of direct coupling. 58
Figure B.2: The sensitive region of PbS detector in relative to a 1000 ℃ black body radiation spectrum 59
Figure B.3: Response curve for PbS detector. 60
Figure B.4: Schematics of adding a lens for light coupling. 61
Figure B.5: Analysis on how much energy is coupled into the optical fiber. 62
Figure B.6: Spectral response of the photodetectors. 63
Figure B.7: Schematic circuits for silicon detector. 63
Figure B.8: Measure dark resistance to acquire the temperature of PbS detector and the corresponding sensitivity. 65
Figure B.9: Amplifying circuits for PbS detector. 66
Figure B.10: Setup for optical temperature measuring system calibration. 67
Figure C.1: The schematic circuits for signal amplification and conditioning. 69
Figure C.2: Schematic of the temperature control program. 70
Figure C.3: Control program user interface 70
Figure C.4: Nanopositioner control program flow chart. 71
Figure C.5: The user interface for nanopositioner control program. 72

List of Tables

Table 2.1: Radiation intensity at different wavelength λ according to Plank's law. 30
Table B.1: Calibrated Si / PbS detector signal ratio (R_{vi}) v.s. temperature. 67

Chapter 1

Introduction

1.1 Nanomaterials

Nanomaterials received extensive research activities in the last twenty years [1-9]. The main interest lies in the vastly increased surface-to-volume ratio of these materials, which makes new quantum mechanical effects possible. For example, the electronic band structure of nanomaterials can be significantly different from their macro-scale counterparts due to quantum confinement [3-5, 10-12]. These emerged properties offer possibilities of new applications.

Carbon based nanomaterials, such as carbon nanotubes (CNTs) [13-17] and graphene [18-22], received probably the highest attention among the nanomaterials. Single-walled carbon nanotubes (SWNTs), rolled up from a single layer of graphene, are highly confined in the radial direction and are an ideal 1-dimensional material for condensed matter physics research [23-29]. CNTs later also found applications in electronics [30-34], sensors [35-37], display [38-40], and drug delivery [41-44]. Following CNTs, Graphene was discovered later in 2004, where a simple handcrafted “scotch tape method” was used [18]. Graphene is the only one-atom-thick material discovered to exist stably in nature up till today. Its unique properties such as massless-Dirac-fermion-like electron transport [19] and room temperature quantum hall effect [45, 46] have also drawn huge research activities. Application wise, graphene can be made into high-speed amplifiers[47], photodetectors [48], single-molecule sensors [49], and transparent electrodes[50].

Each type of nanomaterials has its own synthesis methods. Some of them could be directly obtained from chemical reactions by mixing chemical solutions[51, 52], while others need much more sophisticated methods such as laser ablation [53]. Among the synthesis methods, chemical vapor deposition (CVD) is easy to control, of low-cost, and produces consistent synthesis results [54, 55]. This method is also widely applied in the growth of CNTs [56] and graphene [54].

1.2 Chemical Vapor Deposition

Chemical vapor deposition (CVD) has been widely used in microfabrication processes to produce thin films and has been an important method in the synthesis of various nanostructures [2, 57, 58]. Usually chemical constituents are heated in the vapor phase with appropriate temperature to activate chemical reactions. The thermal decomposition or reaction of gaseous compounds becomes the key deposition sources. CVD requires knowledge from thermodynamics, kinetics, fluid dynamics, and chemistry. Some of these technological issues and principles are discussed in details throughout this dissertation as the foundations for the proposed work on “micro chemical vapor deposition.” For example, pressure and gas flow are important parameters affecting

thermodynamics on the deposition results. They affect mean free path of molecules and the mass transport rate. Another important factor is kinetics, which defines the mass transport process and determines the rate-control mechanism [59].

1.3 Synthesis of Nanomaterials by Chemical Vapor Deposition

Nanomaterials have attracted great research and commercial interests in the last twenty years for various applications and chemical vapor deposition has been one of the major methodologies in the synthesis of nanomaterials since equipment and processes for CVD have been well-developed in the semiconductor industry to grow different types of thin-films at low-cost, high productivity and high quality [60]. The earliest experiments of CVD-based nanostructure syntheses appeared not long after the commercialization of the transmission electron microscope (TEM) [61], which allowed the observation of synthesized nanomaterials [62]. Vapor-liquid-solid (VLS) growth mechanism was proposed and has since been believed as the major growth mechanism for many nanowires/nanotubes synthesized by CVD. For example, in the early CVD process for the synthesis of silicon nanowires, the chemicals in vapor phase are first introduced into the reaction chamber and heated (in this case H2 and SiCl4). Chemical reaction starts with or without the help of catalyst (Au). Reaction products are absorbed into the catalyst droplets which is in liquid phase (gold nanoparticle at 950 ℃) to cause supersaturation. The reaction products (silicon in this case) precipitate from the droplets to initiate the growth of nanotubes/nanowires in solid phase (silicon nanowires). The diameters of the nanotubes/nanowires are therefore strongly correlated to the size of the catalyst particles.

APCVD (Atmosphere Pressure Chemical Vapor Deposition) is easy to set up and does not require vacuum equipment such that it has been widely used in the synthesis of nanostructures. The process is usually performed by forcing the reactant gas to flow through a heated tube in a furnace. After entering into the tube, the gas temperature inside the tube gradually approaches external furnace temperature. CVD reaction takes place either with or without the assistance of catalyst. For example, carbon nanotubes (CNTs) have been previously synthesized with the assistance of iron nanoparticles with methane as the carbon source [63]. Its growth mechanism is generally considered to be the VLS growth mechanism [64]. The catalyst is usually prepared by reactions that generate nanoparticles in solution [63, 65] or by self-aggregation of thin films at high temperatures [66]. However, catalyst-free CNT growth has also been observed [67]. Catalyst-free synthesis is more commonly found for other materials. For example, a "Christmas tree" structure of PbS has been synthesized based on the so-called "screw dislocation" mechanism [68].

1.4 Miniaturization of the Chemical Vapor Deposition System

The behavior of a system can change considerably upon miniaturization. For example, the filament in an incandescent light cools down almost instantly after being turned off, while a pot of boiled water cools down much slower. This phenomenon is essentially due to the significantly smaller heat capacitance of the filament (See Section

2.1.1 for detailed analysis). The same rule applies to furnaces - a smaller furnace indicates a faster response in temperature.

The technologies of micromachining processes made it possible to shrink the large scale CVD systems to micro scale structures as micro CVD systems which could potentially bring new capabilities and innovations for the synthesis of nanomaterials. Miniaturized CVD was reported before for platinum deposition [69, 70]. It has also previously been used in the synthesis of nanomaterials [71-73] by our group. The preliminary works on miniaturization of CVD systems have shown that synthesized nanomaterials were usually low-quality with structural defects and inconsistency [72]. Miniaturization results in changes of various physical quantities and these differences could potentially offer unique advantages over the conventional CVD systems. For example, the heating power is drastically reduced with the possibility of local and selective depositions. As such, the synthesis process can occur in a room temperature chamber with a tiny heating zone which facilitates the possibility to install mechanical manipulators around the micro heating structures. Therefore, the deposited materials could be physically manipulated in-situ during the synthesis process for different applications. This is important because post assembly of nanomaterials often involves usages of various kinds of chemicals which could alter the properties of nanomaterials [74-76]. A miniaturized CVD system will also behave differently as compared to the macro-scale version in many aspects. Specifically, the heat capacity of micro heater scales down quickly with L3 in favor of fast temperature responses. The volume of the CVD chamber also scales down such that switching gases and purging chamber could be done almost instantaneously. Clearly, miniaturization results in unique properties to the CVD system which could lead to unprecedented material synthesis results.

1.5 Dissertation Goals and Structure

The goals of this dissertation are to realize μCVD systems with applications in the synthesis of nanomaterials by exploring the scaling effects. Gas flow, temperature distribution and chemical reaction processes within the μCVD systems are investigated and engineered for to improve the control and quality of nanomaterials. The major tasks of this dissertation are illustrated in Figure 1.1.

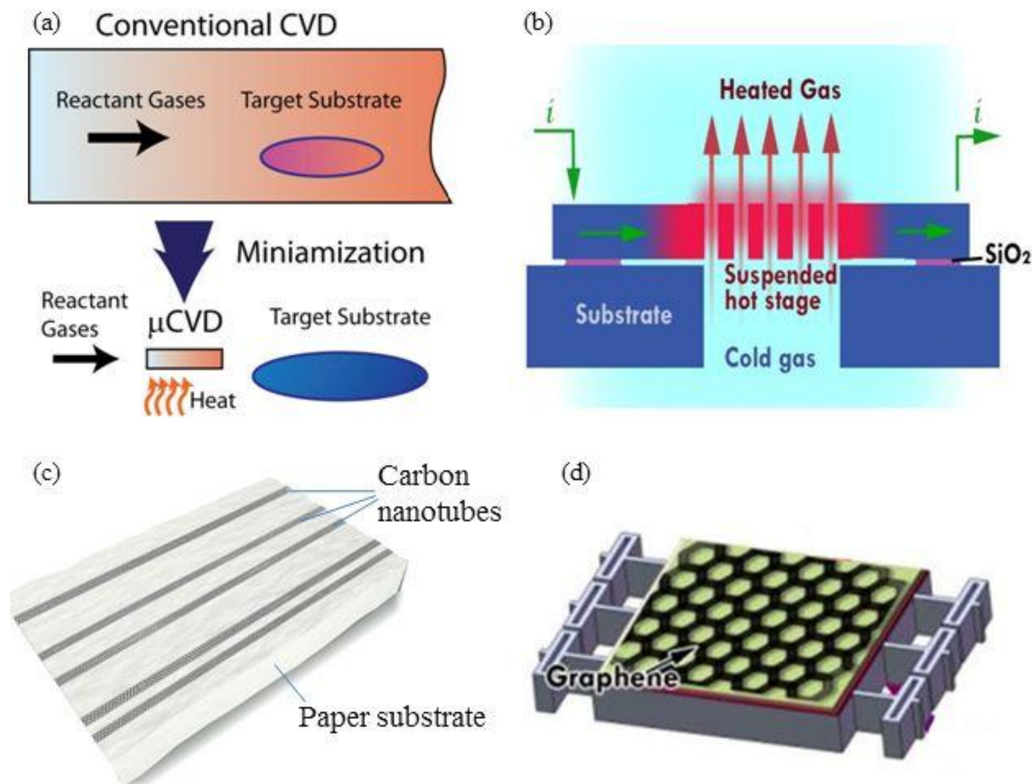

Figure 1.1: Goals of this dissertation. (a) The concept and operation principle of the μCVD system (Chapter 2). (b) Schematic cross sectional view showing a μCVD system fabricated on a SOI (Silicon-on-Insulator) substrate (Chapter 3). (c) Direct deposition of single-walled carbon nanotubes on temperature sensitive substrate via μCVD (Chapter 4). (d) Synthesis of graphene with nickel films on top of a μCVD system via μCVD (Chapter 4).

In Chapter 2, design, manufacturing and experimental setup of the μCVD system are described in details. The chapter begins with the theoretical foundation of the proposed work as illustrated in Figure 1.1(a). The scaling effects are analyzed and modeled with respect to four different important physical parameters/responses: transient temperature response, gas exchange time, flow pattern, and mass transport. The remaining chapter describes the design considerations include heat generation and gas flow control while the key microfabrication process involves deep-reactive-ion-etching of SOI substrates. Experimental setup of the μCVD system including mechanically fixtures, electrical connections, control loop and optical observation outfit is illustrated. A non-contact temperature monitoring system utilizing the spectrum shift of thermal radiation at different temperatures is used to measure the temperature of the μCVD growth chip.

Chapter 3 demonstrates several potential applications of the μCVD system, including successful quality improvement on synthesized SWNTs, aligned high quality SWNTs on temperature sensitive substrates, and the synthesis of graphene on top of nickel layer with fast cooling rate. These are some of the unique capabilities via the utilization of the μCVD system.

Chapter 4 concludes the research work and proposes possible future directions, including direct-write SWNTs onto a target substrate via in-situ mechanical manipulation

of the target substrate during the growth process, and exploring quantitative relationship between the SWNT diameter and growth temperature.

Chapter 2

Operation Principles and Experimental Setup

The micromachined μCVD system emulates the large-scale conventional CVD system by shrinking the large quartz tube to microchannels with diameters in tens of micrometers as illustrated in Fig. 1.1a. The gas is heated up to the CVD reaction temperature by heating up the microchannels via joule heating. Therefore, μCVD is like a miniaturized conventional CVD system with only tens of micrometers in length and several micrometers in diameter. The various effects coming from the size reduction are discussed in this chapter as well as the experimental setup.

2.1 Theoretical Analyses

2.1.1 Transient Temperature Responses

It usually takes several minutes to several hours for a common CVD system to warm up or cool down. By abruptly exposing the CVD chamber to the outside environment or by flowing cold gas into the chamber at a high rate, the cooling time constant can be reduced down to the order of ten seconds. It is difficult to further reduce the thermal time constant because of the system's large heat capacity. However, this difficulty can be overcome by shrinking down the size of the CVD system. A rough estimation on how the thermal time constant scales with system dimension is given as follows.

The system heat capacity, C_h, and the heat resistance, R_h, (heat resistance is the temperature difference between the CVD chamber and the environment divided by the heat flow) determines the system time constant as $\tau_h = R_h C_h$. The heat capacity of the system scales with volume or L^3, where L is the dimension of the system. The heat resistance, on the other hand, scales with L^{-1}. This is because the total heat flow:

$$Q = k \oint_{system} \mathbf{dA} \cdot \nabla T \sim \pi k L^2 (\Delta T / L) \propto \Delta T \cdot L \tag{2.1}$$

where A is the area of heat flow, k is thermal conductivity, T is temperature, and ΔT represents the temperature difference between the heating zone and the environment. The heat resistance is then $R_h = \Delta T/Q$ and scales with L^{-1}. The time constant of the system $\tau_h = R_h C_h$ should scale with L^2. Shrinking the conventional CVD system from macro scale (0.1~10 m) down to several hundred micrometers in dimension will result in an approximately 10^{-6} reduction of response time. This means that the system thermal time constant could go down from about tens of minutes to about one millisecond.

The quick temperature response of the small system implies the temperature of the system can be controlled to reach a certain temperature in a short amount of time, thus to avoid the undesired reactions which could happen at lower temperatures. For example, the synthesis of ZnO (Zinc Oxide) nanowires prefers fast temperature rise and fall to avoid the formation of ZnO thin film or micro-crystals at lower temperature [55]. However, the quick response also suggests that the temperature stability could be worse

than a macro-scale CVD system. Therefore a temperature monitoring and control system is necessary to regulate the synthesis temperature (See Section 2.4.2).

Efforts in simulations have been conducted on devices with real structural dimensions in finite element software such as ANSYS® to have better understanding of the transient responses. Figure 2.1 illustrate the temperature analyses from a μCVD system which has a suspended heating platform at the center and six stress-absorbing connectors to the substrate. Electrothermal analyses have been executed by applying a heating electrical current and the temperature distribution has been simulated as shown. If the heating power is suddenly cut off at time *t*=0, the temperature versus time curve is simulated as shown in Figure 2.2. It is found that the time constant of the μCVD system is about 1.3 ms, which corresponds to a cooling rate of about 0.8×10^{6} °C/s after the heating power is cut off.

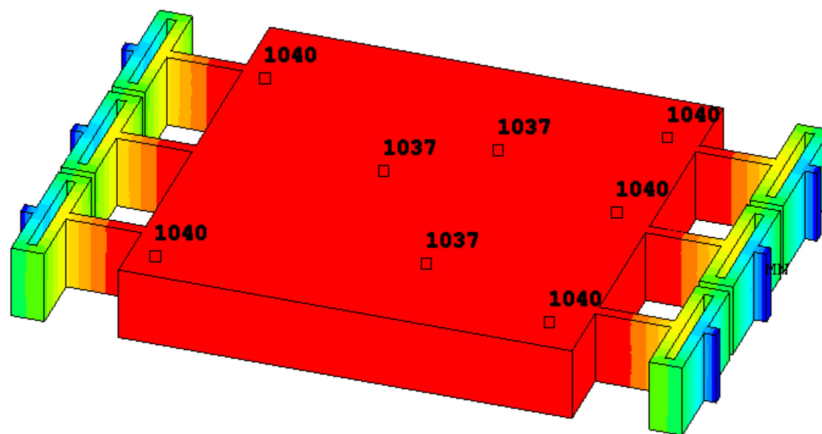

Figure 2.1: ANSYS® simulation on the temperature responses of a typical μCVD chip with relatively uniform temperature distribution on the heating platform at the center portion of the system. Temperature is shown in Celsius at several places of the platform. It is observed that the temperature variation is within 5 °C over the whole heating platform.

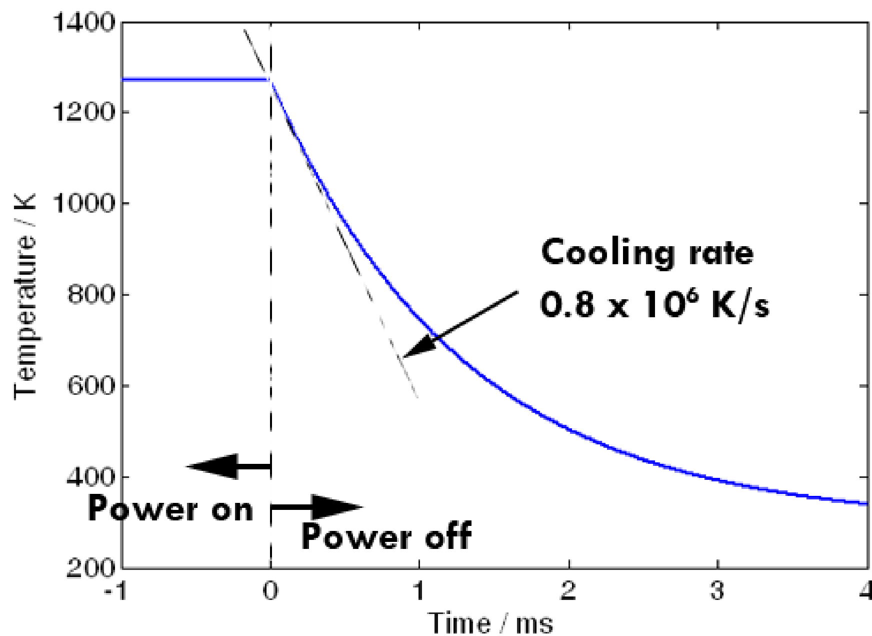

Figure 2.2: Simulated temperature responses vs. time for the μCVD system.

2.1.2 Gas Species Exchange Time

A CVD process usually involves flowing different gases at different stages of the process. For example, in the synthesis process for CNTs, carrier gases, such as argon, continue to flow during the heat-up process in the conventional furnaces. After the temperature is stabilized, the carrier gas is switched to the reactant gas such as methane. During the switching process, the gas concentrations continue to change as the concentration of the carrier gas drops and that of the reactant gas rises gradually. It is desirable to speed up this gas exchange process as it could affect the quality of the synthesis process when reactant gas of lower concentration starts to react prematurely. The time needed for the gas exchange period can be estimated by dividing the total volume of the reactant chamber by the flow rate of the gas. For example, the total volume of a conventional furnace used in our laboratory (5-feet long, 2-inch in diameter tube) is 0.003 m^3. If the gas flow rate is 1000sccm, the gas species exchange time is calculated in the order of minutes. This gas species exchange time is too long and it could affect the CNT synthesis process since CNTs can grow up to a few hundreds microns in length in just one minute [77].

On the other hand, the μCVD system could provide fast gas species exchange time because of the much reduced reaction chamber volume. Specifically, in the scaling analysis, the volume of the reaction chamber scales with L^3. Assuming the same gas flow speed (in the real experiment, the gas flow speed inside the microchannels are calculated to be ~ 1 m/s, on the same order of a conventional CVD system. See Section 2.2.2 for details), the flow rate scales with L^2 due to the reduction of the cross sectional area. Therefore, gas species exchange time should scale with L or about 10^{-4} reduction due to miniaturization in dimensions from the centimeter range of the conventional furnace to

the micrometer range of the μCVD system. In other words, the gas exchange process could be 10^4 faster and only takes several milliseconds.

2.1.3 Flow Pattern

In a CVD process, laminar flow is often preferred for a steady deposition environment. Reynolds number *Re* is often used to characterize different flow regimes and laminar flow in a tube requires $Re<2000$ [78]. For a conventional CVD system, the Reynolds number is estimated to be

$$Re = \frac{\rho v_m D}{\mu} = \frac{\rho Q D}{\mu A} \approx \frac{1\mathrm{Kg/m^3} \times 3000\mathrm{sccm} \times 0.05\mathrm{m}}{1 \times 10^{-5}\mathrm{Pa \cdot s} \times 0.002\mathrm{m^2}} = 125 \qquad (2.2)$$

where ρ is the gas density, v_m is the mean gas speed, μ is the gas viscosity, A is the tube cross sectional area, and D is the tube diameter. Here, the numbers are taken for methane in a 2-inch in diameter furnace nanotube synthesis experiments. It is noted that *Re* is in the regime of laminar flow. However, the flow will be disturbed as the gas entering the furnace tube and experiencing a heating process which could cause local turbulence[79].

Reynolds number inside the microchannels of a μCVD system, on the contrast, could be very small under the same flow speed. Putting $D = 5$ μm into Equation (2.2) with the other parameter unchanged, we get $Re = 0.0125$ (Notice that this calculation is for the gas flow inside the heated microchannels where nanomaterials are synthesized, not the guiding gas channels mentioned below). With a Reynolds number about 5 orders of magnitude smaller than the upper limit of laminar flow, there is plenty of space for adjusting the flow velocity to obtain the optimum synthesis results. Turbulence is no longer a threat to the CVD process. It is noted that the aforementioned discussions for gas flow in μCVD are only valid when the flow resides in the continuum flow region. For most synthesis processes, the mean free path of gas molecules under one atmospheric pressure is on the order of tens of nanometers, which is much smaller than the diameter of the proposed microchannel [80]. Therefore shrinking down the flow channel diameter is a valid approach for reducing Reynolds number and maintaining laminar flow inside the microchannels.

However, the gas flow could become turbulent after leaving the microchannels because of the sudden increase of *Re* due to the change of dimension. Although material synthesis only happens inside the microchannels, turbulence flow can affect the collection of the synthesized material in terms of bad alignment, curly shape, and entangled bundle. These phenomena are actually observed in experiments. As shown in Figure 2.3, the carbon nanotubes are curly because of the local turbulent flow which guides the nanotube orientation.

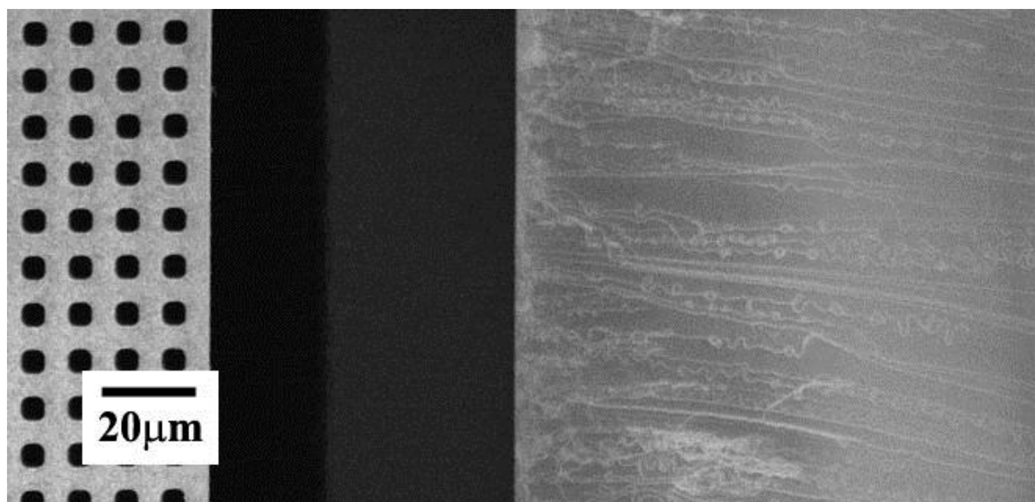

Figure 2.3: Curly carbon nanotubes indicating the existence of gas flow turbulence.

By adding a "cap" on the top of the μCVD chip as illustrated in Figure 2.4, one could extend the possible applications of the μCVD system. A flat-quartz plate is placed on top of the μCVD chip as the "cap", and the distance between them is controlled by the thickness of a slice of sticky tape which has a thickness of 50 μm in the prototype experiments. Figure 2.5 is an optical image of the setup and it is noted that there are 4 μCVD units in the prototype system and two slices of sticky tape are placed in parallel to support the quartz plate and to limit the flow directions. The steady laminar flow established in the microchannels (5 μm in diameter) built in the MEMS platform is extended to the 50-μm-gap region based on the first-order calculation of Reynolds number as follows:

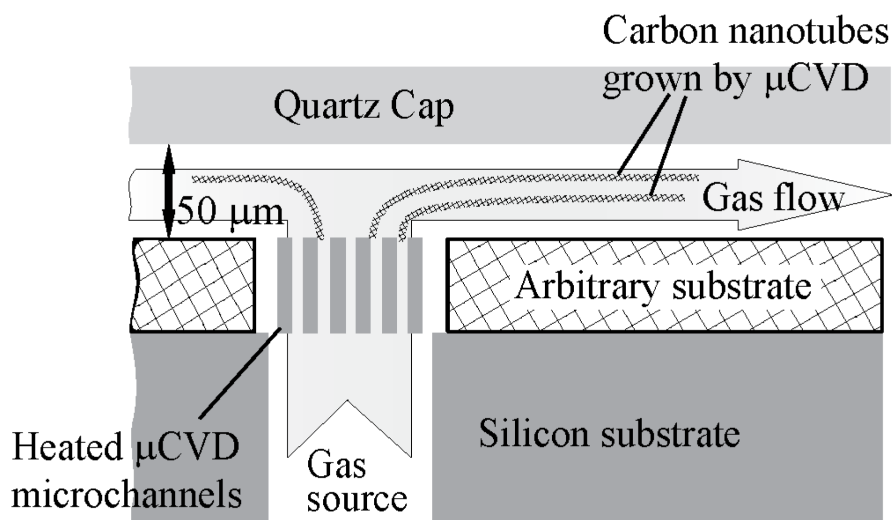

Figure 2.4: Schematic cross-sectional view showing the setup to regulate the gas flow in the vicinity of the μCVD micro heater. Source gas is supplied from the bottom side and passed through the microchannels. A quartz plate is placed on top with a separation gap of 50 μm. Lateral directional laminar flow is expected to guide the growth of CNTs.

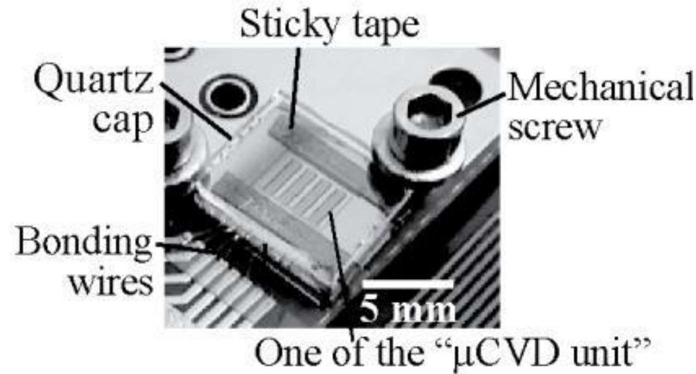

Figure 2.5: Optical image of the experimental setup.

The guiding gas channel between the glass cap and the μCVD system has the following cross sectional area:

$$A = 2 \times 50\ \mu\text{m} \times 4\ \text{mm} = 4 \times 10^{-7}\ \text{m}^2. \tag{2.3}$$

The width of the flow channel is the distance between the two slices of sticky tape, which is 4 mm. Since there are two outlets (left- and right-hand side outlets as can be identified in Figure 2.5), the total cross-sectional area is twice the single cross sectional area. The total gas flow rate applied in the experiment is F = 60 sccm such that the mean flow velocity v_m is:

$$v_m = F/A = 2.5\ \text{m/s}. \tag{2.4}$$

Reynolds number can be estimated by using characteristic length l as the height of flow channel of 50 μm, and the viscosity, μ, and mass density, ρ, are 9.8×10^{-6} Pa s and 1.178 kg/m^3 for ethylene, respectively.

$$\text{Re} = \frac{\rho v_m l}{\mu} = 15 \tag{2.5}$$

If the gas is hydrogen, the Reynolds number is even smaller (~1) because hydrogen has a much smaller mass density. Therefore, the Reynolds number for the guiding gas flow will be lower than 15 for CNT growth with a common recipe (e.g. using gas mixture of ethylene and hydrogen at 3:20 volume ratio). As a result, single-walled CNTs can be grown from inside the microchannels and extended outwards following the gas flow. At the end of the growth process, CNTs fall down onto the substrate in a well aligned fashion (Figure 2.6).

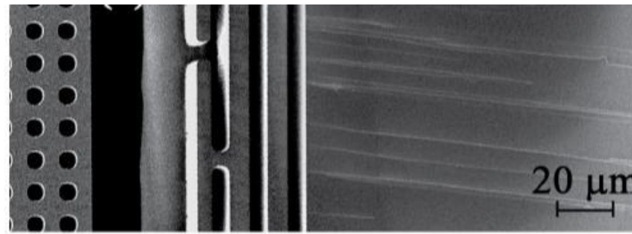

Figure 2.6: A SEM picture showing experimental growth results of CNTs from μCVD when a quartz cap is applied (top view). Curly CNTs are no longer observed and aligned CNTs are found on substrate due to stable laminar flow.

2.1.4 Mass Transport

A CVD reaction is essentially a chemical reaction, which is governed by thermodynamics to determine if the reaction will happen or not. Another equally important factor is the kinetics of the reaction or mass transport, which determines how the reactants reach the deposition surface and how the gaseous by-products are removed.

The sequence of events taking place during a CVD reaction is shown in Figure 2.7[60]. Basically, the reactant gases are first forced to flow into the reaction chamber. Laminar gas flow is usually maintained in the CVD process to ensure a steady reaction condition. As a result, gases have to diffuse through a boundary layer (a stagnant gas layer) to come to contact with the surface of substrate. Similarly, the gaseous by-products also have to diffuse through this boundary layer to leave the substrate. Therefore, the thickness of the boundary layer directly determines the mass transport efficiency. Thin boundary layer is preferred for gases to diffuse in and out.

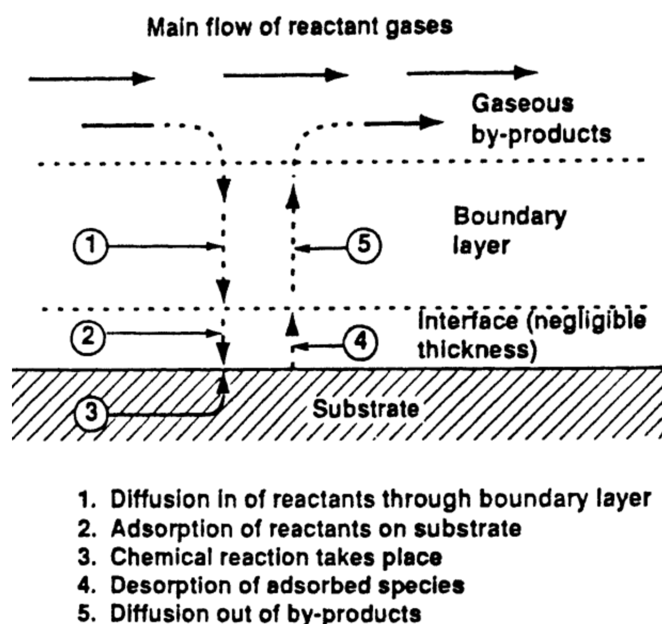

Figure 2.7: Mass transport during a CVD process (adopted from [60]).

Analytically, the thickness of the boundary layer can be expressed as:

$$\Delta \sim \sqrt{\frac{x\mu}{\rho v_m}} \tag{2.6}$$

where x is the distance calculated from the start of the inlet flow, μ is gas viscosity, ρ is gas mass density, and v_m is the mean flow velocity. It is noted that as flow velocity increases, the thickness of the boundary layer decreases which is in favor of mass transport. However, increasing flow velocity could result in turbulent gas flow and degrade the quality of the synthesis results.

It is possible to simultaneously enhance the mass transport and avoid turbulence using the micro chemical vapor deposition (μCVD) system as illustrated in Figure 2.8. Here,

the boundary layer is replaced as diffusion length because the velocity profile of a fully developed flow inside a tube with circular cross section is described by the parabolic velocity profile [81]:

$$v(r) = 2v_m \cdot \left[1 - \left(r / r_0\right)^2\right] \tag{2.7}$$

where r is the radial coordinate, v_m is the mean gas velocity and r_0 is the radius of the tube and it is difficult to define the boundary layer. The mass transport can be more accurately characterized by the diffusion length in this case. Similar to boundary layer, the diffusion length δ is the distance from the reaction surface to the convective gas stock, where gas can freely flow in and out. One way to reduce δ is to increase the velocity gradient (calculated in the direction perpendicular to the reaction surface) near the reaction surface, where flow streams with higher velocity are drawn closer to the reaction surface. The velocity gradient near the inner surface of the tube is:

$$\left.\frac{\partial v(r)}{\partial r}\right|_{r=r_0} = \frac{4v_m}{r_0} \tag{2.8}$$

It is noted in Equation (2.8) that the velocity gradient can be increased by either increasing v_m or reducing the tube radius. Specifically, if the microchannel diameter is 5 μm as compared to a 50 mm conventional quartz tube, a 10^4 increase in velocity gradient can be achieved under the same mean flow velocity. This large velocity gradient could significantly enhance mass transport.

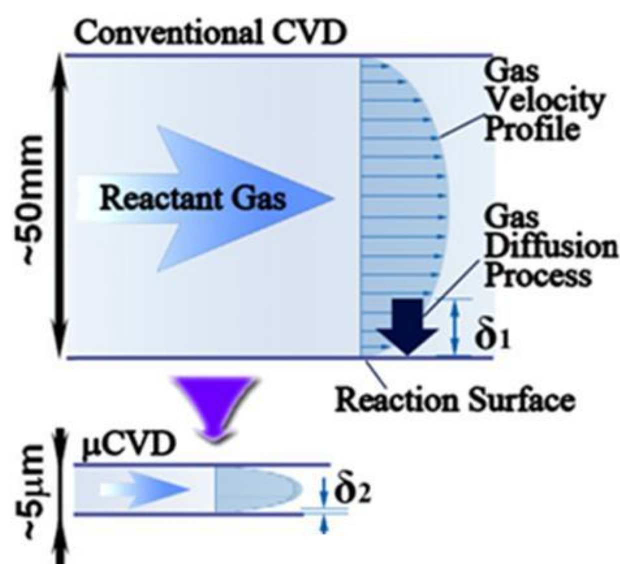

Figure 2.8: The mass transport of a CVD process can be enhanced by miniaturization which reduces the diffusion length δ.

The analysis in Section 2.1.3 and this section demonstrates that the mass transport of the μCVD system is significantly enhanced while the laminar flow condition is still preserved. This synthesis environment is applied in Section 3.1 because it is ideal for the synthesis of carbon nanotubes. More discussion on the mass transport based on the experimental results is found there.

2.2 Design of the µCVD growth chip

The µCVD growth chip is the core of the µCVD system in order to reach synthesis temperature as high as 1000 ℃ and relatively good gas flow control. Two major designs with different features have been implemented in this work for two different applications: (1) heating platform consisting of vertical microchannels for the synthesis of single-walled CNTs, and (2) heating platform with flat surface for the synthesis of graphene. Design and fabrication considerations of the µCVD growth chips are discussed in this section.

Microheaters have been demonstrated by MEMS (Microelectromechanical Systems) technologies many years ago [82-85]. The heat can be generated from joule heating by applying an electrical current through the heater. For example, micromachined polymerase chain reaction (PCR) [83, 85, 86] has utilized microheaters to initialize chemical reaction in micro reaction chambers. It is common to have suspended microheater to reduce the heat losses to the substrate such that the generated heat will not escape easily. This is because the gases (in this work, the working gases) have a much smaller thermal conductivity (~0.1 W/m·K) than silicon (~150 W/m·K). The suspension requires designs in the supporting beam structures as well as plans in the fabrication processes.

2.2.1 Folded beam supported platform

Figure 2.9 illustrates the cross sectional view of the prototype µCVD chip, consisting of a suspended heating stage with built-in vertical microchannels as the chemical reaction chambers. These microstructures are constructed on a SOI wafer. The prototype dimension of the microchannel is 5 µm in diameter and 50 µm in length. Reactant gas is introduced through the backside hole (100 µm in diameter and 400 µm in length) etched by a though-hole deep reactive-ion etching (DRIE) step. A scanning electron microscope (SEM) image of the device can be found in Figure 2.10. The central stage is supported by a pair of flexible beams anchored to the substrate. These beams also function as the electrical heaters to provide the heating power to the stage.

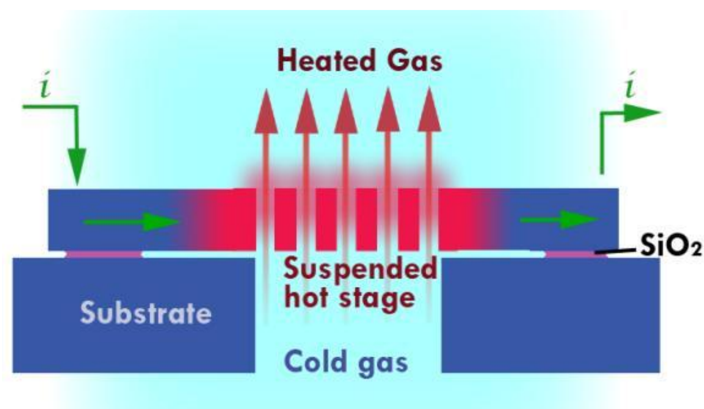

Figure 2.9: Heater and gas channels design (Cross sectional view).

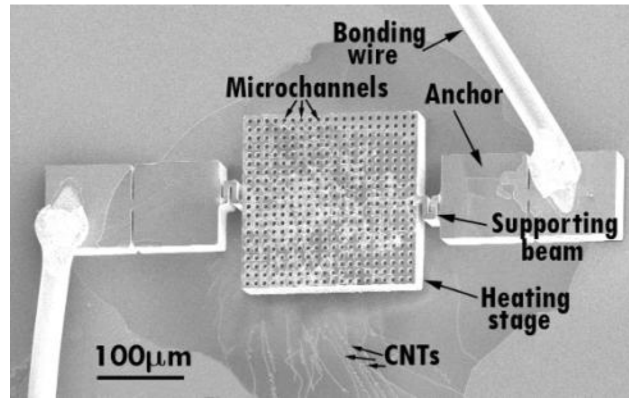

Figure 2.10: Fabricated μCVD chip (Top view).

The suspended heating platform is not fully sealed with the silicon substrate such that gases will leak from the sides of the heating platform. Severe leakage could change the pressure difference across the microchannels significantly and the analysis on gas flow could no longer be valid. Fortunately, the gap between the suspended platform and the supporting substrate is designed as 1 μm, which is smaller than the gas feeding lines whose dimension is at least several millimeters. As a result, its flow resistance (connected in parallel with the microchannels) is large and won't affect the approximation made in Section 2.1 that the measured pressure difference mainly coming from the pressure drop due to microchannels.

The first generation design can synthesize carbon nanotubes but it suffers from a serious heating problem. Heat is generated at the two supporting beams because of their relatively large electrical resistance and heat is dissipated through the two anchors. Therefore, the maximum temperature should occur around the center of the heating platform as illustrated in (Figure 2.11). A simulation is also performed to verify this design as shown in (Figure 2.12). However, experimental observations indicate that the supporting beams have the highest temperature while the center of the heating platform has a bit lower temperature up to hundreds of degrees Celsius. As a result, the supporting beams are easy to break due to high temperature damages. Heat loss through gases can usually be neglected in suspended heater design because the thermal conductivity of gases (~0.1 W/m·K) is orders of magnitude lower than the building material of heater (silicon, ~100 W/m·K). However, the heating platform has a relatively large area and the heat conduction through the gases is approximated as:

$$W = k_c A(T - T_0) / D \tag{2.9}$$

where k_c is the thermal conductivity of gases, A is the area of the heating platform, D is the distance between the suspended stage and the handling substrate (1 μm in this case), T is the temperature of the platform, and T_0 is the environment temperature. In the prototype experiment, $A = 0.03\times10^{-6}$ m^2, $T = 800$ °C, $T_0 = 25$ °C, and $k_c = 0.18$ W/m·K for hydrogen, it is found that $W \approx 4$ W. This number is close to the experimental input heating power. In other words, the central heating platform could be cooled by the gases such that it would be difficult to reach the growth temperature. A simulation is

conducted as shown in Figure 2.13 by counting the heat conduction of the heating platform to the bottom substrate. The results correspond well with the experimental observations. For example, the highest temperature is found to be at the supporting beams and the heating platform has lower temperature.

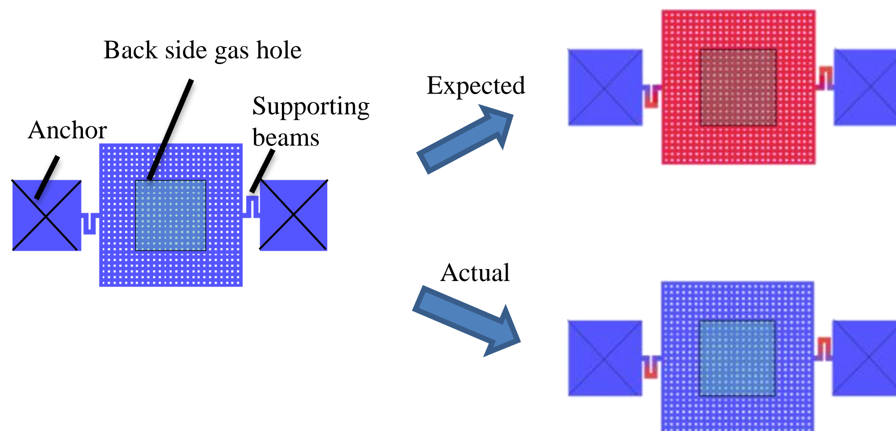

Figure 2.11: Expected and actual temperature distribution

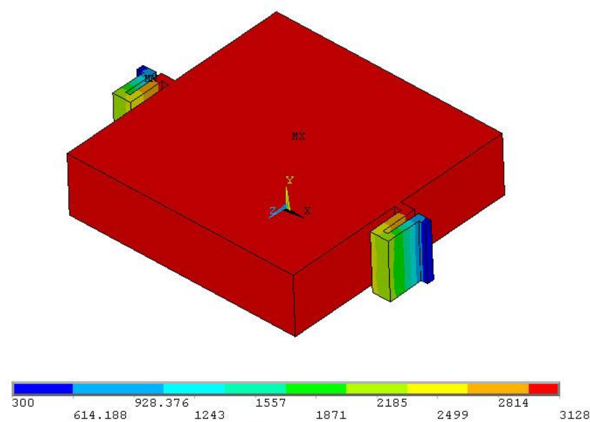

Figure 2.12: Simulated temperature distribution when the heat conduction through 1-µm-thick gas layer is neglected. The heat loss through gases is by forced convection is assumed to have a coefficient of 250 W/m^2K, which is the upper limit for typical convective heat transfer [78].

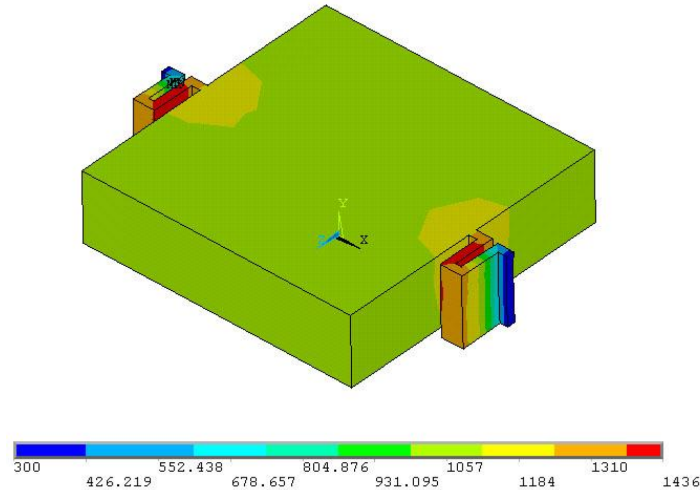

Figure 2.13: Simulated temperature distribution when heat conduction through the 1-μm-thick gas layer is considered. The temperature of the center platform has lower temperature than the maximum temperature of the system which is located at the supporting beams. This is consistent with experimental observations.

One way to circumvent this problem is to use a lower gas pressure to further reduce heat losses through the gas layer. However the thermal conductivity of gases would only be important if the heat dissipation distance is shorter than the mean free path of gas molecules [87]. The mean free path of gas molecules at one atmospheric pressure is only a few tens of nanometers. Therefore, the processing pressure for the μCVD system has to be significantly reduced (gas mean free path should be larger than 1 μm) to effectively block the heat conduction transfer via the gap between the heating plate and the substrate.

2.2.2 U-shaped cantilever with embedded microchannels (Type I)

One easy way to provide good thermal isolation is to open a hole from the backside of the substrate to the bottom of the heating platform for good heat insulation. Furthermore, a U-shaped cantilever heating platform as shown in Figure 2.14 is used to replace the first-generation heating platform with folded beam support. This design results in the highest temperature at the tip of the U-shape cantilever instead of supporting beams. In the prototype design, the cantilever is 1750 μm in length and 300 μm in width. The majority of the generated heat is dissipated by heat conduction through the anchors on the left hand side. As a result, the temperature distribution will have its maximum value at the tip of the cantilever. An electrothermal simulation is carried out as shown in Figure 2.15. Due to the extended length of the cantilever, its stiffness drops significantly. Therefore, 4 folded beams are designed to support the cantilever heating platform which improves its stiffness in vertical direction by 20 times as compared to the original design. The supporting beams can also tolerate structural deformation in the horizontal direction so that they will remain effective when the cantilever operates at high temperature with large thermal expansion.

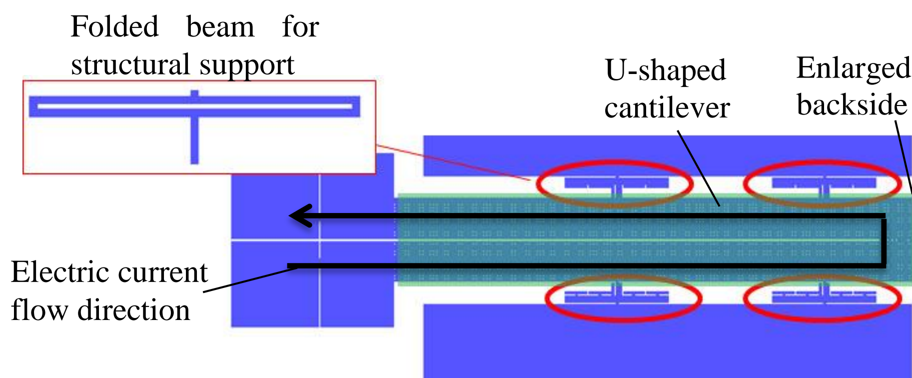

Figure 2.14: U-shaped cantilever as the heating platform with embedded microchannels.

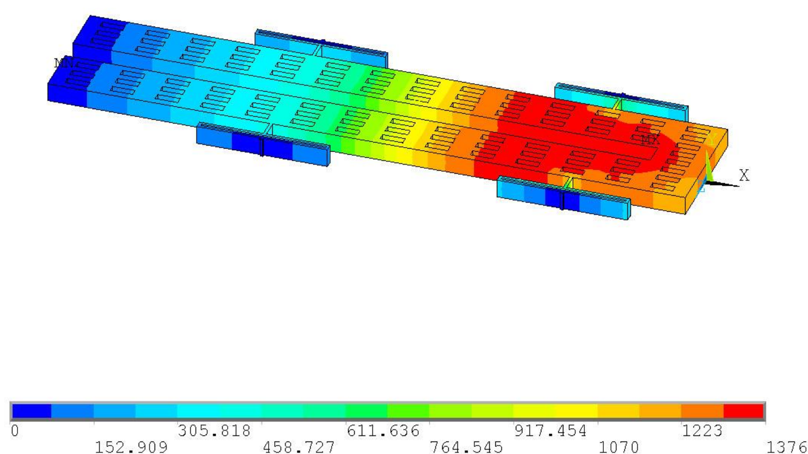

Figure 2.15: Simulated temperature distribution for the U-shaped cantilever heating platform. The simulation is done in ANSYS®.

The U-shaped cantilever heating platform design also results in localized heating. The high temperature region for the synthesis process is near the tip of the cantilever as illustrated in Figure 2.17(a). In the prototype design, four μCVD units have been constructed on a chip of 6×5 mm^2 in size as shown in the optical image in Figure 2.17(b). When the electrical power was applied to the second μCVD unit from the left, the micro-heater was observed to glow visibly at high temperature. The corresponding infrared image in Figure 2.17(c) (FLIR® A320 Camera, the emissivity of the μCVD chip surface is calibrated to be 0.75 as explained in Figure 2.16) validates that the high temperature region was localized at the micro-heater. Materials that cannot sustain high temperature can therefore be placed close to the micro-heater unit without thermal damages or degradations during the synthesis process. For example, a 50-μm-thick sticky tape (Kapton®, 2 mil) as seen at the bottom of Figure 2.17(b) has been used as the spacer to adjust the height of the gas flow channel between the top cap and the μCVD unit and no damages have been identified after the growth process.

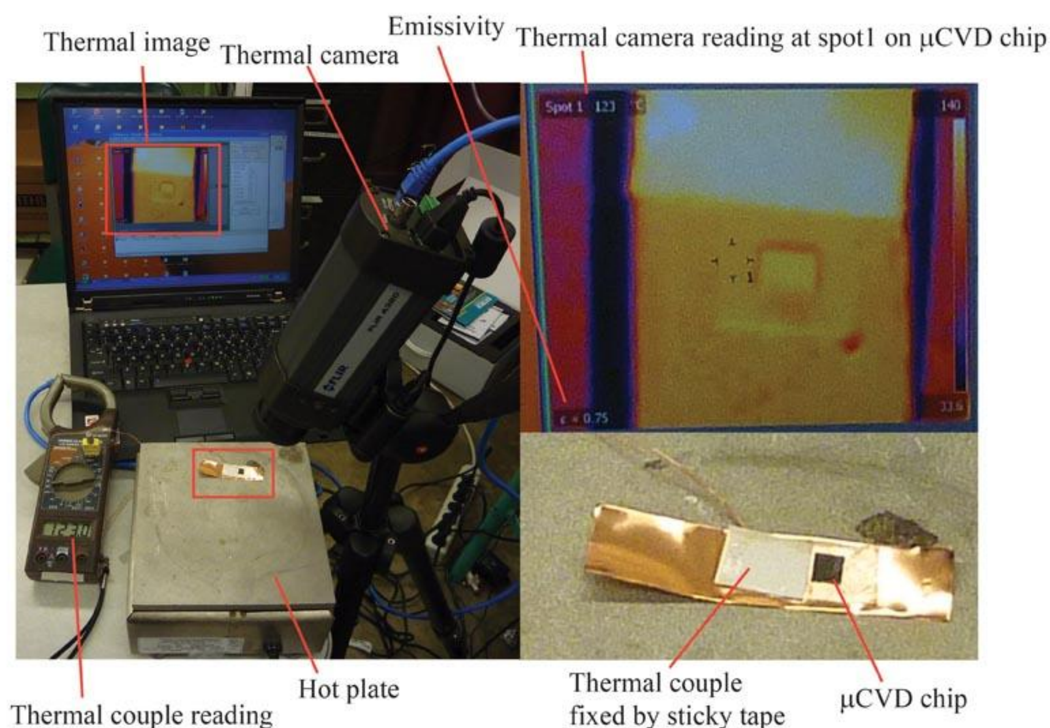

Figure 2.16: Calibration of the emissivity of the µCVD chip surface. The emissivity of the µCVD chip surface is calibrated by a thermal couple. The thermal couple and the µCVD chip are fixed closely to each other on a copper sheet so that the readings from the thermal couple represent the actual temperature of the µCVD chip. A hot plate is used as a heat source to control the temperature. The emissivity value is adjusted in the process until the temperature readings are the same from the IR camera (FLIR® A320) and the thermal couple. The top surface of the µCVD chip is silicon and our calibration process covers a temperature range from 50 to 130˚C. Within this range, the difference of the temperature readings from the thermal couple and the IR camera are within 3˚C. This implies that our IR camera is calibrated for the low temperature operations. The IR camera is working on the wavelength of 7.5-13 µm. The emissivity of µCVD chip surface is found to be 0.75, which is consistent with previous findings on heavily doped silicon [88].

The cantilever design causes non-uniform temperature distribution along its length which could potentially affect the quality of the nanotubes [72]. To overcome this potential problem, microchannels of 5 µm in diameter have been constructed vertically throughout the suspended 50-µm-thick cantilever platform. When the reactive gases are forced to flow through these microchannels from bottom to top as illustrated in Figure 2.17(d), they can be modeled as miniaturized CVD furnaces.

The following conditions are the basic assumptions used to estimate the gas temperature inside the µCVD microchannels.

1. Laminar flow in the microchannels. Reynolds number is calculated to be about 0.01 (See Section 2.1.3 [89]), which is much smaller than the upper limit for laminar flow (~2000) [81].

2. Negligible heat radiation: The reactive gases are transparent to most part of the spectrum of thermal radiation except for several absorption peaks in the infrared region.

The energy conservation model at steady state calls for:

$$k\nabla^2 T - c_p\, \rho\, \boldsymbol{v} \cdot \nabla T = 0 \tag{2.10}$$

where T is the gas temperature, k is the thermal conductivity of the gas, ρ is the mass density of the gas, c_p is the specific thermal capacity (constant pressure) of the gas per unit mass, and $\boldsymbol{v}$ is the gas velocity. The first term at the left-hand side describes the heat transfer into a volume by conduction. The second term describes the energy transfer by the mass flow. The sum of the two terms therefore describes the total energy flow into the volume and should be proportional to the temperature change rate. Under steady state, the two terms should cancel out each other.

The equation is solved in a cylindrical coordinate system numerically by assuming the parabolic flow velocity profile since the microchannels are long enough (aspect ratio 10:1) to have a fully developed flow pattern. This is also verified in the flow simulation described in the next section. The boundary conditions are:

$$T/_{r=R} = T_w, \text{ and } T/_{z=0} = T_0 \tag{2.11}$$

where R is the radius of the microchannel, T_w is the temperature of the wall of the microchannel, and T_0 is the room temperature. The two boundary conditions represent the fact that: 1) The gas temperature at the wall of the microchannel is T_w; 2) The gas at the inlet of microchannel is at room temperature. The calculated gas temperature results are illustrated in Figure 2.17(e). It is noted that the cold gas is quickly warmed up and its temperature becomes stable within approximately the first 5 μm into the microchannel, much shorter than the total length of the microchannel of 50 μm. Therefore, a uniform temperature profile is expected in the latter part of the microchannel which emulates that of a large scale CVD system to provide well-controlled growth environment for SWNTs. The gas parameters used in the calculation is for ethylene. The addition of hydrogen gas in the ethylene gas will have similar results except with even shorter warm-up distance due to higher thermal conductivity of hydrogen.

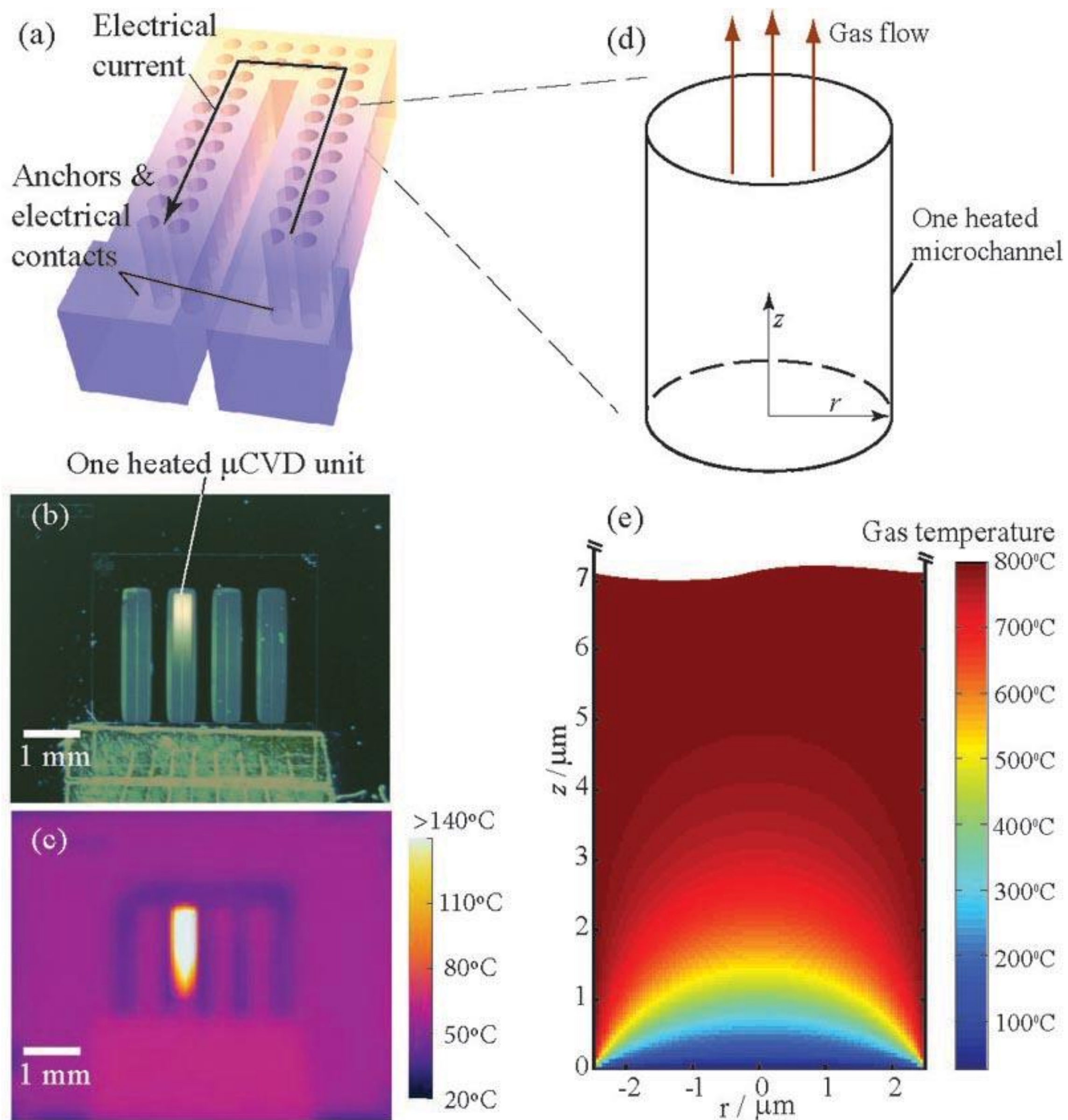

Figure 2.17: Temperature analysis of the μCVD system. (a) A μCVD unit is heated by joule heating when electrical current is applied. (b) An optical photo showing a μCVD unit is selectively heated with glowing color indicating high temperature areas. (c) Infrared image of the same structure in (b) indicating all regions but that of the heated μCVD unit are at low temperature. (d) The gas flow through one microchannel in a μCVD unit. The temperature distribution of the gas is illustrated in (e). It is observed that the temperature profile becomes uniform after approximately 5 μm into the microchannel.

Because of the enlarged backside openings, there will be gas leakage from the sideways of the cantilever as illustrated in Figure 2.18(a) (See Figure 2.6, the dark rectangular region next to the microchannels) compared to the previous design. Severe leakage can change the pressure difference across the microchannels significantly. Fortunately, the width of the possible gas leakage path is approximately 10 micrometers, which is much smaller than the gas feeding lines whose diameters are at least several millimeters. As a result, the flow resistance (connected in parallel with the

microchannels) is large and will not affect the previous approximation that the measured pressure difference is the pressure drop between the two sides of a microchannel. A detailed simulation is also conducted in ANSYS® Fluent®. Figure 2.18(b) is the pressure plot of the system and it can be observed that the gas pressure drop occurs across the microchannels (major resistance). Figure 2.18(c) illustrates the stream lines with velocity profile in colors. High velocity profile is noted at the gas leakage path as well as the downstream gas flows which can be observed in Figure 2.18(c).

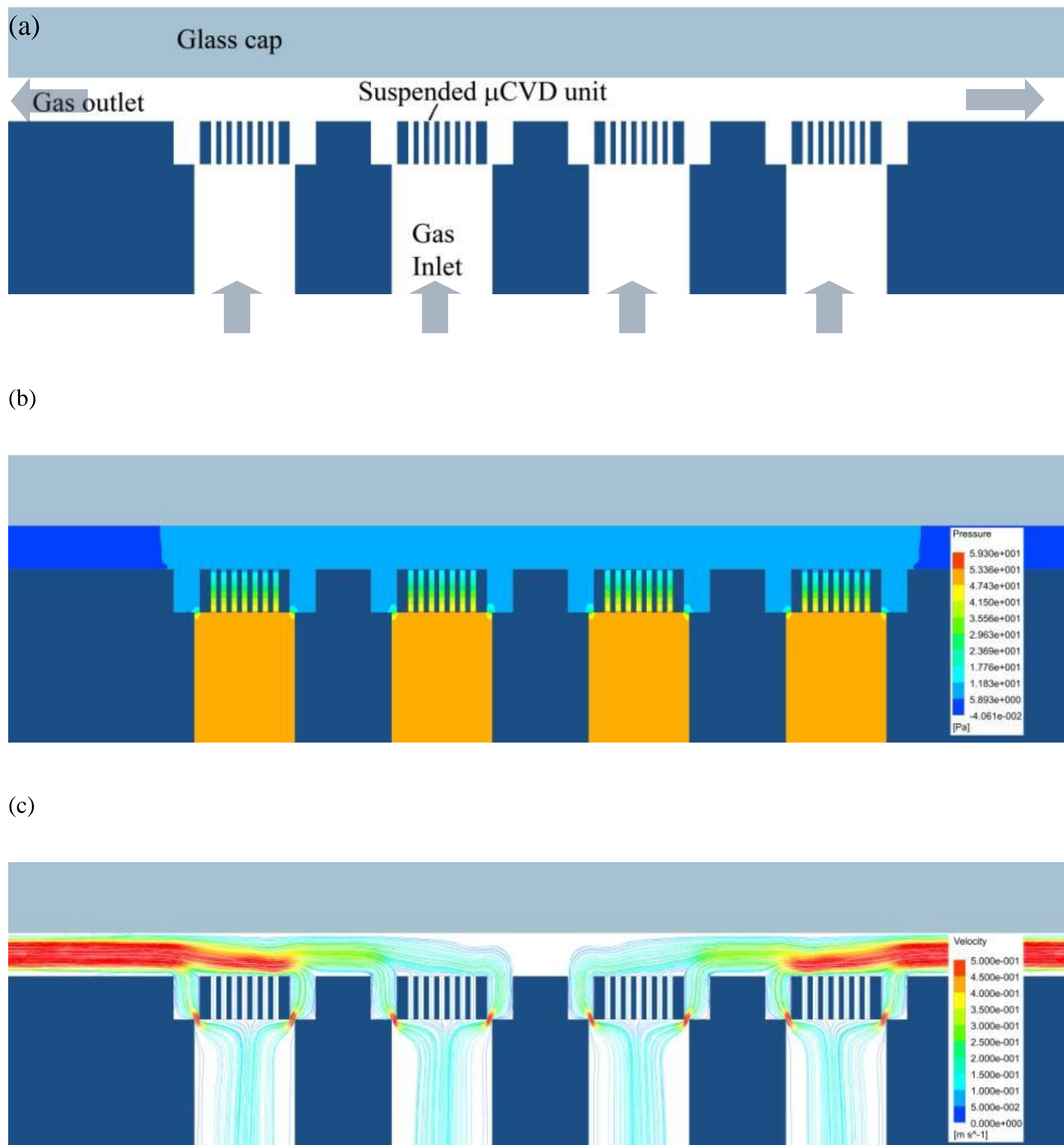

Figure 2.18: Gas flow simulations by ANSYS® Fluent®. (a) Cross sectional view of the structure being computed. (b) Pressure distribution. (c) Stream lines with velocity distribution.

2.2.3 Microheater with square-shape platform (Type II)

Uniform temperature distribution is essential for high quality material synthesis that requires uniformity such as film thickness over a large area. Therefore, in contrast to the aforementioned U-shaped cantilever design, a second microheater design with a square-shape platform is also designed and fabricated for the synthesis of large area nanostructures. For example, graphene is a two-dimensional nanostructure and in the synthesis process of graphene, highly efficient mass transport is not required. As a result, a central heating platform with uniform temperature distribution is the key architecture for the second type microheater. Figure 2.19 illustrates a fabricated μCVD unit built from a silicon-on-insulator (SOI) wafer specifically for the synthesis of graphene. The system is composed of a 300 μm × 300 μm suspended heating stage in the center, supported by 6 folded beams which are designed to absorb possible thermal stress during the synthesis process.

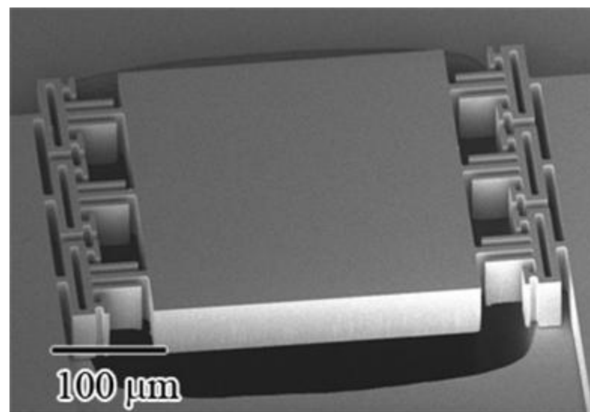

Figure 2.19: A scanning electron microscopic picture showing the fabricated μCVD chip for graphene synthesis.

As discussed previously, the conductive heat flow to the substrate and convective heat flow to the environment dominates the heat loss of the heating stage. As a result, the length and width of the supporting beams are important parameters in the process of heat generations and heat losses. By carefully choosing these parameters, a heating platform for an operation temperature at 1000 ℃ with temperature variations within 5 ℃ could be realized. Figure 2.1 illustrates the temperature distribution simulated by ANSYS® with good uniformity over the heating platform. Specifically, a uniform temperature field is especially critical for the synthesis of graphene by using nickel layer to absorb equal amount of carbon during the heating process to construct a consistent number of graphene layers.

2.3 Fabrication Process of μCVD growth chips

One key consideration on the design of the μCVD chip is the compatibility to available micro-machining processes. For instance, the microchannels are placed vertically because they can be patterned by photolithography and fabricated by deep reactive-ion etching (DRIE). The main steps of the μCVD chip fabrication process are described in Figure 2.20. The process begins with a standard silicon-on-insulator (SOI) wafer. The wafer has a device layer of 50 μm in thickness, a buried oxide (BOX) layer of

1 μm in thickness, and a handling substrate of 525 μm in thickness. The device layer is heavily boron doped with a resistivity of 0.001 Ω·cm. A wet thermal oxide layer with a thickness of 2 μm is first grown to cover the whole wafer at the temperature of 1000 ℃ as illustrated in Figure 2.20(a). This oxide layer serves both as an etching mask for later processes and as a protective layer for the device layer during wafer handling. The backside of the wafer is then going through the lithography and etching process first. MEGAPOSITTM SPRTM-220 thick photoresist from ROHM and HAAS® is spin-coated onto the handling layer with a thickness of 10 μm. The soft-bake temperature used here is 95 ℃ instead of the standard soft-bake temperature of 115 ℃, because the photoresist would be subject to serious cracking issues during the DRIE step if the standard soft-bake temperature was used. Using the lower soft-bake temperature will sacrifice some resolution in photolithography which is negligible since the backside openings are all relatively large in size (minimum width of 200 μm). The bake time is slightly elongated from the standard 5 minutes to 7.5 minutes. The photoresist is then exposed following standard photolithography process using Karl Suss® MA6 Mask Aligner with the soft contact program. After the exposure, the post-exposure-bake temperature is the standard temperature of 115 ℃ but the baking time is shortened to 3 minutes instead of the standard 6.5 minutes to avoid cracking of photoresist. The photoresist is developed, rinsed, dried, and ready to serve as an etching mask. The wafer is first dry etched in a plasma etcher (Lam Research) to remove the exposed oxide layer with RF power of 400 W, processing gas CHF_3 at 30 sccm and CF_4 at 90 sccm, and chamber pressure of 2.8 Torr. It is noted that a reduced power (the standard etching power is 850 W) is used to reduce the possible high temperature damages to the photoresist during the etching process. The wafer is then processed in Surface Technology Systems (STS) Advanced Silicon Etch (ASE) system for DRIE (Deep Reactive Ion Etching). The process is highly anisotropic and stops at the BOX layer. The etch rate is roughly 2~3 μm/min for a standard recipe HEX100A. The etch selectivity is roughly 1:100 between silicon dioxide and silicon, and 1:70 between photoresist and silicon. All the photoresist is consumed during the etching, so that no photoresist stripping is needed. After these steps, Figure 2.20(b) applies.

Afterwards, OCG 825 g-line photoresist from Fujifilm is spin-coated onto the device layer with a thickness of 2 μm. It is exposed using Karl Suss® MA6 Mask Aligner with the hard contact program. Backside alignment is necessary for this step to make sure that the backside openings are aligned with the heating platforms at the front side. With microchannels of 5 μm diameter, the feature size is much smaller than the backside openings, so the hard contact program is used for better resolution. After development, the photoresist is treated with ultraviolet light at 240 ℃ for 2 minutes in Fusion M150PC Photostabilizer System. The ultraviolet light treatment can cross-link and harden the patterned photoresist, making it more resistant to plasma etching. The wafer is again processed in the Lam plasma etcher to remove the patterned thermal oxide layer. The etching power is the standard 850W because the thinner photoresist can dissipate heat more easily and is already treated with ultraviolet light at relatively high temperature for stronger etching resistance. Higher etching power is also preferred for uniform and anisotropic etching. The 2-μm-thick oxide layer serves as the etching mask for the next DRIE step. The DRIE plasma is coupled by 380 kHz RF generator with 15 ms on time and 5 ms off time. This configuration is used to cope with the inherent variability in etch

uniformity across the wafer (bull's-eye effect), the micro loading effect (RIE-lag), and the aspect ratio dependent etching effect (ARDE) [90]. The etch rate for this recipe is much lower at roughly 1.2 μm/min with selectivity approximately 1:20 for photoresist and 1:70 for oxide. After the etch, the wafer is put into piranha solution (3:1 concentrated sulfuric acid to 30% hydrogen peroxide solution) at 120 ℃ to remove the etch residues, such as photoresist and carbon-based residues from the DRIE passivation cycle. The wafer is then gone through a time-etching process in a 5:1 buffered oxide etch solution to release the structure. Figure 2.20(c) applies after these steps.

Metallic catalyst is typically required for the synthesis of nanostructures. In the synthesis process, silicon could form silicide with various metals at high temperature which inactivates the functionality of the catalyst. Therefore, a barrier layer is necessary to prevent the direct contact of metal and silicon. This is accomplished by a thermal oxidation at 1000 ℃ for a 200 nm-thick oxide layer as shown in (Figure 2.20(d)).

This newly grown thermal oxide layer prevents electric contacts to the buried silicon device layer and has to be selectively removed to allow for electric contacts. Photolithography at this stage is tricky because the device layer has many high-aspect ratio structures. After many trials, dry-film photoresist FX940 from DuPont® is used. This 40-μm-thick negative photoresist film is applied by hand to cover the wafer. The alignment error is about 30 μm which is good enough to define the electric contact pads with a minimum feature size of 200 μm. After development, the wafer is put into a plasma etcher (Plasma-Therm PK-12) for oxide removal with gas flow rate of 4 sccm oxygen and 80 sccm CHF_3, RF power at 100 W and the pressure at 1 Torr. The etch rate is approximately 30 nm/min. It is noted that the power used here is much lower than the previous oxide etch, because the dry-film photoresist is very thick and temperature sensitive. The photoresist is then stripped off, and the wafer is cleaned in piranha solution. Figure 2.20(e) applies after these process steps.

Finally, the wafer is spin-coated with another layer of protective photoresist and diced into chips. After stripping off the photoresist, the chips can be deposit with the right catalyst without using any mask as illustrated in Figure 2.20(f). In this case, the process for a droplet-based catalyst deposition is assumed such that the deposition is limited to the heating platform area as shown. Electrical connections are made to the μCVD chip by wire-bonding and the chip is ready for the synthesis process of specific nanomaterial.

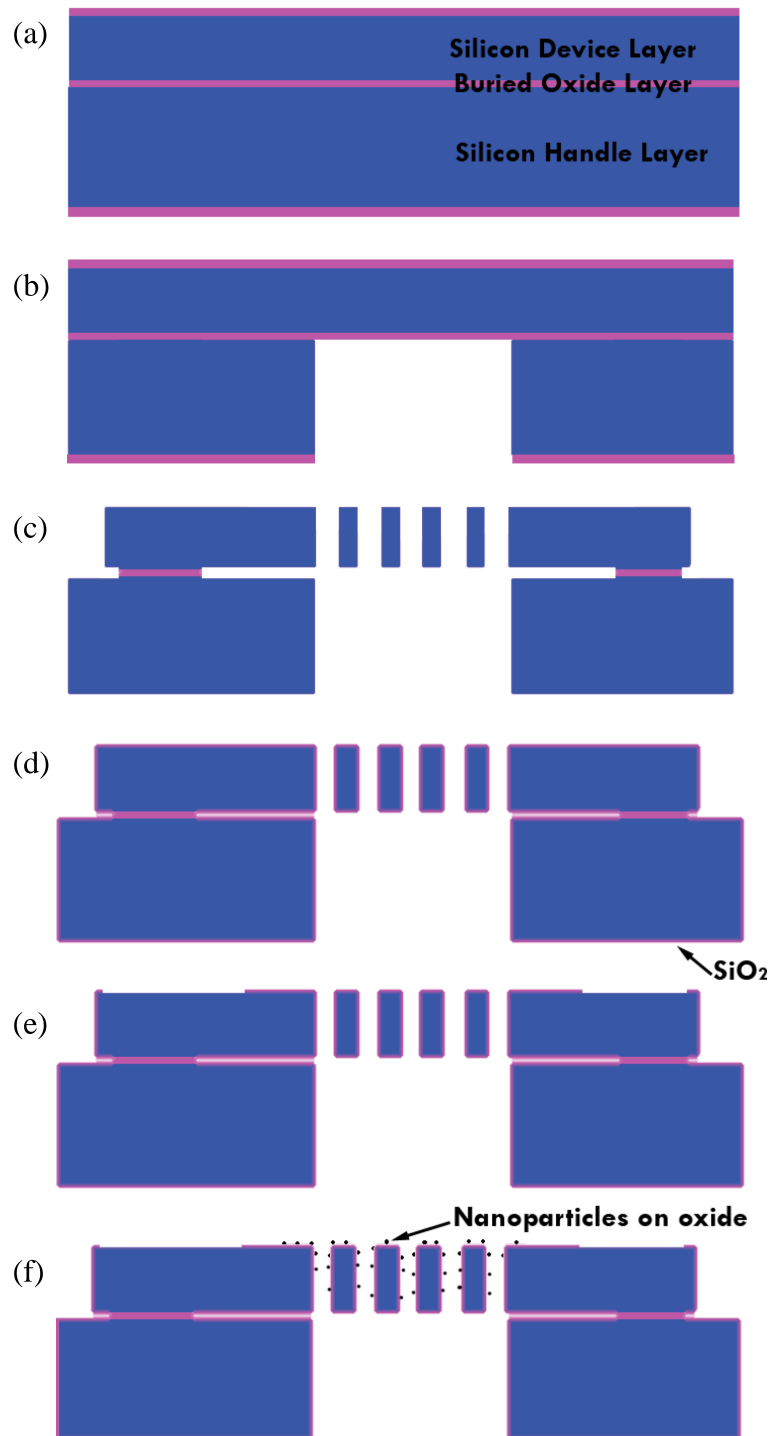

Figure 2.20: Typical fabrication process of a μCVD chip. (a) Start with a SOI wafer; (b) Backside patterning and etching; (c) Front side patterning and etching; (d) Growth of thermal oxide layer; (e) Patterning the thermal oxide layer to open electrical contacts; (f) Catalyst nanoparticle deposition for nanomaterial synthesis.

The SEM picture of a fabricated μCVD chip is shown in Figure 2.21. Four units are shown and the false-colored region indicates one of them. The U-shaped cantilever structure is clearly visible in green color. The backside openings are also visible as black slits.

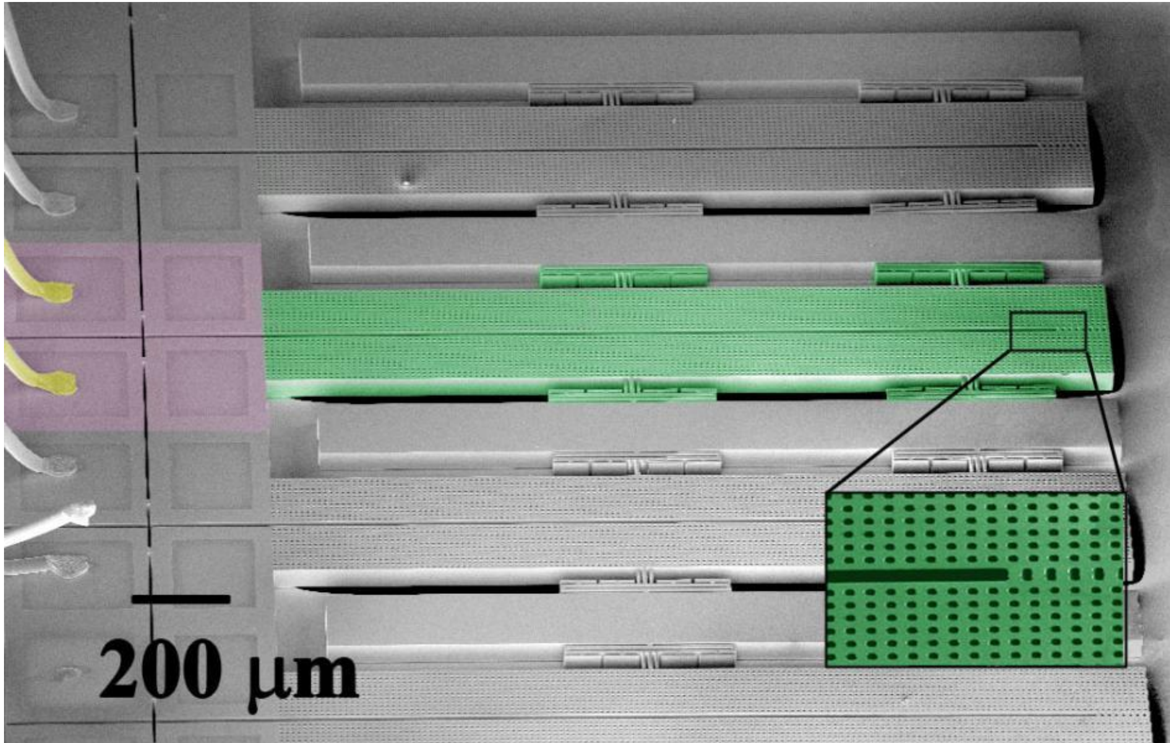

Figure 2.21: The scanning electron microscope (SEM) image of a fabricated μCVD array with several μCVD units. The false-color region indicates one of the units with the electrical wires in yellow color, the bonding pads in purple color, and the U-shaped cantilever in green color where many vertical microchannels are built in (inset).

2.4 System Architecture and Assembly

2.4.1 System Architecture

The μCVD system requires monitoring and control of temperature, gas flow and heating power concurrently for reliable nanostructure synthesis. The architecture for the peripheral components is illustrated in Figure 2.22.

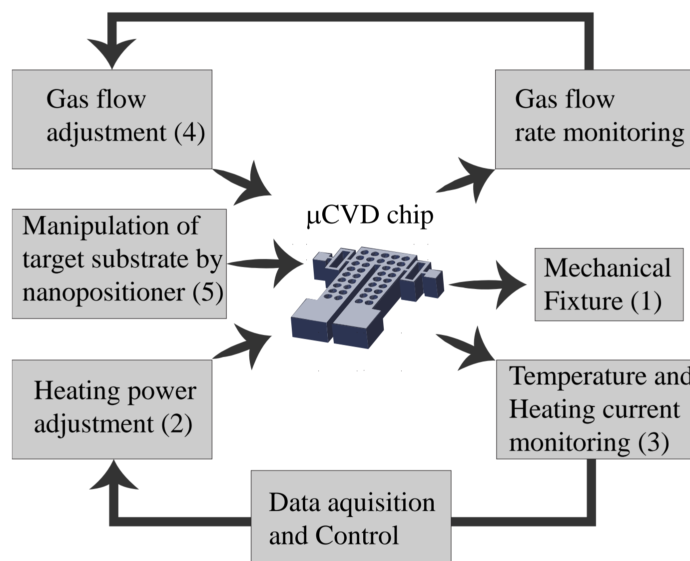

Figure 2.22: The system architecture including components and their relationship to the μCVD chip.

Mechanical assembly of the μCVD system is required in order to (1) hold the μCVD chip; (2) achieve electrical contacts during the experiments; (3) allow optical temperature monitoring; (4) allow controlling the flow rate of the processing gases; and (5) allow possible extension of the experiments such as interface to a nanopositioner to actively control the locations of the nanomaterial deposition process. The detail of the constructions of each component can be found in Appendix A.

2.4.2 Temperature Monitoring System

Temperature control plays an important role in the synthesis process to produce high quality materials by the μCVD system. For example, the synthesis of graphene on top of a nickel film (to be described in details in Chapter 3) should occur at an optimum temperature of 1000 ℃ using a traditional furnace. At 950 ℃, the synthesized graphene layer won't be continuous with lots of defects. At 1050°C, the nickel film (only 300 nm in thickness) starts to melt and its surface becomes rough and bumpy resulting in discontinuous and defective graphene. Therefore, it is vital to control and monitor the temperature in a conventional CVD system and it would be even more important for

μCVD system as temperature in a microsystem could change drastically without a good temperature control scheme.

A rough estimation of the temperature for the μCVD system can be obtained by monitoring the I-V (electrical current-voltage) curve of the micro heater during the synthesis process. Figure 2.23 illustrates a typical I-V curve of a fabricated micro heater. In region I, the silicon resistor is at low temperature, and the I-V curve follows Ohm's law. In region II, the micro heater starts to warm up. Electron transport becomes scattered by the increasing number of phonons such that the curve bends downward (Matthiessen's rule) [91]. In region III, the temperature gets even hotter and thermally exited charge carriers start to appear in large numbers and to contribute to the electrical current. As a result, the I-V curve starts to curl upward. The temperature is estimated from the emitting light color and intensity of heater to be around 600 ℃ between region I and II, and 800 ℃ between region II and III. This I-V curve method provides a rough estimation about the reaction temperature and it could also quickly validate the temperature measurement results from other more precise methods.

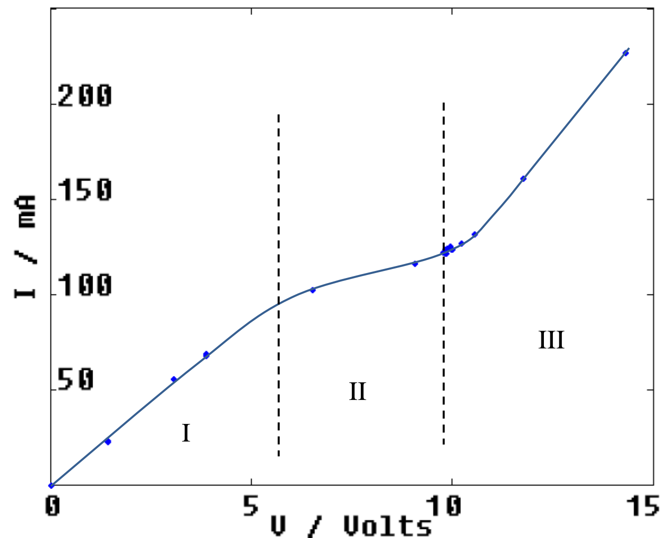

Figure 2.23: A typical I-V curve from a silicon heater.

In the reaction chamber of a conventional furnace, the temperature can be measured by thermal couples via direct contacts with good precision. However, commercially available thermal couples are too bulky to be used for the μCVD system. Alternatively, with an addition layer of material such as platinum, thermal couples can be built together with the micro heater. This approach, however, significantly increases complicity of the micro fabrication process. Therefore, a non-contact temperature measurement solution is developed here. Specifically, the light radiated from a black body at a given temperature *T* can be described by Plank's law [91, 92], which states:

$$J(\upsilon,T) = \frac{2h\upsilon^3}{c^2}\frac{1}{e^{\frac{h\upsilon}{kT}}-1} \tag{2.12}$$

where *J* is spectral radiance, or energy per unit time per unit surface area of the emitting

surface per unit solid angle per unit frequency, h is Plank's constant, c is the light velocity in vacuum, k is Boltzmann's constant, and υ is the frequency. Integrating J over frequency and solid angle gives the Stefan-Boltzmann law [92]:

$$I = \frac{2\pi^5 k^4}{15c^2 h^3} T^4 = \sigma T^4 \tag{2.13}$$

, here I is the radiated power per unit area, and σ is Stefan's constant, $\sigma = 5.7 \times 10^{-8}$ J $s^{-1}m^{-2}K^{-4}$.

There are two possible approaches for the optical temperature measurement. The first approach is based on the Stefan-Boltzmann law, which measures the absolute total light intensity since it scales with temperature to the fourth power. The second approach is based on Plank's law, which measures the spectrum, the relative intensity at different frequency of the emitted light. Both methods require calibration since the target is usually not a completely black body, and the optical imaging system also affects the radiated light spectrum.

The first approach seems to be easy at the first glance since it only requires a photodetector. However, temperature, size, orientation and distance of the object all affect the readings from the radiation intensity such that a complicated optical imaging system with a photodetector array is required to provide good spatial resolution. A complete imaging system, or a camera, is usually utilized to provide such information such as those commercially available thermal cameras (for example, FLIR® systems). However, the cost for such a system is high and the spatial resolution is low. Therefore, the second approach based on spectrum shifts with respect to temperature changes is implemented in this work. The relative intensity ratios of radiated light from a black body at two different wavelengths of 2.0 μm and 1.0 μm are listed in Table 2.1 and it is observed that the intensity ratios change drastically with temperature and could be used for temperature measurements. Furthermore, the method is also relatively robust because it measures the relative intensity ratios and does not depend on the sample size, orientation or distance to the detector.

Table 2.1: Radiation intensity at different wavelength λ according to Plank's law.

Temperature (℃)	Intensity at λ=2.0 μm (pW m^{-2} sr^{-1} Hz^{-1})	Intensity at λ=1.0 μm (pW m^{-2} sr^{-1} Hz^{-1})	Ratio ($I_{\lambda=2.0\ \mu m} / I_{\lambda=1.0\ \mu m}$)
700	30.3	0.147	206
750	43.5	0.303	143
800	60.4	0.585	103
850	81.4	1.063	77
900	107.1	1.837	58
950	137.7	3.035	45
1000	173.7	4.821	36

Usually, a spectrometer is required to resolve light intensities at different wavelengths. However, for the purpose of temperature measurement, measuring intensities centered at

two different wavelengths are sufficient. A two-color detector is utilized which eliminates the requirement for a spectrometer and significantly reduces the cost and complicity of the measurement system. The details of the temperature monitoring system can be found in Appendix B. Different optical designs as well as an amplifier circuit are analyzed and compared and the system is built. Figure 2.24 shows the calibration results and theoretical results following Plank's Law using intensity ratio of two wavelengths at 1.03 μm and 2.0 μm, respectively. It is noted that the experimental numbers here are not from absolute intensity ratios but relative intensity ratios. The results are in good agreement with theoretical predictions by Plank's law, implying a good temperature measurement system.

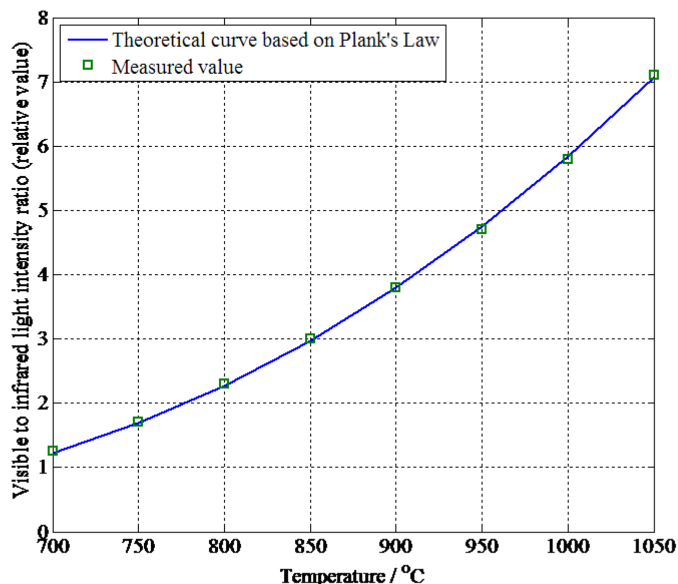

Figure 2.24: Measured signal strength ratio of Si to PbS detector. The fitted curve is based on Plank's law.

2.4.3 Flow Rate Control

The mean gas flow velocity v_m inside the microchannels can be calculated by the pressure drop Δp across the microchannels based on a fluid mechanics derivation [81]:

$$v_m = \frac{r_0^2}{8\mu} \frac{\Delta p}{L_{mc}} \tag{2.14}$$

where L_{mc} is the length of the microchannels, r_0 is the radius of the microchannels, and μ is the viscosity of the gas. It is noted that the flow velocity can be controlled by varying the pressure drop since they are in linear proportion. The details of the experimental setup can be found in Appendix A.2.

2.4.4 Electrical Interface and Computer Control

Figure 2.25 illustrate the architecture of the electrical interface and computer control for the μCVD system. Temperature measurement results are used as the feedback to

adjust the applied electrical current of the microheater with an appropriate control strategy. In the case of extending experiments with an active nanopositioner, the movement of the nanopositioner has to be controlled via the computer. The details of the construction are presented in Appendix C.

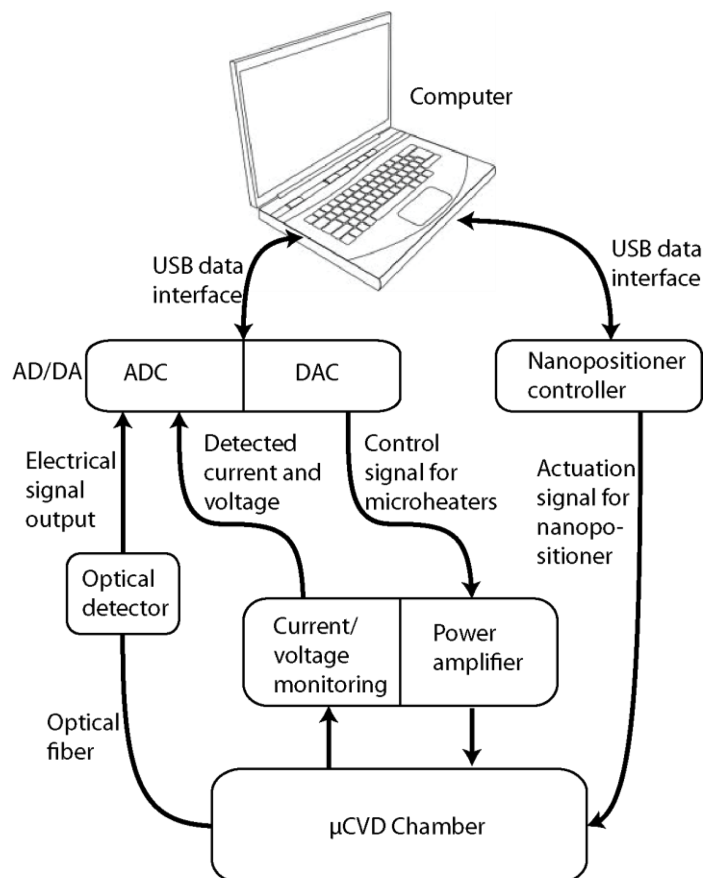

Figure 2.25: The electrical interface for µCVD system.

Chapter 3

Application Demonstrations of μCVD

3.1 Carbon Nanotube Synthesis with Enhanced Mass Transport

3.1.1 Introduction

Chemical vapor deposition (CVD) has been broadly adopted to grow single-walled carbon nanotubes (SWNTs) [56, 93]. However, it has been well documented that this growth process will terminate after a short period of time (usually several minutes) [93, 94]. The reason, as suspected by many groups, is the formation of amorphous carbon [80, 95-97] that poisons the catalyst nanoparticles. The generally established growth mechanism for SWNTs is the vapor-liquid-solid (VLS) process [64, 97-99], in which carbon from the decomposed hydrocarbon gas is absorbed by nanoparticle catalysts at high temperature, and SWNTs are grown as a result of carbon super-saturation. The formation of amorphous carbon, on the other hand, does not require catalysts and is therefore a direct vapor-solid (VS) process. Various methods and carefully chosen experimental parameters have been implemented [100, 101] to inhibit this process, resulting in nanotubes of millimeter length and free of amorphous carbon. Most of these methods are based on chemistry, using different gas source or catalyst. One example is to introduce hydrogen gas into the system, thereby impeding the forward progress of the decomposition reaction of hydrocarbon gas, as suggested by Le Chatelier's principle [95]. However, this method would also suppress carbon super-saturation and therefore the growth of SWNTs.

The different growth mechanisms between SWNTs (VLS process) and amorphous carbon (VS process) provide the possibility of promoting one process and suppressing the other. This could be accomplished via "enhanced mass transport" by increasing the rate of gas molecules entering and leaving reaction sites during the growth process. Slower mass transport allows the gas to remain in the immediate vicinity of the reaction site at high temperature for a longer period of time, increasing the likelihood of decomposition [57]. As a result, promoting mass transport could suppress the formation of amorphous carbon while having no effect on SWNT growth since the process is usually limited by reaction rate rather than mass transport [97].

The mass transport process can be enhanced by increasing the gas flow rate. In most atmospheric pressure synthesis processes, the gas velocity near the reaction surface is close to zero. As a result, reactant gas does not directly impinge on the substrate but diffuses through a distance δ to the reaction surface. The diffusion length, δ, is the distance from the reaction surface to the convective gas stock, where gas can freely flow in and out. A small δ corresponds to a short distance that gas has to diffuse through to reach the reaction surface, yielding fast mass transport. One way to reduce δ is to increase the velocity gradient (calculated in the direction perpendicular to the reaction surface) near the reaction surface, in which case flow streams with higher velocity are drawn closer to the reaction surface. A simple way to increase the velocity gradient is to

increase the gas flow rate. However, it has been discovered that in conventional CVD systems this could result in turbulent flow and affect the quality of SWNTs [79, 97].

3.1.2 Experiments

Experimentally, iron nanoparticles are first deposited by a solution-based method [65, 102] following the μCVD fabrication process as detailed in chapter 3 as the catalyst for SWNT synthesis. Ethylene and hydrogen (volume ratio 3:20) were then used as the source gases during the growth process. The measured pressure drop from the backside opening underneath the testing chip to the testing chamber is 250 Pa. The pressure drop of an individual microchannel should be close to 250 Pa since the microchannels experience much larger flow resistance than macro-sized gas lines. The mean flow velocity v_m can therefore be estimated as [81]:

$$v_m = \frac{r_0^2}{8\mu}\frac{\Delta p}{L_{mc}} \approx \frac{(2.5\mu\text{m})^2 \times 250\text{Pa}}{8\times 8.4\times 10^{-6}\text{Pa}\cdot\text{s}\times 50\mu\text{m}} \approx 40\text{cm/s} \tag{3.1}$$

where p is the gas pressure, and L_{mc} is the length of the microchannels. Viscosity of hydrogen is used in this calculation. It is noted that the applied pressure is much larger than in a conventional setup (on the order of 10^{-3} Pa for 3000 sccm flow in a 50 mm inner diameter tube with 1 m length) to achieve comparable flow velocity.

In the experiments on a prototype μCVD system, an electrical current of 180mA was used and the temperature of the tip region (center of the U-shaped heater) reached about 900 ℃ based on a simplified electrothermal model and experimental verification [72, 103, 104]. It was observed under SEM analyses that dense and long SWNT growth occurred in the regions with a temperature of approximately 800°C. The temperature of the whole U-shaped cantilever was not uniform, but the temperature of a particular microchannel was locally uniform and stable to grow SWNTs (See Chapter 2.2.2 for detailed temperature analysis).

3.1.3 Results and discussion

Figure 3.1(a) shows the synthesis results of SWNTs by the μCVD system. In this experiment, in addition to the vertical gas supply through the microchannels, gas was additionally flowed horizontally on the top surface of the μCVD system from left to right. This flow can force SWNTs to fall rightwards onto nearby micro structures after the growth process. As a result, structures seen in the SEM photo from left to right are: a region of the μCVD heater with built-in microchannels, a dark through-hole region, a folded beam structure, an anchor for a folded beam, an isolation area (without the top silicon device layer to isolate the individual μCVD systems), and a chip edge shoulder. Some gas will leak from the dark through-hole region during growth. Severe leakage can change the pressure difference across the microchannels significantly and therefore invalidate the previous analysis on gas flow. Fortunately, the width of the slit is only approximately 20 microns, which is much smaller than gas feeding lines whose diameters are at least several millimeters. As a result, its flow resistance (connected in parallel with the microchannels) is large and will not affect the previous approximation that the measured pressure difference equals the pressure drop between the two sides of a microchannel. The synthesized SWNTs grew up to 0.7 mm in length in a 30 min growth

process. In the microchannel area as shown in Figure 3.1(b), SWNTs were distributed randomly as they grew and fell onto the substrate. Over the through-hole region, SWNTs were suspended and difficult to distinguish, so a high-contrast SEM photo was taken to reveal them in Figure 3.1(c). Some of the longer SWNTs can be observed in Figure 3.1(d) in the anchor region. It is believed that the growth mechanism of these long SWNTs was base growth – otherwise catalyst particles would be far away from the heat source and no growth could occur.

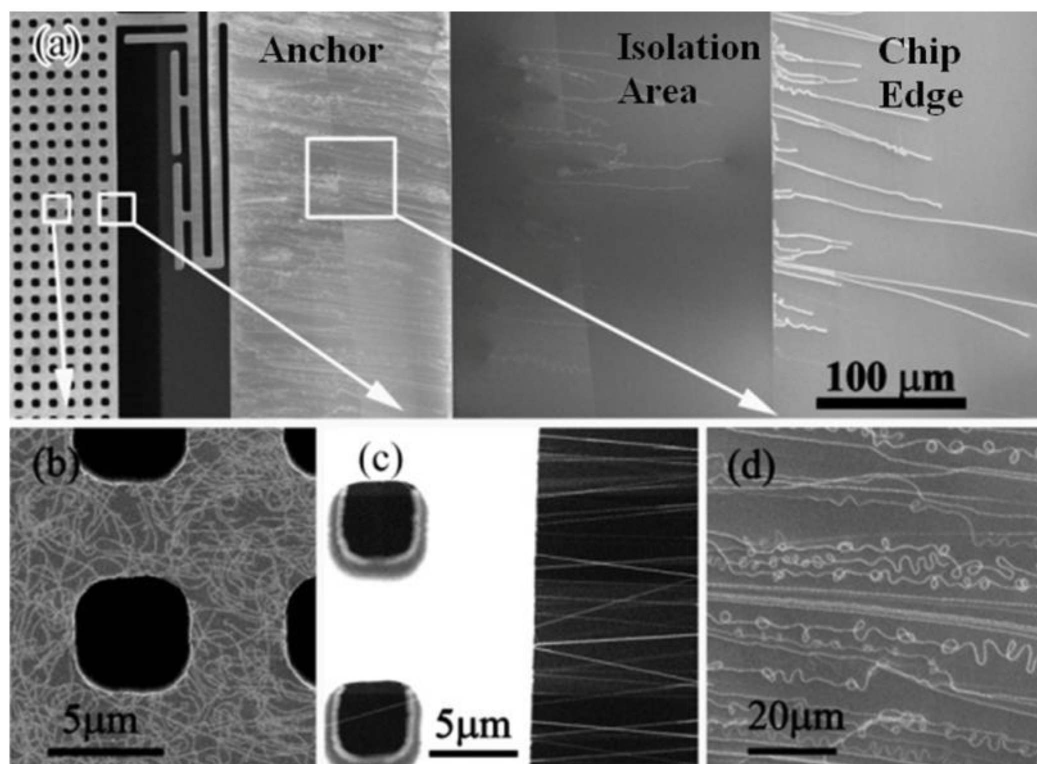

Figure 3.1: SEM images showing growth results. (a) Overview. The left side is the growth side and a portion of the U-shaped micro heater is shown. SWNTs fell to the right due to the external horizontal gas flow. (b) A close view near the microchannel region showing randomly distributed SWNTs. (c) A high-contrast SEM image close to the edge of the micro heater revealing many suspended SWNTs over the through-hole regions. (d) A close view showing longer and aligned SWNTs that lying on near-by structures.

The nanotubes synthesized by μCVD were free of amorphous carbon as seen in the close view SEM photo in Figure 3.2(a). Atomic force microscopy (AFM) was used to verify the results in Figure 3.2(b). It is found that most synthesized nanotubes were single-walled and had diameters in the range of 1~2nm. They appeared to have larger diameters under SEM due to charge effects [105]. This is the first successful attempt to grow clean and small-diameter SWNTs using the μCVD system with solution-based iron nanoparticles as catalysts, and hydrogen and ethylene as gas sources. Methane [93], ethanol [101], or carbon monoxide [106] is usually reported as the carbon source in the growth of SWNTs. Ethylene is sometimes added in very small amounts to increase gas activity [107] but has never been used successfully as the main carbon source, except for

the "super-growth" mechanism [94] where water is added to keep the catalyst active. The difficulty of using ethylene as the main carbon source is that ethylene decomposition starts at relatively low temperature (~750 ℃) while small-diameter SWNT growth usually happens at higher temperature (>800 ℃) [97]. As a result, amorphous carbon from the pyrolysis of ethylene can easily deposit in large amounts to block the growth of SWNTs.

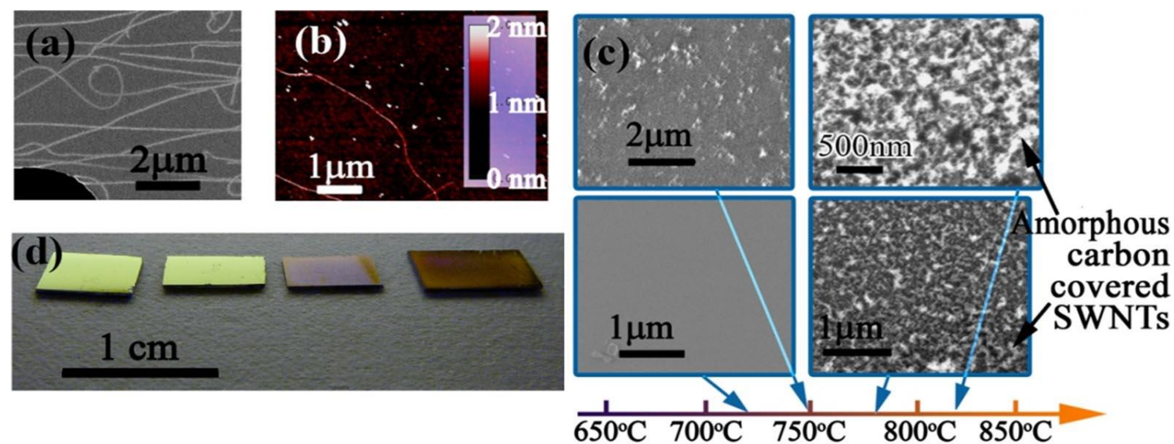

Figure 3.2: SWNTs synthesized from μCVD and conventional CVD. (a) A SEM image showing clean SWNTs from μCVD. (b) An AFM image is used to characterize the diameter of SWNTs from μCVD. (c) SEM photos showing results from control experiments to synthesize SWNTs from conventional furnace, with the same source gas under different growth temperatures from 720–820 ℃. (d) Optical images of the chips in (c), showing amorphous carbon formation at high temperatures.

Control experiments have been conducted using a conventional CVD setup with the same catalyst and gas inputs under various temperatures between 600-850 ℃. It was observed that no growth occurred at low temperature, and as the growth temperature increased, short and curly nanotubes were grown, but they were covered by a significant amount of amorphous carbon. SEM photos of samples grown in 5 minutes at 720 ℃, 750 ℃, 780 ℃, and 820 ℃ are shown respectively in Figure 3.2(c). Optical observation of the 820 ℃ growth showed a black substance covering all the chips (Figure 3.2(d)) as well as the walls of the growth furnace. The widely-spread black substance was considered to be amorphous carbon as its formation does not require catalysts. It is concluded that μCVD significantly enhances mass transport without causing turbulence, and thus may allow the use of a wider variety of gas sources for potentially new synthesis results.

3.2 Direct Growth of Aligned SWNTs on Temperature Sensitive Substrates

3.2.1 Introduction

The integration of nanomaterials with flexible substrates has drawn great interests targeting low-cost and lightweight applications [108-112]. Among various nanomaterials, single-walled carbon nanotubes (SWNTs) have a unique set of specific properties including high electronic mobility [113], high electrical current carrying capability [88, 114], and ballistic electron transport phenomenon at room temperature [30, 115]. These breakthrough demonstrations of SWNTs, however, have all been based on the direct growth of SWNTs in high temperature chambers without post-assembly processes to

avoid possible degradations during the transfer processes [116-124]. Specifically, two types of transfer processes have been commonly employed for one-dimensional nanostructures. The solution-cast approach starts with the dispersion of SWNTs with liquid to form a nanotube ink, which is later deposited onto a target substrate and dried [119-123]. Nanotubes deposited by this method usually exhibit degraded electrical performance due to random alignment [120, 123], ultrasonic agitation [125], and/or electrical property modifications from the SWNT-solvent interactions [126, 127]. The second approach starts with the synthesis of well-aligned SWNTs with the aid of electrical field [128], gas flow [77, 129], or crystal lattice orientation on the growth substrate [130]. Afterwards, a transfer layer (usually polymer) is deposited and SWNTs are attached to the transfer layer and relocated to a target substrate [131, 132]. The transfer layer is later dissolved or etched away, leaving aligned SWNTs on the target substrate. This approach preserves the originally well-aligned patterns but various chemicals used in the process could affect the electrical properties of SWNTs due to chemical doping and surface adsorption [126]. Here we describe a different approach without the transfer process to allow as-grown SWNTs to be directly placed onto arbitrary substrates with self-aligned patterns such as glass, ceramics and temperature-sensitive substrates including plastics and papers.

3.2.2 Experimental setup

Figure 3.3 illustrates the basic principle and the setup of the synthesis process. Briefly, micro chemical vapor deposition (μCVD) system which is part of the suspended cantilever microstructure [89], is built by means of silicon micromachining processes. Adequate heat transfer design limits the high temperature region to be localized on the cantilever. As such, temperature sensitive target substrate can be placed close to the cantilever without experiencing high temperature damages from the synthesis process. The gap between the top "cap" and bottom μCVD chip forms a narrow gas channel which guides the growth direction of SWNTs over the nearby target substrate. The narrow gas channel also reduces Reynolds number and avoids turbulent flow, which is desirable in this case to effectively guide and align the synthesized SWNTs. At the end of the growth process, the heating power and the gas are turned off to allow the SWNTs to be deposited onto the target substrate.

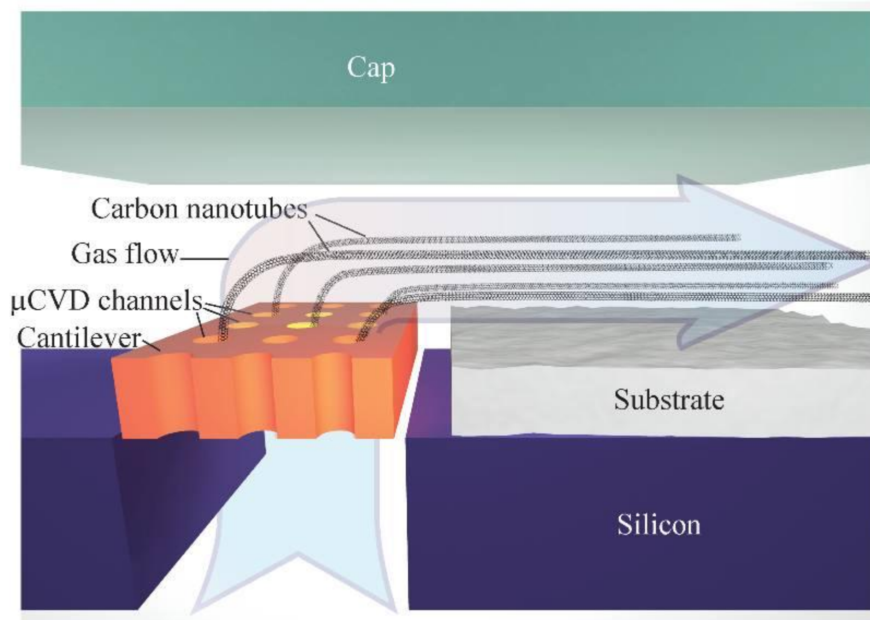

Figure 3.3: Schematic diagram illustrating the direct synthesis of self-aligned SWNTs onto an arbitrary substrate. Nanotubes are synthesized from the μCVD channels at high temperature. The high-temperature region is localized at the suspended cantilever to allow a temperature sensitive substrate to be placed nearby. The gap between the cap and the substrate creates a micro gas flow channel which ensures laminar flow condition. This laminar gas flow guides the growth of nanotubes so that they stay straight and well-aligned. The nanotubes are deposited onto the substrate after the gas flow is turned off.

3.2.3 SWNT growth procedure

Iron nanoparticles are deposited onto the walls of the microchannels by first dipping the whole μCVD chip into 10 mL 0.01 mM iron chloride solution. 100 μL 40 mM hydroxylamine hydrochloride solution is added and stirred. The μCVD chip is taken out of the mixture after 20 seconds, rinsed and dried [65]. The chip is then heated to 800 ℃ for 5 min in oxygen environment in a conventional furnace.

Ethylene and hydrogen carrier gas were provided into the synthesis chamber at a volume ratio of 3:20 from the bottom. The actual mean flow velocity inside the microchannels is estimated to be 0.1 m/s by monitoring the pressure drop across the microchannels (similar to the calculation in Section 3.1.2). The micro cantilever platform was heated to approximately 800 ℃ (the temperature distribution is estimated by a simplified electrical-thermal model, see Chapter 2.2.2 [71, 103]) at its center location for the synthesis of SWNTs under an electrical current of 180 mA and voltage of 17 V. A small aluminum heat sink was placed near the μCVD chip to provide adequate cooling. The total growth time is 10 min.

3.2.4 Characterization of the as-grown SWNTs

As-synthesized SWNTs have been characterized by scanning electron microscope (SEM), Raman spectroscopy, atomic force microscope (AFM), and transmission electron microscope (TEM), respectively. The SEM image in Figure 3.4(a) shows that SWNTs grown from the left-hand-side μCVD unit were self-aligned onto the right-hand-side

silicon structure. Good alignment has been achieved as compared to the one without using the top cap as illustrated in the inset of Figure 3.4(a). This validates the effectiveness of flow control for the alignment of SWNTs. The SWNTs are free of local waviness[77] and two factors could contribute to these advancements. First, laminar flow without local turbulence is achieved as the characteristic dimension of the flow is only tens of micrometers and the Reynolds number is about 15 (Section 2.1.3). Similar phenomena have been reported in macro-scale CVD SWNT synthesis by reducing reaction tube diameter and gas flow rate.[129] Second, the temperature away from the heated microchannels drops quickly to room temperature such that the possible thermal vibration [133, 134] of nanotubes is minimized.

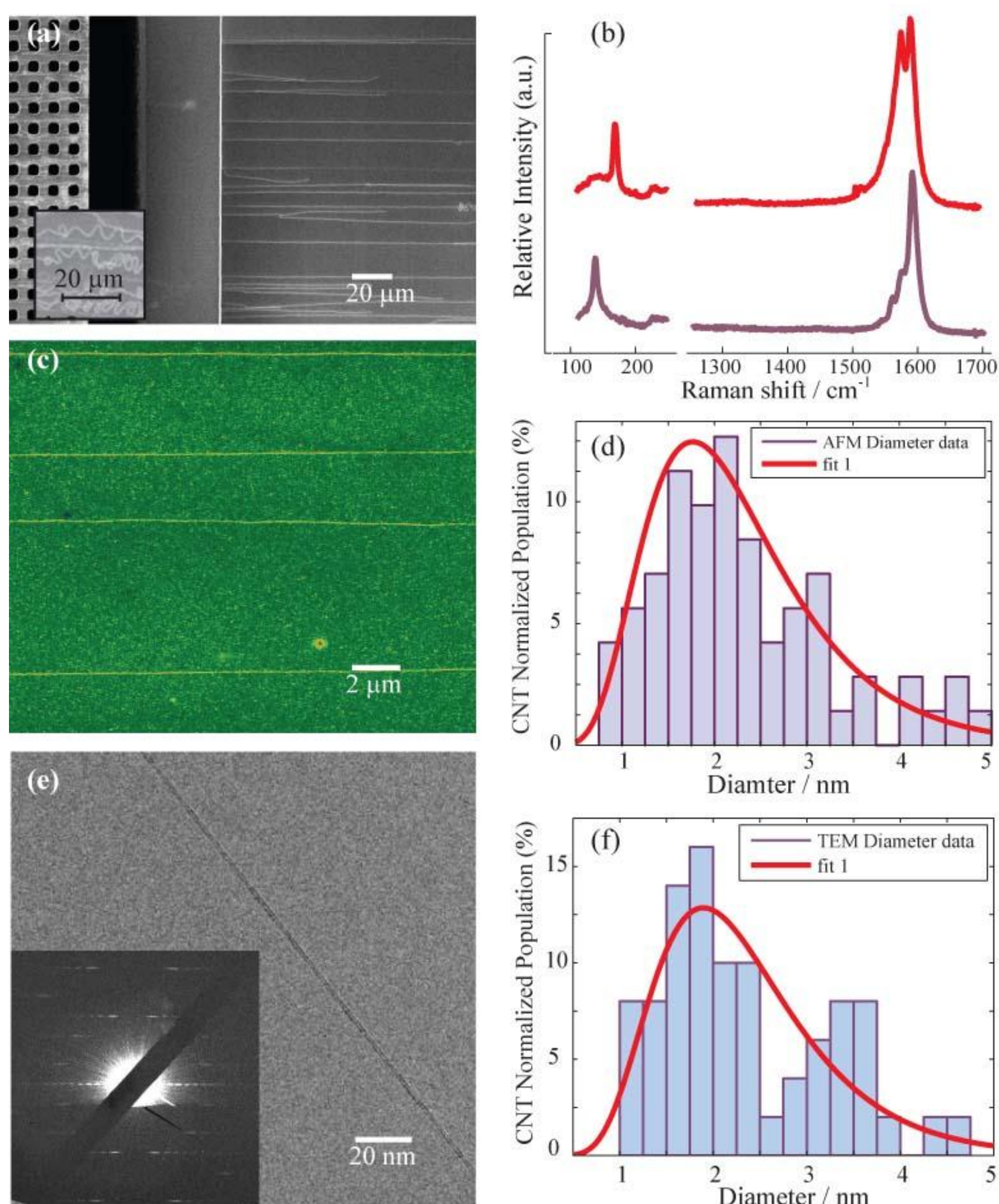

Figure 3.4: Characterizations of the synthesized SWNTs by µCVD. (a) SEM image showing that the nanotubes grown from the left-hand side are deposited and self-aligned on the target substrate at the right-hand side. As a comparison, the inset showed poorly aligned nanotubes without the top cap to regulate the

gas flow. (b) The Raman spectral of the as-grown SWNTs by μCVD. (c) AFM image showing four nanotubes are well-aligned on the substrate without local waviness. (d) Histogram showing the diameter distribution of the SWNTs from 100 samples from AFM measurements. (e) TEM image of an as-grown SWNT. The inset showed its diffraction pattern from which the chirality of the SWNT is determined as (19, 6). (f) The histogram of the diameters of 50 nanotubes synthesized by μCVD from TEM measurements.

The Raman spectra characterization of the as-synthesized SWNTs have been obtained using 633 nm laser at room temperature by a Renishaw® RM1000 spectrometer. Two representative Raman spectra are shown in Figure 3.4(b) with clear G mode peaks at ~ 1580 cm^{-1} and no noticeable D mode at ~ 1350 cm^{-1}, indicating SWNTs with very little defects if any. The radial breathing mode (RBM) of the two spectra at 138 cm^{-1} and 169 cm^{-1} implies the diameters of the nanotubes as 1.78 nm and 1.43 nm respectively (υ_{RBM}=223.5 cm^{-1}nm / d +12.5 cm^{-1} [135]). A typical AFM image with higher spatial resolution than SEM in Figure 3.4(c) illustrates that the nanotubes remain straight and aligned. About 100 nanotubes grown by the μCVD process have been measured by AFM and the diameter histogram is shown in Figure 3.4(d) with a mean value of 2.32nm and standard deviation of 0.93nm.

TEM characterizations of the synthesized SWNTs have been obtained in a JEOL 2100 TEM operated with beam energy of 80kV at room temperature as illustrated in Figure 3.4(e). Here the as-grown nanotube is suspended above the gap region of the μCVD chip (the dark strip in Figure 3.4(a)) to allow direct TEM characterization. It appears to be very clean and the electron diffraction pattern shown as the inset helps to validate the structure as a single-walled nanotube. The nanotube in the picture is (19, 6) and its diameter is calculated to be 1.77 nm. A total of 50 SWNTs with different diffraction patterns have been measured and the histogram of the corresponding diameter is shown in Figure 3.4(f). The peak probability for the diameter of the SWNTs is at around 2 nm with mean value at 2.35 nm and standard deviation of 0.87 nm. These numbers are very close to the AFM characterizations. A total of two double-walled carbon nanotubes were found during the measurement of 50 samples. The results suggest that most of the synthesized carbon nanotubes are single-walled, with little defects, and covered by little or no amorphous carbon in their pristine state.

3.2.5 Direct growth of SWNTs on temperature sensitive substrates

The localized heating of the μCVD provides the possibility to place high quality SWNTs directly onto arbitrary substrates. The optical microscopic image in Figure 3.5(a) illustrates that a piece of copy paper printed with letters "*cal*" from a laser printer was placed right next to the μCVD chip by applying a small amount of grease (Apiezon®, type H). Figure 3.5(b) shows the SEM image of the same area after the synthesis process, where the printed letters are still distinguishable. The close-up view around the letter "*l*" area is magnified in Figure 3.5(c) as SWNTs on paper are difficult to image by SEM due to electron charge effects[105]. The heating platform close to this area in the photo has the appropriate temperature for the synthesis of SWNTs. It is observed that SWNTs maintain good self-aligned patterns with possible obstruction from the surface roughness of the copy paper. A close-up view image is shown in Figure 3.5(d) where two nanotubes can be identified extending from the μCVD platform from the left to the right-hand side copy paper. The two nanotubes stay close to each other with a small gap

distance of less than 1 μm. The alignment is continuous without entanglement even if the shapes of the nanotubes are distorted slightly by the surface roughness of the paper. This is important because entanglement of SWNTs will alter and degrade their electrical properties.[117, 118, 135] Direct growth of SWNTs on plastic substrate (Kapton®, 2 mil tape) has also been demonstrated as illustrated in Figure 3.5(e). It is observed that SWNTs tend to deposit in the bundle format without entangling with each other as illustrated in Figure 3.5(f). Well-aligned nanotubes can also be found on the top glass cap (which is also a low-temperature substrate, see supplementary data) or cap made from sapphire, fused quartz, or single-crystalline quartz. All these results support the feasibility of our synthesis process.

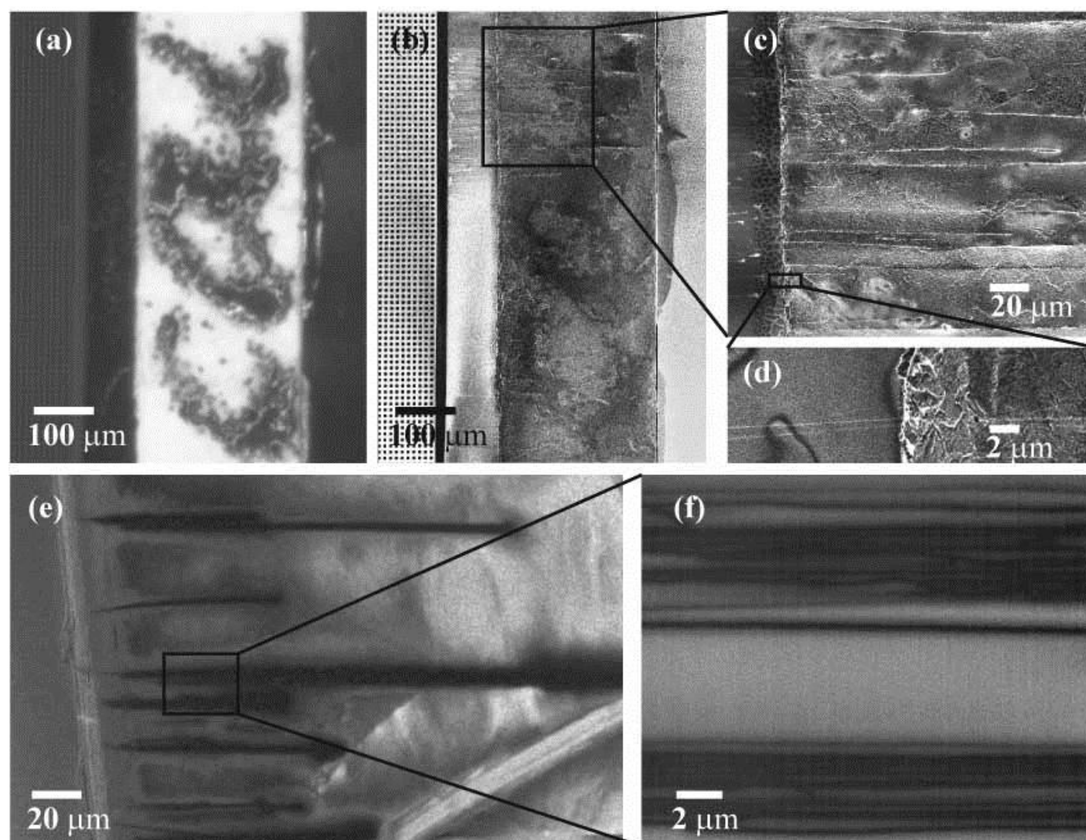

Figure 3.5: Direct growth of SWNTs on paper and plastic substrates. (a) Optical image showing a piece of regular copy paper with letters "*cal*" printed by a laser printer is placed at the right side of a μCVD unit. (b) SEM picture of the same region revealing the existence of SWNTs around the letter "*l*" region after synthesis. (c) SEM picture with higher magnification showing as-grown SWNTs by μCVD deposited onto the copy paper. (d) The alignment of the SWNTs is maintained under the influences of the surface roughness of the copy paper. (e) SWNTs are directly deposited on a plastic tape by μCVD. (f) A closer SEM photo revealing that the nanotubes tend to form bundles but they do not entangle with each other on the plastic substrate.

SWNTs have also been collected on the covering glass cap which is expected to remain near room temperature during the growth process. It is noted that nanotubes are also self-aligned on the glass chip as shown in Figure 3.6.

Another merit worth being pointed out is that the reusability of the μCVD chip. Localized heating suggests that the long SWNTs are all produced with root growth mechanism (the catalyst particles stay on the μCVD heater while the SWNTs stretch out. If catalyst particles stayed at the tip of the SWNTs, they would be cooled down as the nanotube stretches out of the localized heating zone). Therefore, by burning off the nanotubes at the μCVD heater in oxygen environment, the top substrate can be removed (nanotubes on the top substrate is intact due to localized heating) and all the catalyst particles are preserved on the μCVD heater, ready for a second growth process. Experimentally it is observed that fewer nanotubes are grown in the second run, probably due to catalyst contamination. This should be overcome with better growth condition control in the future.

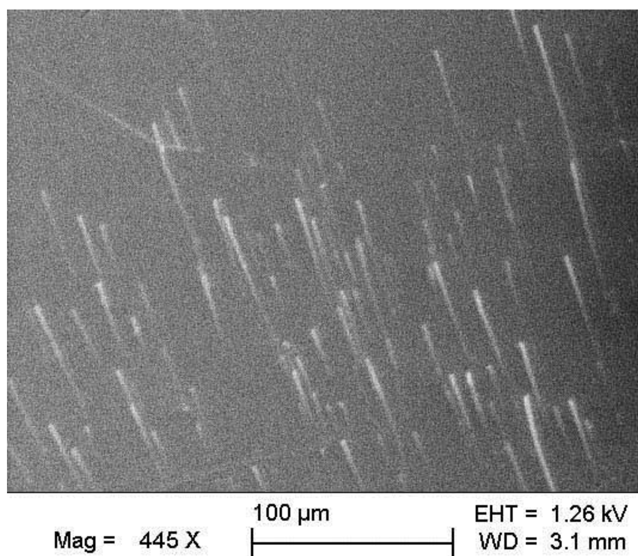

Figure 3.6: A SEM photo showing aligned nanotubes deposited on the top glass substrate.

In conclusion, self-aligned SWNTs up to hundreds of microns in length have been directly grown onto various substrates including paper and plastic. The process does not involve the conventional transfer and assembly process which usually alters the properties of SWNTs. The nanotubes are of high quality in their pristine state, and are therefore suitable for high-performance electronic applications on non-silicon, flexible, low-cost substrates.

3.3 Uniform Graphene Synthesis with Controlled Layer Number

3.3.1 Introduction

Graphene has been commonly referred to as monolayer graphite. Being theoretically studied since the 1940s with the beginning of condensed matter physics [136], its physical existence has not been discovered until 2004 [18]. Since then, it has drawn huge amount of research interests because of its amazing mechanical, electrical and optical properties [19, 45, 137-139].

Chemical vapor deposition has been widely used in microfabrication processes to produce thin films on substrates and has been an important method in the synthesis of various nanostructures [57]. Recently, graphene has been synthesized by CVD process [140, 141]. Graphene acquired from the CVD approach demonstrates low defects so this approach is considered to be a candidate for large scale, low cost and high quality graphene synthesis.

The CVD based graphene synthesis process is described here. A thin layer of nickel (usually a few hundred nanometers in thickness) is first deposited onto a substrate, and then the substrate is put into a furnace to be heated up to about 1000℃ in a hydrocarbon gas environment. The nickel layer then helps the hydrocarbon gas to decompose. The decomposed carbon gradually gets absorbed into the nickel layer. As the solubility of carbon in nickel decreases with temperature, in the cooling process (typically in a few minutes), supersaturated carbon appears on the nickel surface as graphene. However, graphene layer synthesized by this method is not uniform as carbon prefers to segregate at the nickel grain boundaries, and will easily form multi-layer graphene or graphite [142]. Using copper foil instead of nickel film can resolve this problem [141], but only monolayer graphene can be acquired. It is usually desired to have some control on the number of graphene layers. For example, Bilayer graphene is desired in many applications because it has a tunable band gap [137, 138, 143].

It has been reported that quick cooling rate can help to suppress the preferential carbon segregation on nickel grain boundaries, thus form a consistent number of graphene layers [140]. Currently the best result achieved is mono- or bilayer graphene of up to about a hundred square microns.

Benefiting from scaling effects, the μCVD system, as described in Chapter 2, has several advantages over the conventional CVD system such as agile temperature control, fast gas species exchange, steady laminar gas flow and enhanced gas mass transport. Each of these advantages opens up new possibilities for potential applications in material synthesis. For example, graphene synthesis mentioned above prefers a high cooling rate to suppress the carbon segregation at nickel grain boundaries. Because μCVD provides a cooling rate which is several orders of magnitude higher than the conventional CVD system, it is used in this paper to obtain a uniform number of graphene layers.

The basic concept of using μCVD in graphene synthesis is shown in Figure 3.7.

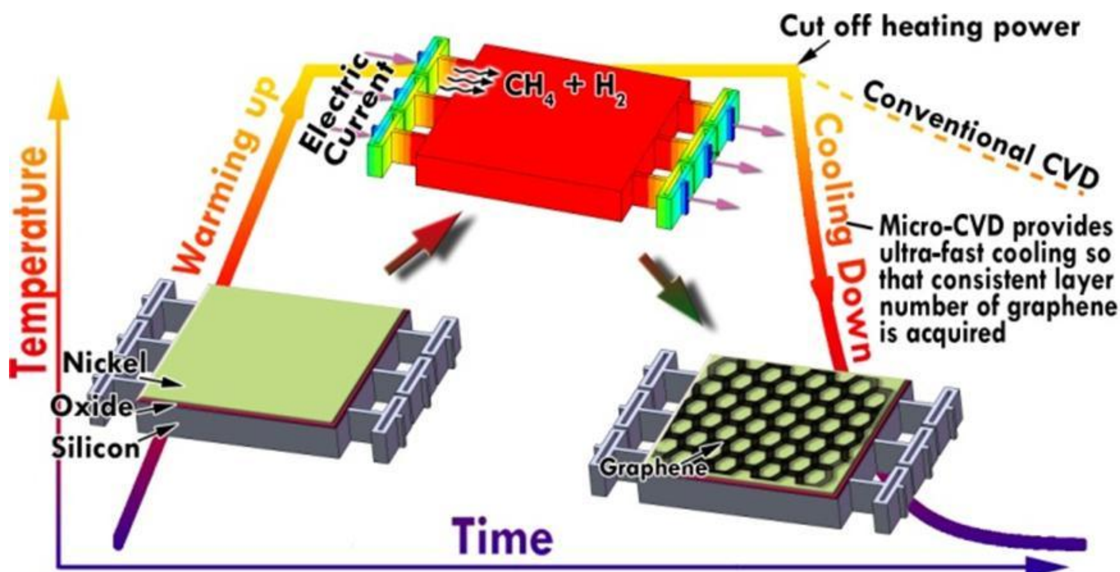

Figure 3.7: The basic concept of graphene synthesis using μCVD shown in the temperature versus time diagram. The ultrafast cooling rate provided by the μCVD system promotes the controlled growth of graphene.

3.3.2 Experiments

The device fabrication follows the standard DRIE on SOI wafer process described in Chapter 2.3. In the end, a 300nm-thick nickel layer is deposited by e-beam evaporation. A photolithography is performed and the nickel and silicon oxide on the contact pads are etched away to allow electric contact to be made to the supporting anchors (Figure 3.8).

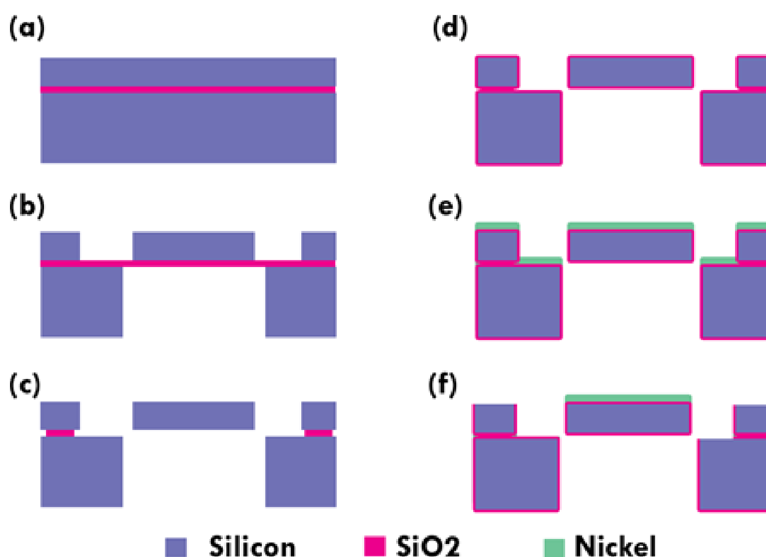

Figure 3.8: Fabrication Process of a μCVD chip for graphene synthesis. (a) Start with a SOI wafer. (b) Back-side opening and front side etch for heating stage and supporting beams. (c) Structure release in buffered HF solution. (d) Thermal oxidation to grow 200nm silicon oxide layer. (e) Evaporate 300nm thick nickel layer. (f) Etch away nickel and silicon oxide on anchors.

The synthesis process is done at one atmosphere pressure. First hydrogen gas is used to flush the chamber for 30 minutes. Then a small electrical voltage is applied to the μCVD chip. The temperature of the heating stage rises because of joule heating. The voltage is gradually increased until the chip shows mild red color where the temperature is measured to be 800 ℃ (See Section 2.4.2 for measurement). The chip is kept in the hydrogen environment for 20 minutes to remove any possible native oxides due to previous exposure to air. This annealing step also helps the evaporated nickel to crystallize. After this, the voltage is increased again, until the heating stage shows a bright orange color with a temperature of 1000 ℃. The voltage applied at this point is 13.2V and the current is 325mA. After that, methane is introduced as the carbon source. The volume ratio of methane to hydrogen is 1.5%. By interaction with the nickel layer, methane will decompose and the resulting carbon can dissolve into the nickel layer due to a relatively large solubility of carbon inside nickel. The amount of carbon absorbed by nickel is controlled by how long the chip is exposed to methane. After five minutes, the heating power is cut off to quickly bring down the temperature of the heating stage, so methane decomposition stops and the carbon can precipitate as graphene layers.

3.3.3 Characterization of Synthesized Graphene

As one of the routine methods, Raman spectroscopy is used to characterize the synthesized graphene [144]. Raman spectroscopy probes the crystal lattice vibration modes by measuring the frequency shift of reflected photons relative to the original incident ones. Important information about the material can thus be learned. In the graphene case, usually we are interested in 3 frequency shift peaks, called G-band at ~1580 cm^{-1}, D-band at ~1350 cm^{-1}, and 2D-band at ~2700 cm^{-1} respectively. D-band is often referred to as the "defect" band. Its intensity indicates the number of defects inside a graphene sheet. The intensity ratio of G-band to 2D-band is used to determine the number of layers for the synthesized graphene. For a single layer of graphene, 2D-band will have a much larger intensity than G-band; and for multiple-layer graphene, G-band will surmount 2D-band.

Figure 3.9(a) and Figure 3.9(b) show a typical optical microscopic image and SEM photo of the platform after the synthesis process. The Raman spectrum at the crosshair position in Figure 3.9(a) is recorded as the top curve in Figure 3.9(c). The non-negligible D-band indicates the existence of defects. This makes sense intuitively, because high cooling rate eliminate the opportunity of annealing. Annealing exists naturally in the conventional CVD process because of the long cooling time and thus might help to reduce the occurrence of defects. The intensity ratio of G band and 2D band is about 1, which indicates that bilayer graphene structure is obtained. We randomly measured tens of positions on the platform and their Raman spectra show similar features throughout the whole $300 \times 300 \mu m^2$ area (three other Raman spectra are also shown in Figure 3.9(c). It is easily observed that all the curves are in great consistency. As a comparison, Raman spectra of a furnace grown graphene sample are shown in Figure 3.9(d). It is easy to notice that the spectra have very small D-band intensity, and thus show a better graphene quality. However, the features of the spectra vary when a different measurement position is chosen. This indicates that the uniformity of the graphene layers obtained from the conventional CVD process is much worse than the μCVD system. The result verifies that ultra-fast cooling of the nickel layer successfully controlled the number of graphene

layers on a large area (about 10^5 square microns instead of previously about a hundred square microns [140]).

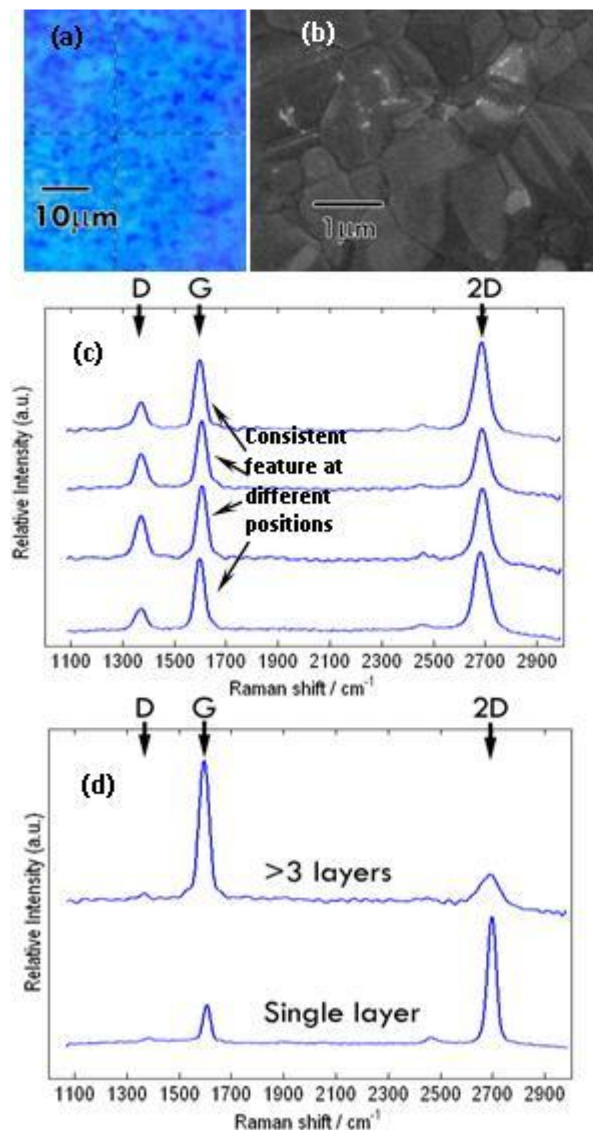

Figure 3.9: Raman spectra analyses. (a) Optical microscope photo showing an area of CVD chip after the graphene synthesis. (b) A SEM image. The nickel grain boundaries are obvious and they could cause the non-homogenous color in (a). (c) Raman spectra - the top curve is taken at the crosshair position in (a). Other curves, with great consistency, are from other random positions on the micro platform. (d) Raman spectra of a furnace grown graphene sample we have processed as a reference. It shows inconsistent number of graphene layers at different positions.

3.3.4 Discussion

μCVD has several distinctive advantages over the conventional CVD systems due to scaling effects. The miniaturized system has an exceptionally small heat capacity, so the thermal time constant is orders of magnitude shorter than that of a conventional CVD

system. This advantage brings μCVD into the application of graphene synthesis, where high cooling rate could be preferred to form uniform layers. In the preliminary experiment, a thin nickel layer is heated to ~1000 ℃ in hydrocarbon gas environment and cooled down at about 4 orders of magnitude faster rate than a conventional CVD system. The obtained graphene film shows great uniformity of bilayer graphene Raman feature across the heating platform. However, due to the lack of annealing, the film also has more defects than those synthesized from the conventional CVD process. This problem might be overcome by using an electrical controlled circuit to reduce the cooling rate (i.e. rather than directly cut off the power supply, the heating voltage is gradually reduced down to zero in a controlled manner). To measure the electrical transport properties and to make the synthesized graphene layer of practical use, one future work is to transfer the graphene to an insulating substrate and to construct electrical contacts.

Chapter 4

Conclusions and Future Directions

4.1 Conclusions

The preceding chapters have served to illustrate the construction of the μCVD system and its potential applications in the synthesis of nanomaterials. The concept of the μCVD system is proposed and verified experimentally in this work with distinctive advantages as compared with the conventional atmospheric pressure CVD system, including: (1) agile temperature control, (2) fast gas species exchange, (3) steady laminar gas flow and (4) efficient gas mass transport. These advances are made possible by the miniaturization of the CVD system. The theoretical analyses on effects of scaling are presented in chapter 2 to illustrate that some parameters of the μCVD system are different than those of the macro scale CVD system by orders of magnitude. Chapter 2 also addresses the setup of peripherals around the μCVD chip. Among them, the construction of the temperature monitoring and control system is time-consuming and could have many further improvements. The implementation the μCVD system further requires considerable amount of engineering as presented in chapter 3. The most challenging work include the design of the μCVD chip, including the considerations of gas flow, heat generation and management, nanostructure growth mechanism, and feasible micromachining processes. Prototype experiments have been conducted to demonstrate various capabilities. In the experiment of carbon nanotube synthesis in chapter 4, the effects from enhanced mass transport allow μCVD to have a wider choice of gases used in the synthesis process. The ability to make fast temperature adjustment made the synthesis of ultra-long carbon nanotubes possible. The acquired nanotubes are characterized to be single-walled, free of amorphous carbon with limited defects. These good characteristics are the results of efficient mass transport and uniform gas temperature distribution. Synthesized carbon nanotubes have been demonstrated to be deposited directly onto temperature sensitive substrates such as paper via the μCVD system. Because the process does not involve the use of liquid which is commonly required in other CNT transfer processes, SWNTs are protected to stay in the pristine state. The μCVD system has also been applied to the synthesis of two-dimensional nanostructures in the graphene growth experiments. Experimentally, good uniformity has been achieved in the synthesis of graphene on top of deposited nickel thin film. These present the current accomplishments by using μCVD system to synthesize nanomaterials which could be the foundation for future applications.

4.2 Future Directions

4.2.1 Patternize carbon nanotubes

Well-controlled nanomanufacturing, such as the direct deposition of one-dimensional nanostructures with controllability over size, orientation and position is presently not possible. Single-walled carbon nanotube has many unique properties for various applications but it is difficult to control its growth pattern and orientation. Previously,

researchers have demonstrated that CNTs can be randomly synthesized on a substrate [145], or aligned by guiding fluidic flows [146], electrical fields [133], and crystalline orientations [66]. Recently, SWNT serpentines were constructed on crystalline substrate under the guidance of gas flow [147]. In contrast to the aforementioned attempts, it will be interesting to investigate if the µCVD system can accomplish: (1) a direct-write process including both synthesis and deposition of CNTs onto a second substrate; (2) combination of gas flow and mechanical movement to actively control their deposition position and orientation; and (3) feasibility for depositing CNTs on arbitrary substrates including non-flat surfaces. Figure 4.1 illustrates the possible experimental setup where a target substrate is placed above the MEMS µCVD system to allow the passage of the guiding gas flow. An electrical field is applied in the vertical direction toward the µCVD to guide the growth of nanotube to the top substrate. The target substrate is controlled to be movable for possible position and pattern controls of the CNTs. The application of the µCVD system makes this possible because the heating is localized such that the top target substrate or the bottom µCVD system can be connected to a nanopositioner to control the fine movements at room temperature environment while the µCVD itself could be at a high growth temperature. Results from this future experiment can inspire different applications based on the µCVD system.

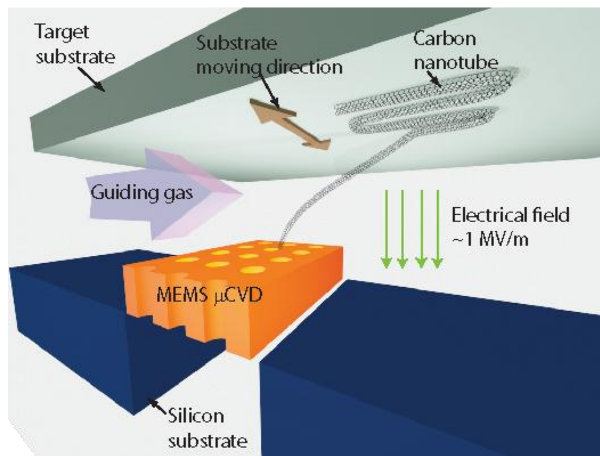

Figure 4.1: The concept of direct writing carbon nanotubes.

4.2.2 The interaction of carbon nanotube and the substrate

The alignment of carbon nanotube is observed on single-crystalline quartz [148], indicating strong substrate interactions with nanotube growth. However debates persist on the growth mechanism. For example, one hypothesis postulates that the catalyst is sliding along the crystal orientation in liquid form at high synthesis temperature [66]; while another hypothesis contradicts this finding because the experimental facts suggest that the nanotube has a floating tip high above the substrate during the growth [147]. Therefore, the interaction must be between the SWNT and the substrate, instead of between the catalyst and the substrate. This ambiguousness could be clarified by conducting experiments using the µCVD system because of the localized heating process would only generate root-growth, long SWNTs to reach the target substrate. The tip-growth SWNTs can only grow to a short distance as the catalyst at the tip could be cooled before reaching the target substrate in the room-temperature chamber.

Furthermore, the van der Waals interaction between the SWNTs and the substrate could be studied by adjusting experimental parameters in the μCVD system. Specifically, four different forces can exist during the direct-write CNT process by μCVD as illustrated in Figure 4.2, including (1) force coming from the gas flow, which can be adjusted by the flow velocity, (2) electrostatic force from the electrical bias, which can be adjusted by the field strength, (3) mechanical spring force of the CNT, and (4) local van der Waals force. The interaction of these forces will determine the final deposition position, orientation and speed of the CNT such that they should be studied both analytically and experimentally. For example, the gas flow could create an energy field such that that each CNT will maintain the lowest energy configuration following the gas flow direction as illustrated. The deposited CNTs could align with the gas flow. However if the gas flow is weak, the local van der Waals interaction could dominate the deposition orientation of the deposited CNTs. By varying the guiding gas flow rate and observing the geometry of the deposited CNTs while keeping same values for all other parameters, one could investigate the strength of the van der Waals interaction.

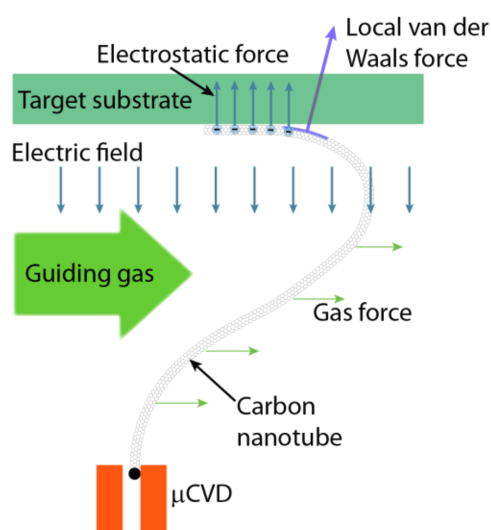

Figure 4.2: Utilizing μCVD for the study of nanotube-substrate interaction.

4.2.3 Relationship between nanotube diameter and growth temperature

It has been reported that the diameter of CNTs can be altered by the growth temperature [149]. However this finding contradicts the common understanding that the synthesis of SWNTs follows the original chirality which is thermal-dynamically favorable. For example, previous experiments have shown that one nanotube can be cut into many segments and "cloned" independent of the synthesis temperature [67]. While some researchers found that the diameter increases with synthesis temperature [150], some other researchers stated that the diameter decrease with growth temperature [149]. In general, most researchers believe that the quality of the SWNTs is affected by the growth temperature rather than their diameter [151]. The difficulty of finding collaborating evidences in the aforementioned results is that the process parameters could change from one growth process to another, including the diameter of the catalyst, local gas flow pattern, position of the sample in the furnaces, possible contaminations, and the

deposition of amorphous carbon in the reaction chamber. These factors could all potentially affect the SWNT diameter and it is difficult to study the temperature effects in a regular furnaces with multiple experiments by only changing the synthesis temperature [152].

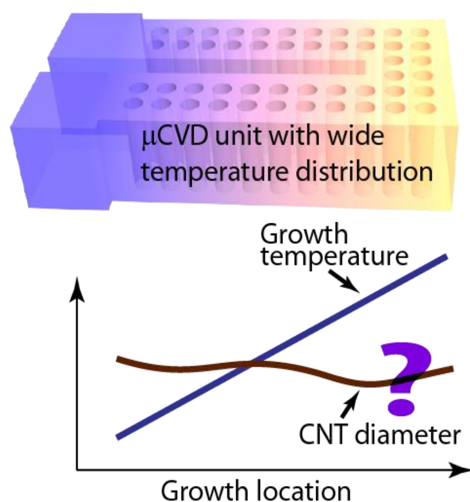

Figure 4.3: Studying the relation between the CNT diameter and the growth temperature using µCVD.

µCVD could serve as the platform to explore the temperature effect for the synthesis of CNTs. The platform is designed to have a wide temperature distribution across a very short length as illustrated in the top diagram in Figure 4.3 such that the possible variations of the other growth parameters could be minimized while the effects of temperature could be studied. After the growth process, the acquired SWNTs can be directly characterized on the µCVD growth chip by TEM without being removed and re-deposited onto TEM grids. The diameters of CNTs can be plotted with respect to the growth location and temperature as illustrated in the bottom diagram in Figure 4.3. TEM serves as an excellent tool for the nanotube diameter measurement because the exact chirality of a nanotube can also be decided by its electron diffraction pattern.

Appendix A Mechanical Assembly for µCVD system

A.1 µCVD Chip Holder and Electrical Interface

The µCVD chip is first fixed on a printed circuit board (PCB). This board serves both as electrical and gas interface for µCVD chip as illustrated in Figure A.1. Ultrasonic wire bonding is used to make electrical connection from the PCB to the µCVD chip.

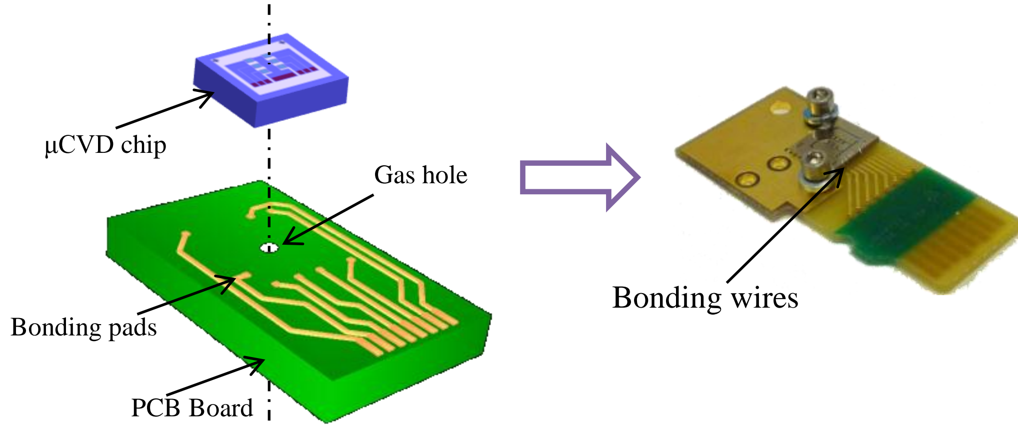

Figure A.1: The assembly of µCVD chip on its chip holder.

The board is then inserted into a microSD™ card connector (3M®, 2908-05WB-MG), which is soldered to the surface of another PCB. All the incoming electrical wires are connected to this PCB. This PCB also provides mechanical support for gas interface components, as described in the next section.

A.2 Gas System for Flow and Pressure Control

The concept of gas flow monitoring and control for the µCVD system is illustrated in Figure A.2. The gas flow rate in a microchannel can be calculated by the pressure drop Δp across it [81]:

$$v_m = \frac{r_0^2}{8\mu}\frac{\Delta p}{L_{mc}} \tag{A.1}$$

where μ is the gas viscosity, r_0 is the radius of the microchannel, and L_{mc} is the length of the microchannel. Experimentally, a differential gauge (Dwyer® Magnehelic® 0~5 inH_2O pressure) is used to measure the pressure drop. The two inputs of the differential pressure gauge are actually connected to the backside opening underneath the testing µCVD chip and to the testing chamber respectively. The pressure drop across an individual microchannel should be close to the measured value since the microchannels experience much larger flow resistance than macro-sized gas lines. Similar to connecting two electrical resistors in serial, the voltage drop across the resistor with much larger resistance is close to the total applied voltage.

The pressure drop is adjusted by a needle valve. It is observed in Figure A.2 that when the needle valve is completely closed, the entire gas has to flow through the μCVD chip. While

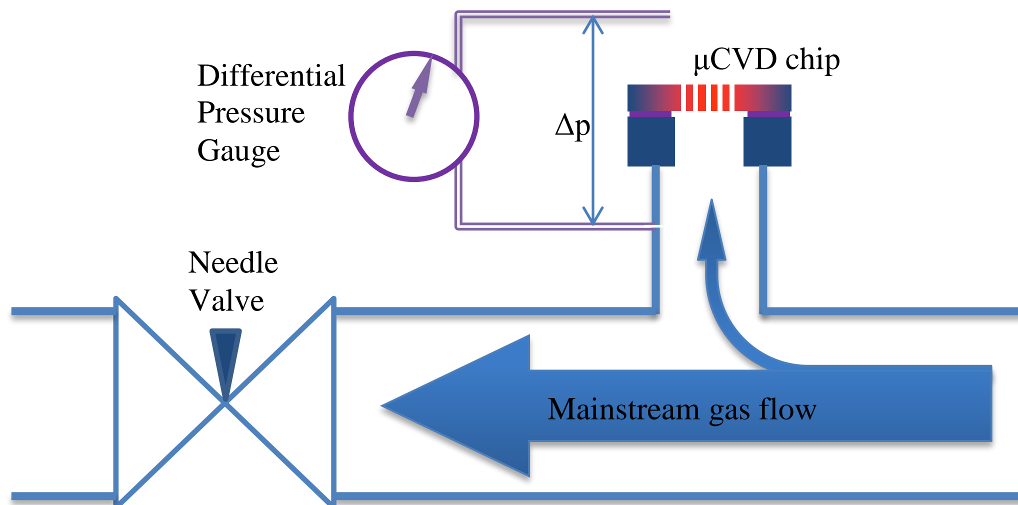

Figure A.2: Gas flow control diagram. The gas flow rate through the microchannels of the μCVD chip is monitored by the differential pressure gauge, and can be adjusted by the needle valve and the total gas flow rate.

It is preferred that the space between the mainstream flow and the μCVD chip is as small as possible so that the gas from mainstream can reach the microchannels quickly. This is important for reactant gas switching in some processes like carbon nanotube synthesis. In this process, the oxidized nanoparticle catalyst is first reduced in hydrogen gas flow at high temperature and then hydrocarbon gas is introduced for nanotube growth. It is found that prolonged exposure (> ~ 5 min) of the catalyst in hydrogen at high temperature will result in degraded growth results.

To reduce this space, direct gas coupling is utilized in the design by eliminating any commercial gas tubes or joints. First, the μCVD chip is directly fixed onto the previously mentioned PCB which has a through hole for gas to flow through (Figure A.1). Usually photoresist (OCG 825) or thermally conductive encapsulant (Dow Corning® 3-6752) is used between them to construct an airtight joint. An O-ring is placed between the chip holder PCB and the main PCB to form a good seal (Figure A.3). The O-ring is permanently glued onto the main PCB so that changing chip holder between experiments is convenient. A gas hole is also drilled on the plastic tube, which is pressed against the main PCB by an aluminum holder so that the gas from the mainstream flow in the plastic tube can flow directly through the two PCBs and reach the μCVD chip. A small amount of sealant (Loctite® 80724) is used to form a good seal between the plastic tube and the main PCB. The aluminum holder is fixed onto the main PCB by four 4-40 machine screws.

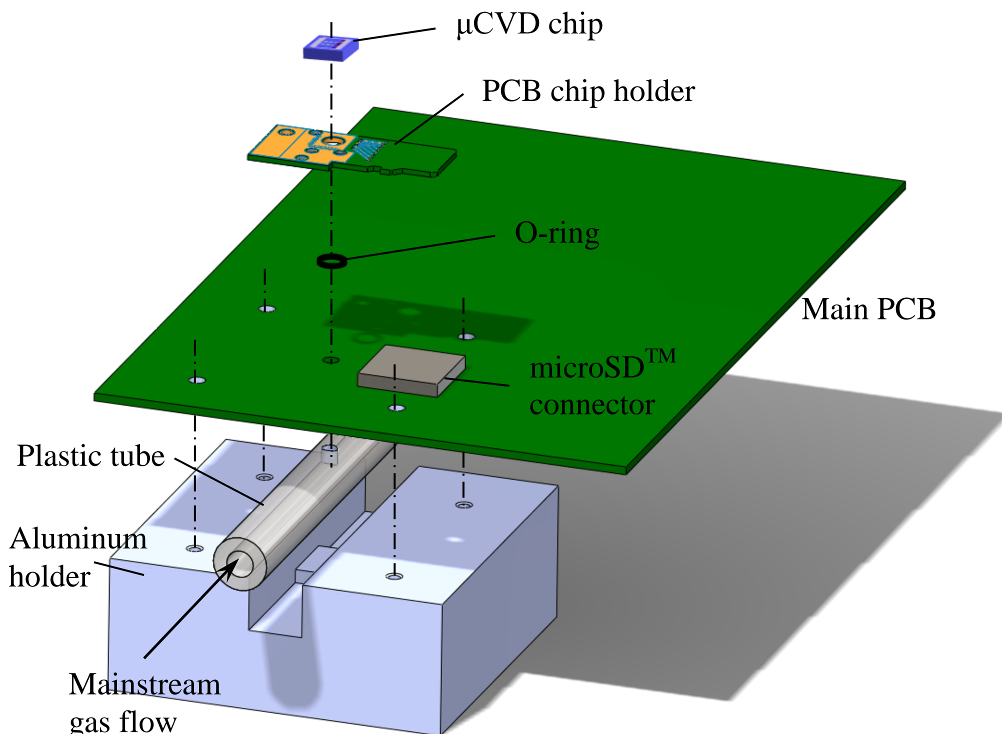

Figure A.3: Direct coupling to reduce the space between the μCVD chip and mainstream gas flow.

The space between the mainstream flow and the μCVD chip in this direct coupling design can be estimated as:

$$V \approx \pi r^2 (t_{\text{plastic tube}} + t_{\text{main PCB}} + t_{\text{O-ring}} + t_{\text{chip holder PCB}}) \quad \text{(A.2)}$$

Here r is the radius of the gas holes and is approximately 1.5 mm, and t denotes the thickness of various layers. The volume is calculated to be ~ 30 mm^3. For some of the μCVD chip design, only around 2000 microchannels with a diameter of 5 μm are present, and if assuming 100 mm/s mean flow velocity (See Chapter 2 for flow analysis in microchannels), the total flow rate is 4 mm^3/s. As a result, the gas exchange time is $\frac{30\text{ mm}^3}{4\text{ mm}^3/\text{s}} \approx 10\text{ s}$. This is small enough compared to the 5 min limit stated previously and should therefore not affect the growth results. Notice that a commercial joint such as a barbed tube tee usually occupies a volume on the order of 1 cm^3, which could extend the gas exchange time to ~ 200 s.

Finally, differential pressure gauges, needle gas valves are all assembled together with a home-made vacuum chamber. The vacuum chamber insulates the μCVD system from the outside environment and provides the capability of varying CVD pressure. The system diagram is shown in Figure A.4.

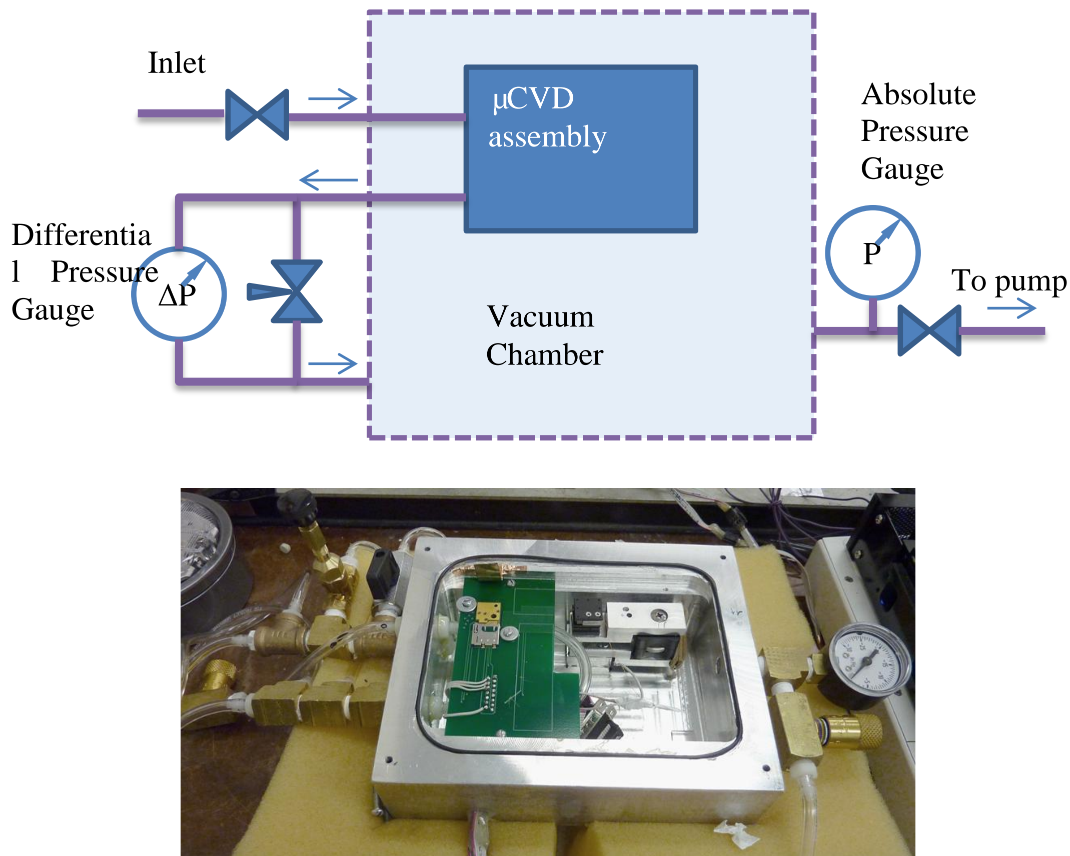

Figure A.4: Gas control system diagram and an optical photo of the home-built system.

A.3 Mechanical Assembly of Nanopositioner

A "cap" is located above the μCVD chip, with two slices of plastic tape between them which serves as spacers (Figure A.5). As a result, the nanomaterials grown from the μCVD chip can deposit directly onto the cap. If the cap moves during this process, the nanomaterials can follow its moving trace and be patterned.

A nanopositioner is used to manipulate the cap - the target substrate where the synthesized nanomaterial is collected. The assembly drawing of the nanopositioner can be found in Figure A.5. The optical image of the nanopositioner can also be found in Figure A.4. The nanopositioner can control the horizontal x-y movement of the target substrate. The target substrate is first suspended by a slice of double sided sticky tape which sticks on the connecting PCB. The connecting PCB is assembled onto the nanopositioner by machine screws. Initially, the bottom surface of the target substrate is ~ 1 mm away from the top surface of the μCVD chip during the assembling of system. Later, the target substrate is brought into contact with the spacers on the μCVD chip by a z-directional stage (Newport® 9201 Tiny Lab Jack) located at the right hand side of

Figure A.5. Lubricant (Apiezon®, type H) is applied between the target substrate and the spacers so that the target substrate can still move horizontally above the μCVD chip. However in vertical direction, the position of the target substrate relative to the μCVD chip is only decided by the spacer and is irrelevant to the position of connecting PCB. This is because the double sided sticky tape serves as flexible hinges to accommodate the vertical vibration while still offers sufficient horizontal rigidity to nudge the target substrate horizontally. This design significantly reduced the possible influence from the vibration of the whole system and the connecting PCB. Finally an electrical conducting wire connects the main PCB and the connecting PCB to provide high voltage (~1 kV). This high voltage is subsequently applied on the ITO layer of a quartz chip through a conductive tape. The ITO layer is only ~10 nm thick so it exhibits a high sheet resistance of ~ 1 kΩ/sq. However this is sufficient for the purpose of providing a plane with equal electrical potential under zero current flow. A strong electrical field (~1 MV/m) could therefore be built between the μCVD chip and the ITO layer to guide the growth of nanotubes or nanowires. The thin ITO layer also allows infrared light to pass through (thick ITO layer with a low sheet resistance is not transparent to infrared light [153, 154]), which makes non-contact temperature measurement possible. The ITO film is used with the optical temperature measurement system and is proved to not affect the measurement results.

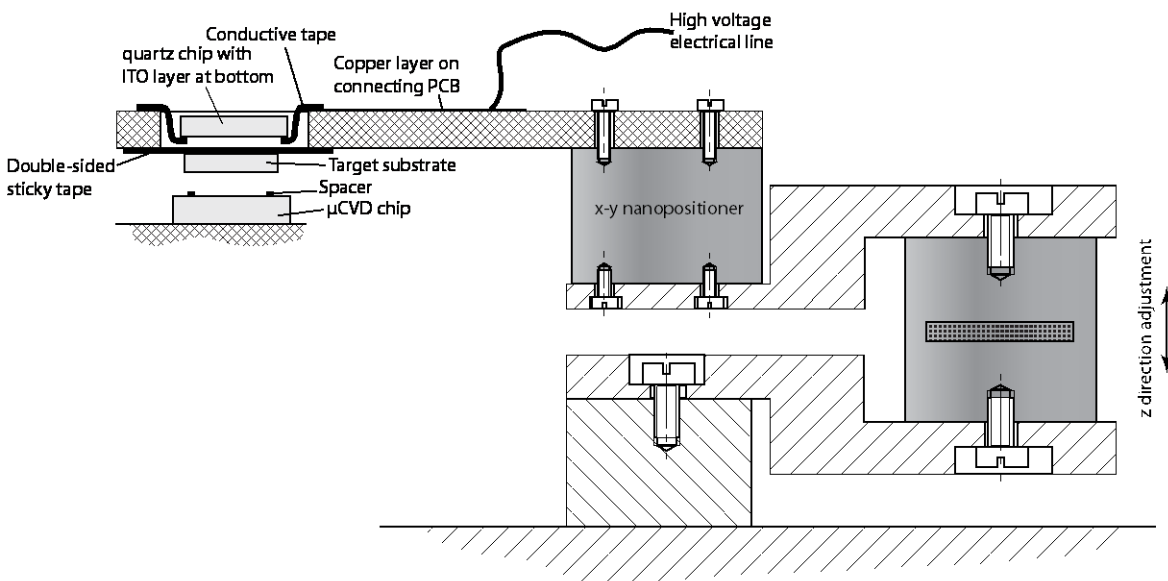

Figure A.5: The assembly drawing of the nanopositioner.

A.4 Optical Monitoring Glasses

The optical windows are embedded in the top cover of the vacuum chamber to allow direct observation and optical temperature measurement. The design considerations are: 1) Mechanically they should stand 1 atm differential pressure between the two sides; 2) Optically they should allow light with wavelengths from approximately 600 nm to 2200 nm to come through. Sapphire windows are chosen because they are transparent for wavelengths from 150 nm to 5000 nm. The mechanical strength of the windows is

simulated in ANSYS® to ensure a safety factor of at least 2. The assembly drawing of the top cover of the vacuum chamber is shown in Figure A.6.

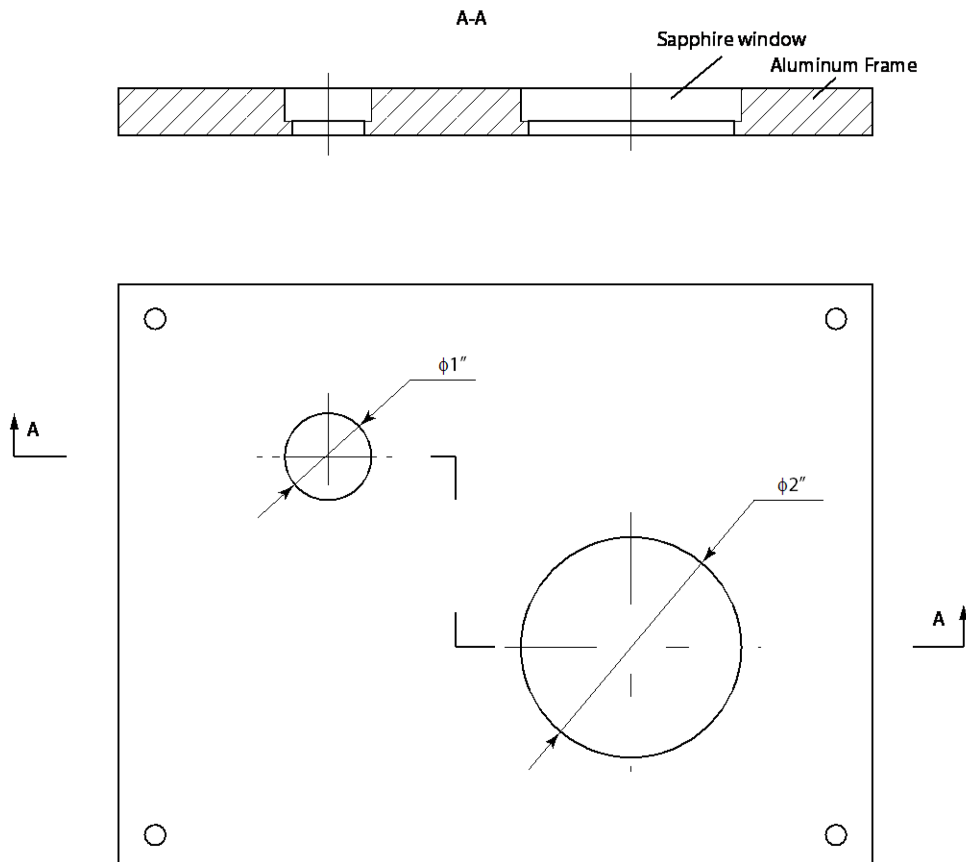

Figure A.6: Assembly drawing of the top cover of the vacuum chamber.

Appendix B Design of the Temperature Monitoring System

B.1 Optical Design

Optical design solves the problem of how the radiation from the light source is coupled to the photodetector. The easiest way is direct coupling.

B.1.1 Direct coupling

Direct coupling simply aligns the photodetector with the light source as Figure B.1.

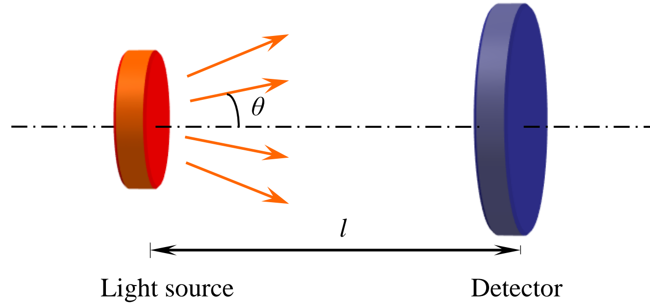

Figure B.1: Schematics of direct coupling.

The power input on the photodetector can be calculated as follows. Assume the light source to generate radiation power I per unit area, as described by Equation (2.13). The power j radiated from a small area ds to a small solid angle $d\Omega$ should obey:

$$ds \cdot I = ds \int j d\Omega = ds \cdot 2\pi \int_0^{\pi/2} (j_0 \cos\theta) \sin\theta d\theta \qquad \text{(B.1)}$$

This gives

$$j = \frac{I}{\pi} \cos\theta \qquad \text{(B.2)}$$

When the photodetector is aligned with light source and their size is much smaller than their distance, cos $\theta \approx 1$. For an area $d\sigma$ on photodetector, the power it intercepts from the light source ds is:

$$dP = d\sigma \cdot j \cdot d\Omega = j \cdot d\sigma \cdot \frac{ds}{l^2} = \frac{I}{\pi l^2} d\sigma ds \qquad \text{(B.3)}$$

The total power density impinged on the photodetector is therefore:

$$I_D = \frac{\int_{\text{total area of light source}} dP}{d\sigma} = I \frac{A_l}{\pi l^2} \qquad \text{(B.4)}$$

where A_l is the area of the light source.

An estimation of the power density I_D for a real experiment is given below. The heating area of μCVD chip for graphene synthesis is 300×300 μm^2. The power density of the light source can be estimated by the Stefan-Boltzmann law Equation (2.13). I_D is therefore:

$$I_D = 5.7 \times 10^{-8} \text{Js}^{-1}\text{m}^{-2}\text{K}^{-4} \times (1000\text{K} + 273.15\text{K})^4 \times \frac{300\mu\text{m} \times 300\mu\text{m}}{\pi \times (2\text{cm})^2} \approx 10\text{W/m}^2 \qquad \text{(B.5)}$$

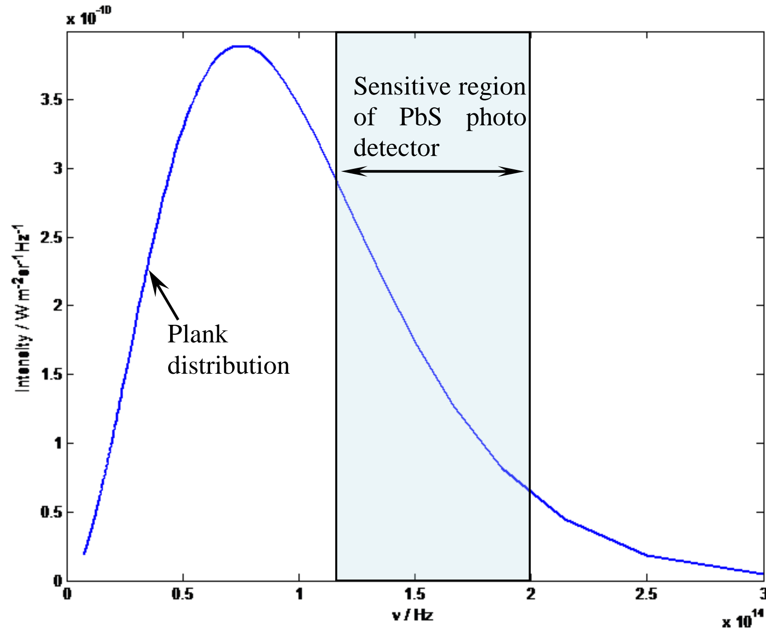

Figure B.2: The sensitive region of PbS detector in relative to a 1000 ℃ black body radiation spectrum

Several factors should be considered to get the actual effective power density. Usually a photodetector only responds to a certain portion of the spectrum. As can be observed in Figure B.2, the sensing region of a PbS detector covers the wavelength from 1.5 μm to 2.5 μm. Therefore only approximately 30% of the total power is effective in generating detectable signal for the PbS sensor by counting the ratio of the area below Plank distribution curve within sensitive region to the total area below Plank distribution curve. There is also reflection at both sides of the observing sapphire window (See Chapter A.4 for window design) which can be calculated by Fresnel equation:

$$R = \left(\frac{n_1 - n_2}{n_1 + n_2} \right)^2 \tag{B.6}$$

where n_1 and n_2 are the refractive indexes for two different materials respectively. Here $n_1 = 1$ for air, and $n_2 = 1.75$ for sapphire. Using this equation, a total of 15% energy is reflected by the two sides of observing window. Finally, the heater is not an absolute black body. The emissivity of heavily doped silicon (in the case of bare heater) and nickel (in the case of being coated for graphene growth) is 0.85 and 0.2 respectively at around 1000˚C. Considering all these effects, the actual delivered power on photodetector is about 2 W/m^2 and 0.5 W/m^2 for bare heater and for nickel coated heater respectively.

This power level has unfortunately exceeded the linear region of sensor (Figure B.3). Allowing the sensor to work in this region will invalidate the initial motivation of building a two-color detection system: measured intensity ratio at the two different wavelengths is independent of the relative position between the emitter and detector. Another problem found during the experiments is that the radiated power will heat up the

detector. Although no apparent influence has been observed on the silicon p-n junction based photodetector, but the temperature variance dramatically alters the free carrier concentration generated by thermal excitation in PbS detector. These thermally generated free carriers will contribute to the detected photocurrent and affect the measured radiation power. Experimentally, continuously rising of PbS detector signal is observed while the signal from silicon detector keeps constant. A more detailed analysis on the two-color detector will be carried out in the circuit design section.

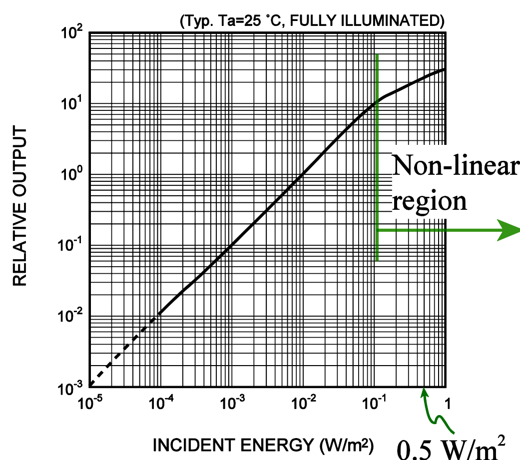

Figure B.3: Response curve for PbS detector (data from Hamamatsu® 1713-01 photodetector datasheet).

The light intensity has to be attenuated to keep the photodetector working in linear region and to reduce the temperature effects. An easy way is to relocate the detector further away from the light source. This approach does not change the radiation spectrum and is therefore chosen in experiments. Black rubberized fabric (Thorlabs®, BK-5) is used to block the ambient light and also to absorb any radiated light impinging on it so that it will not be reflected to enter the detector. The detector is brought to approximately 10 cm away from the light source. The power density therefore reduces in reverse proportion to the second power of distance, to about 1/25. This cut the power density to below 0.1 W/m^2 so that the photodetector works in its linear region.

However, the light intensity problem is not completely solved. The photodetector's incoming light intensity becomes very weak when the μCVD heater is working at lower temperature such as 750˚C. This temperature is however indispensable for catalyst nanoparticle calcination in carbon nanotube growth experiments. The infrared light signal drifts significantly from temperature variation caused by placing the detector by hand each time (see section B.2.2). To circumvent this, the photodetector should be fixed in a temperature stable region while the radiation from μCVD heater can still reach it. This is realized by applying optical fiber so that sensor positioning and radiation measurement is separated.

B.1.2 Optical fiber coupling

Assume the light source is on the axis of the optical fiber. If the light that enters the optical fiber is within its numerical aperture limit, it is all transported to the photodetector. This is the case in our setup because the light source, or micro heater, is small compared to the distance to the optical fiber. The light incident angel is therefore small. The power intercepted by the optical fiber by equation (B.4) is therefore:

$$P = I \frac{A_l}{\pi l^2} \times A_f \tag{B.7}$$

where A_f is the cross-sectional area of the optical fiber. The power density that impinges on the photodetector with area A_D is then:

$$I_{D,fiber} = I \frac{A_l}{\pi l^2} \times \frac{A_f}{A_D} \tag{B.8}$$

We notice that the power density is further reduced to A_f / A_D of direct coupling.

B.1.3 Adding a lens to regulate light path

Direct optical fiber coupling solves the problem of photodetector temperature instability. However, another problem arises from the assumption made in the beginning: the light source has to be accurately aligned to the axis of the optical fiber; otherwise the light will not be able to reach the photodetector because the incident angel exceeds the allowed range set by the numerical aperture of the optical fiber. A lens is introduced to allow for easier alignment. As illustrated in Figure B.4, the axis of the optical fiber is aligned with the optical axis of the lens, and one end of the optical fiber is fixed at the focal point of the lens. Light from the light source will always enter the optical fiber and be transported to the photodetector as along as the incident angle is within the limit set by the numerical aperture of the optical fiber. This gives:

$$\sin\alpha \approx \frac{\delta}{f} < \mathrm{NA} \tag{B.9}$$

For a lens with 30 mm focal length and an optical fiber with NA=0.22, the setup can accommodate up to 6.6 mm misalignment, which is large enough to allow easy alignment.

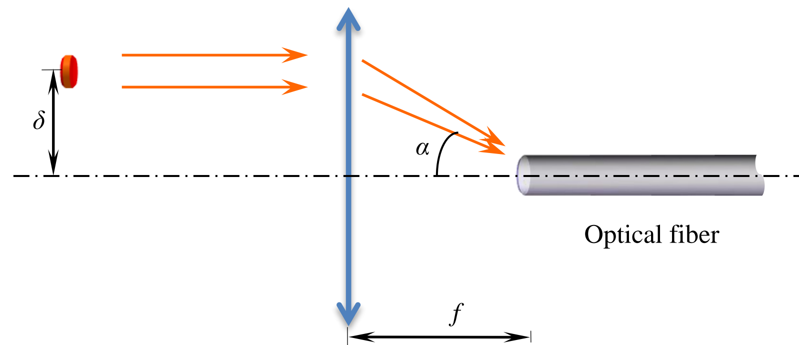

Figure B.4: Schematics of adding a lens for light coupling.

The next problem is to calculate how much energy is coupled into the optical fiber. The analysis in Figure B.5 shows that, with respect to the main axis of the lens, incident light within the angle α will reach the end of optical fiber with radius r and located at the focal point of the lens. The corresponding solid angle is $\Omega_\alpha=\pi\alpha^2$, so that the total power coupled to the optical fiber is therefore:

$$P_{lens} = A_l \times j \times \pi\alpha^2 = A_l I \left(\frac{r}{f}\right)^2 \tag{B.10}$$

And the power density impinges on the photodetector is:

$$I_{D,lens} = \frac{P_{lens}}{A_D} = \frac{A_l}{A_D} I \left(\frac{r}{f}\right)^2 \tag{B.11}$$

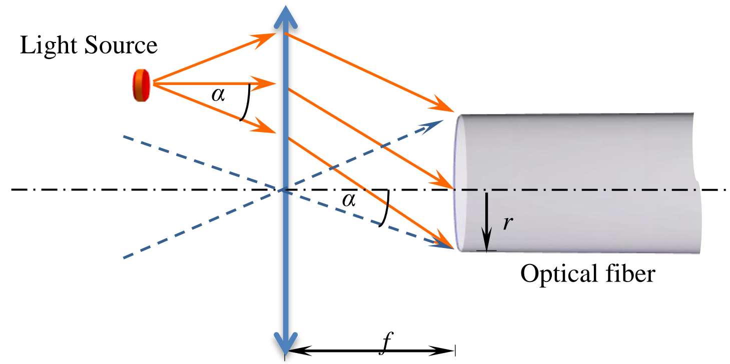

Figure B.5: Analysis on how much energy is coupled into the optical fiber. The incident light that is parallel to the auxiliary dashed line will converge and intersect with the dashed line at the focal plane.

We notice that the energy being coupled into the optical fiber is independent of the distance to the light source, and can be adjusted by using lens of different focal length or by using optical fiber of different diameter.

B.2 Photodetector and the Amplifying Circuit

The photodetector model is K1713-01 purchased from Hamamatsu Photonics. This two color detector has a silicon top layer which absorbs and detects visible light, but allows infrared light to pass through. The infrared light is then picked up by a lead sulfide (PbS) layer. The unique configuration of this two-color detector allows simultaneous detection of light intensity centered at two different wavelengths. The spectral response of the detectors can be found in Figure B.6.

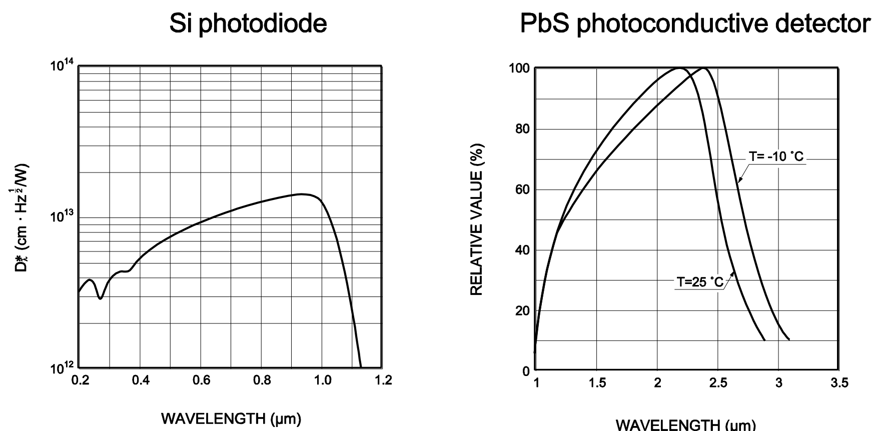

Figure B.6: Spectral response of the photodetectors (data from Hamamatsu® 1713-01 photodetector datasheet).

B.2.1 Silicon detector

The silicon detector is a p-n junction based photodetector, or a photodiode. The detector is operated at zero bias, so that it is in equilibrium with zero current output when kept in dark. Thermally excited free carriers do not contribute to electrical current. This is because (1) the detector is in equilibrium and the chemical potential is the same across the circuit so no diffusion current; and (2) there is no electrical field induced drift current due to zero bias.

When shined with photons with appropriate energy, free carriers are generated. Most of the electrons and holes soon recombine, except for those at the depletion region of the p-n junction. The electrical field at this region quickly separated electrons with holes due to they carry different signs of charges. After electrons and holes are swept away from the p-n junction region and injected into the p and n region, the excessive carrier concentration there induces diffusion current which is then collected as photocurrent. It is seen therefore the output current is in linear proportion to the radiation intensity. A circuit based on detecting photocurrent at zero bias is designed as illustrated in Figure B.7.

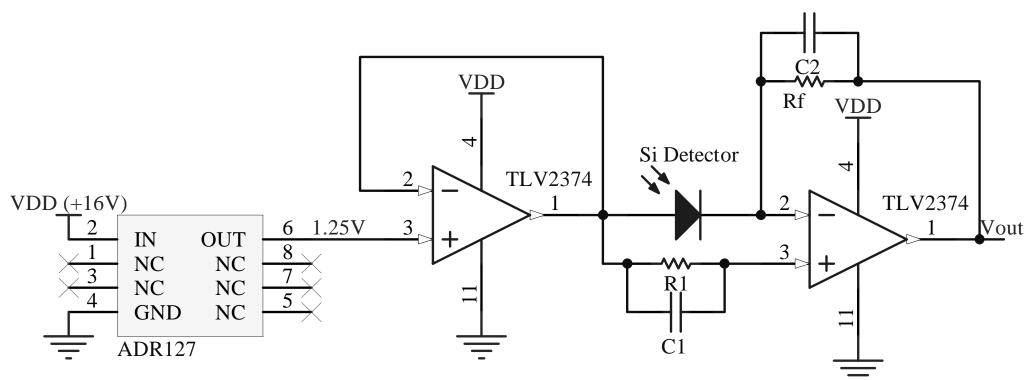

Figure B.7: Schematic circuits for silicon detector.

A reference voltage of 1.25 V is first provided by band gap reference ADR 127. It is first buffered by an operational amplifier (op-amp) working in voltage follower mode.

The second op-amp works in negative feedback mode, so its two input terminals stayed at the same electrical voltage of 1.25 V. This ensures the necessary zero-bias condition. Because of the input current of op-amp is negligible, generated photocurrent also flow through the feedback resistor R_f, which converts the photocurrent to output voltage. The final output voltage signal for silicon detector is therefore:

$$V_{Out,Si} = V_{ref} + i_{photo} R_f \tag{B.12}$$

Excessive noise signal of approximately 40 mV RMS is observed on this amplifying circuit in the initial test, which makes it useless for low-light intensity detection (the scenario would be catalyst calcination for nanotube growth at ~750˚C. At relatively low temperature the radiation intensity scales with T^4 according to Stefan-Boltzmann law and is therefore very low). The noise source is found to be related to the non-infinite resistance of print circuit board (PCB). The noise sources, such as noise from power supply and induced voltage variation by free-space electromagnetic waves, is connected by this parasitic resistor to the negative input of op-amp, which is then amplified by R_f. The effect is prominent because R_f is large (10 MΩ). The solution could be to apply a conductive shielding line to encircle the negative input pin of the op-amp, or just simply remove the negative input pin from PCB and make the electrical connection floating in air. The later method is used because it does not require a re-design and fabrication of PCB. The detector and circuit are finally encased in an aluminum box with a wall thickness of 8 mm to further reduce the disturbance from environment. The RMS of the noise output signal is reduced to approximately 100 μV after this, which means an enhancement of around 400 for signal-to-noise ratio. The noise level is now approaching the resolution limit of a 16-bit AD converter working at 0~10 V (10 V / 2^{16} = 150 μV. More details about the data acquisition system are described in Appendix C).

B.2.2 PbS detector

Different from the silicon detector, the PbS detector does not have a p-n junction, so external electrical field is required for carrier separation. The detection of light is therefore based on conductance/resistance change of the detector. As a result, thermal excited free carriers contribute significantly to the total conductance, considering the relatively small band gap 0.37 eV of lead sulfide. The dark resistance of detector is around 1 MΩ. It is found that this resistance can vary ~10% solely from laboratory temperature variation. The temperature variation of PbS detector can also come from the energy brought by the strong radiation being measured. The detector will also work in the non-linear response region under strong illumination (See Figure B.3). It is therefore preferential to restrict the detector to work within a small energy input level, which limits the photo-induced conductance to be within 10% of the original dark conductance. Obviously either the device has to be kept at constant temperature or the temperature effects have to be compensated to give dependable measurement results. Adding a temperature controller will raise the cost and complicity of the system, so temperature compensation is adopted.

The temperature compensation is carried out based on the factory given curves. There are two numbers to compensate: the dark resistance and the sensitivity of detector. The dark resistance is measured directly in dark before each experiment. Then from the dark resistance-temperature relation curve in Figure B.8(a), the temperature of detector

can be found. The temperature parameter is then used to find out the sensitivity of detector by looking at the sensitivity-temperature relation curve in Figure B.8(b).

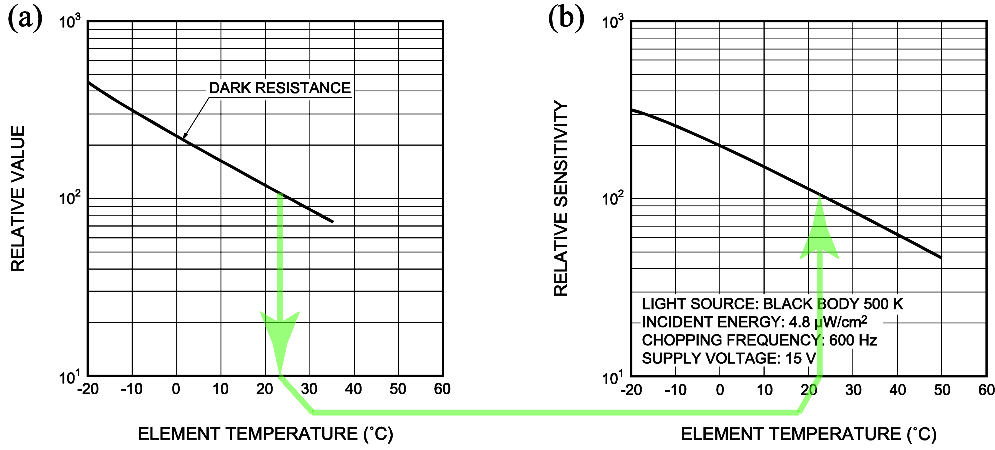

Figure B.8: Measure dark resistance to acquire the temperature of PbS detector and the corresponding sensitivity.

Specifically, the two curves in Figure B.8 are first approximated by linear relation near the working temperature of 20 ℃. The relations are:

$$\ln R_d = -k_R T + C_R \tag{B.13}$$

, and

$$\ln S = -k_S T + C_S \tag{B.14}$$

where R_d is dark resistance and S is sensitivity. Sensitivity represents the ratio of actual light intensity to measured electrical signal. k_R, C_R, k_S and C_S are the constants. k_S and k_R are determined to be 0.02926 and 0.03185 respectively by curve fitting (Figure B.8). After some manipulation with the previous two equations, we get:

$$S = S_0 \left(R_d / R_{d0} \right)^{\frac{k_S}{k_R}} = S_0 \left(R_d / R_{d0} \right)^{0.919} \tag{B.15}$$

where S_0 and R_{d0} is sensitivity and dark resistance respectively at reference temperature T_0.

The detector is working in constant bias mode. The voltage applied on the detector is 17.25V according to the amplifying circuit configuration as illustrated in Figure B.9. The corresponding electrical field can quickly separate the free carriers generated by illumination and produce photocurrent. The photocurrent is then converted to voltage signal by feedback resistor R_f. The circuit output is:

$$V_{out,PbS} = V_{ref} + i \cdot R_f = V_{ref} + \left(\frac{V_{ref} - V_{SS}}{R_{dark}} + i_{photo} \right) R_f \tag{B.16}$$

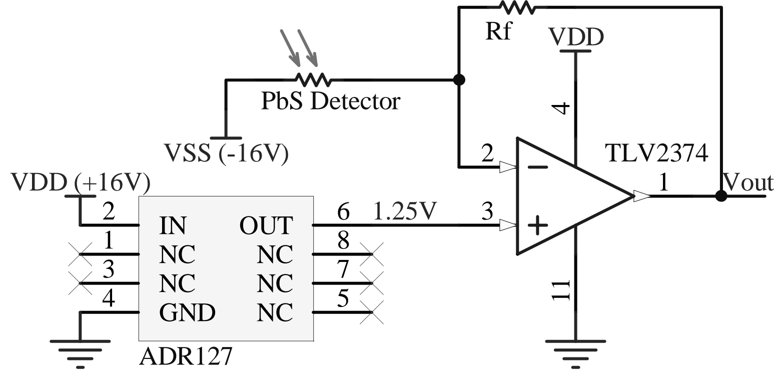

Figure B.9: Amplifying circuits for PbS detector.

To compensate the temperature effects, dark current is first measured by completely shielding the detector from any light source immediately before experiments, so that:

$$i_{dark} = (V_{out,PbS} - V_{ref}) / R_f \tag{B.17}$$

Since $i_{dark} = (V_{ref} - V_{ss})/R_d$ is proportional to R_d^{-1}, we get from (B.15) that

$$S = S_0 \left(i_0 / i_{dark} \right)^{0.919} \tag{B.18}$$

where i_0 is reference current.

During a growth experiment, electrical current is applied to heat up the suspended micro heater to growth temperature. The thermal radiation induces photo current, which is deduced from (B.16) to be:

$$i_{photo} = (V_{out} - V_{ref}) / R_f - i_{dark} \tag{B.19}$$

And the radiation power to be measured is therefore:

$$I_{PbS} = S \times i_{photo} = S_0 \left(\frac{i_0}{i_{dark}} \right)^{0.919} \left(\frac{V_{out} - V_{ref}}{R_f} - i_{dark} \right) \tag{B.20}$$

B.3 System Calibration

The system calibration is done using a conventional furnace. Absolute light intensity calibration is not carried out because the system is used solely for the purpose of temperature measurement. The signal strength ratios of Si detector to PbS detector are recorded at different temperatures targeting at a silicon wafer surface placed inside a furnace, as illustrated in Figure B.10. The silicon wafer used here is the same as µCVD chip material, (boron heavily doped silicon covered by 200 nm oxide) so it should exhibit identical radiation spectrum. The pinhole and fiber collimator limits the incoming light to only source from the silicon wafer.

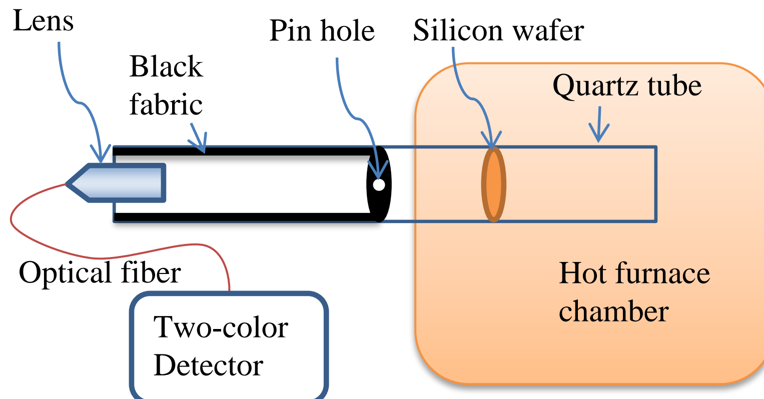

Figure B.10: Setup for optical temperature measuring system calibration.

The calibrated results are listed in Table B.1. The measurements are repeated twice with good repeatability. The wavelengths used here are chosen to be within the most sensitive region of silicon and lead sulfide detector (See Figure B.6).

Table B.1: Calibrated Si / PbS detector signal ratio (R_{vi}) v.s. temperature.

Temperature (℃)	700	750	800	850	900	950	1000	1050
R_{vi} (Si / PbS signal ratio)	1.25	1.7	2.3	3.0	3.8	4.7	5.8	7.1

Appendix C Signal Processing and Computer Control

C.1 General Description of the Construction

The heating and temperature control is interfaced with computer via USB (universal serial bus) data interface. The data is communicated with an AD/DA (analog to digital / digital to analog conversion) module. The AD converter converts the analog signal of electrical voltages from the optical detector and from the current and voltage monitor to digital signal. The DA converter converts the digital signal of the heating voltage for the microheater to analog voltage signal. The analog signal to and from the microheater is transported through another module into the µCVD chamber. This module composes mainly of amplifiers. Power amplifiers provide enough power (up to ~10 W) for heating; operational amplifiers and instrumental amplifiers perform signal acquiring and conditioning. The nanopositioner comes with a commercially available controller, which is connected to the computer via a separate USB cable.

C.2 AD/DA Module

The AD/DA module is purchased from National Instruments (NI USB-6221). It has 16 analog inputs (16-bit, 250 kS/s, -10V~10V) and 2 analog outputs (16-bit, 833 kS/s).

The signal from the photo detectors are amplified and connected to the analog inputs of the AD/DA module. Two other signals, representing the voltage and current applied to the microheater respectively, are also connected to the analog inputs. Notice that AD/DA module has only one actual AD converter built in. The connections between the 16 analog input channels and the AD converter are established and cut off by an analog switch consecutively. It is therefore important to open only the input ports to be used. Also, the waiting time before switching to a different channel should be long enough to make sure the signal connected to the AD converter is stabilized. This is especially true for signal source of relatively large output impedance since the stabilization time is proportional to the RC time constant. The voltage to be applied onto the microheater is controlled by the analog output on the AD/DA module.

The AD/DA module is connected with a computer by a USB cable. The control over the AD/DA module is through Matlab® Data Acquisition Toolbox. It is found that the sampling rate on the AD/DA module has to be set much higher than the actual readout frequency on the computer; otherwise the readout will either be empty or a set of several samples. This is probably due to the limitation of the USB protocol.

C.3 Signal Amplification and Conditioning Module

The output signal from the AD/DA module cannot be connected directly to the microheaters, as several watts are required to bring the microheaters to their operating temperature of approximately 1000 ℃ and the output power of the AD/DA module cannot exceed 50 mW. Four power amplifiers are therefore utilized to provide enough power to heat up the μCVD unit.

The circuit for this module can be found in Figure C.1. The input signal is first Two power amplifiers are connected in parallel to provide voltage in the plus range of 0~16V, while the other two amplifiers provide voltage in the negative range. The maximum voltage can be applied on the μCVD unit is therefore 32V. Diodes are necessary as they block the current flow between the two parallel connected power amplifiers. Without them, the amplifiers become unstable.

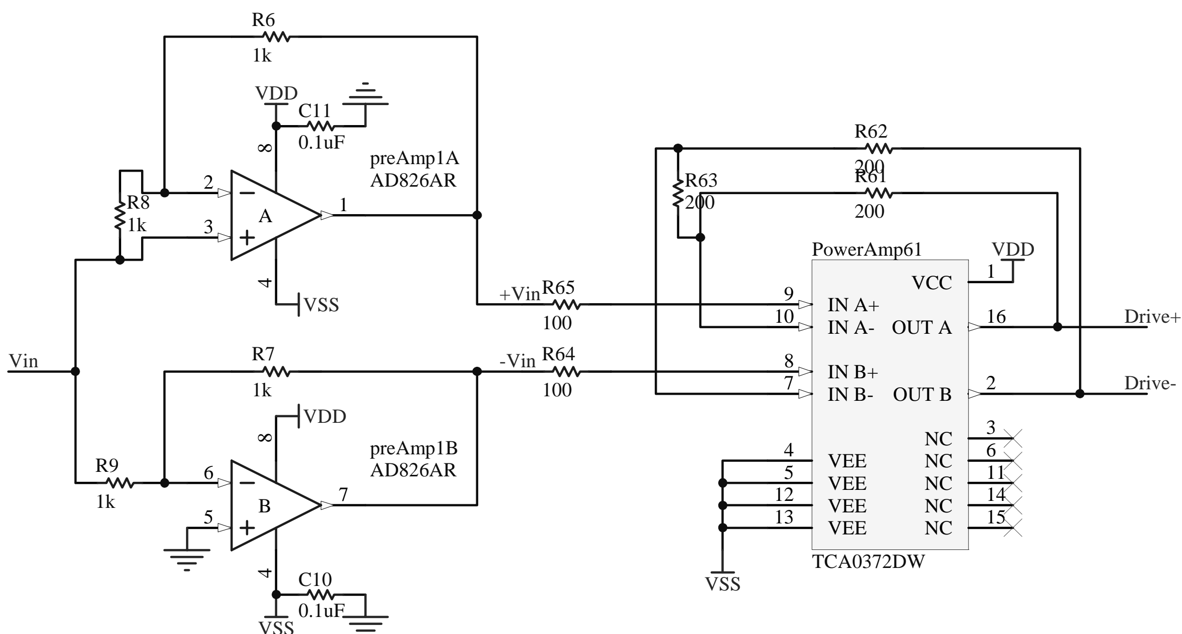

Figure C.1: The schematic circuits for signal amplification and conditioning.

C.4 Temperature Control Program

The schematic of the temperature control program is shown in Figure C.2. The measured data of the µCVD system, such as temperature (the temperature information is actually acquired from the signals produced by PbS and silicon photodetector), voltage and current, is collected from the AD/DA module. The sampling rate of the AD/DA module is set at 960 Hz, but the data is only collected 5 times per second. As a result, roughly 200 data sets are acquired each time. An analysis on the signal noise reveals that the spectrum of the noise is white, with the exception of the silicon photodetector channel which has a distinctive 60 Hz noise and its harmonics. A digital FIR (finite impulse response) filter is designed to filter the noise. The 160-order equiripple filter is directly designed using Matlab® Signal Processing Toolbox. The order is chosen to be 160 because of the USB data transfer instability (See Section C.2).

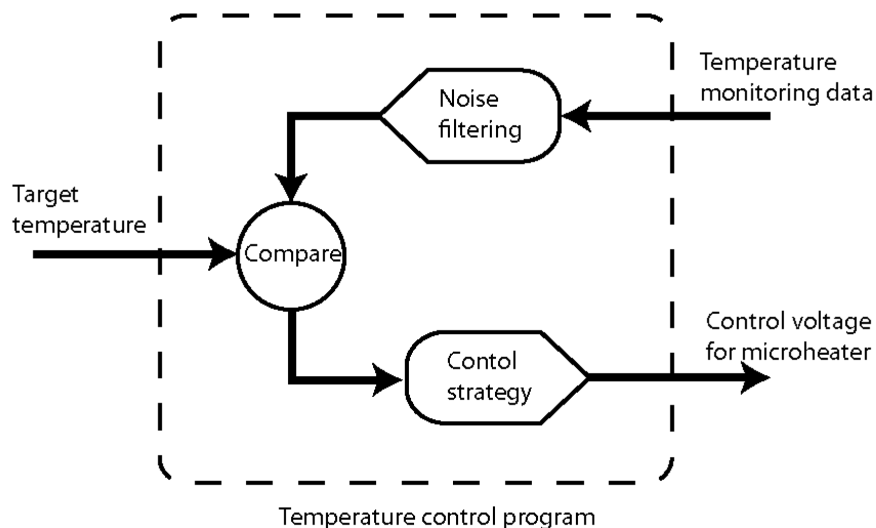

Figure C.2: Schematic of the temperature control program.

The data is then compared with the target temperature so that the control voltage for the microheater can be determined. The control strategy is:

1. When the signal from the photodetector is too low, raise the voltage to be applied on the microheater at the rate of 0.2 volt per controlling cycle.

2. When the signal from the photodetector is strong and reliable, determine which region on the I-V curve the microheater is working in based on the current and historical voltage and current data (See Section 2.4.2, Figure 2.23). This is because the silicon heater behaves very differently in different regions. For region II, increasing voltage will not significantly increase the current and the temperature. For region III, increasing a very small amount of voltage can significantly increase the current and temperature.

3. For different working region, use different parameters for PID (proportional–integral–derivative) control. The parameters are decided from several experimental runs. Because the control time interval is much longer than the thermal time constant of the microheater, the derivative “D” term is set to a very small value.

For the ease of operating the μCVD system, the program is designed with a user interface (Figure C.3). The monitored data is also displayed and stored in real time. The voltage and current applied are also displayed graphically so that the user of the program has a better perception of the working status of the microheater. Finally, the operation guidance for a chosen growth recipe is also displayed step by step to minimize possible operation errors by the user.

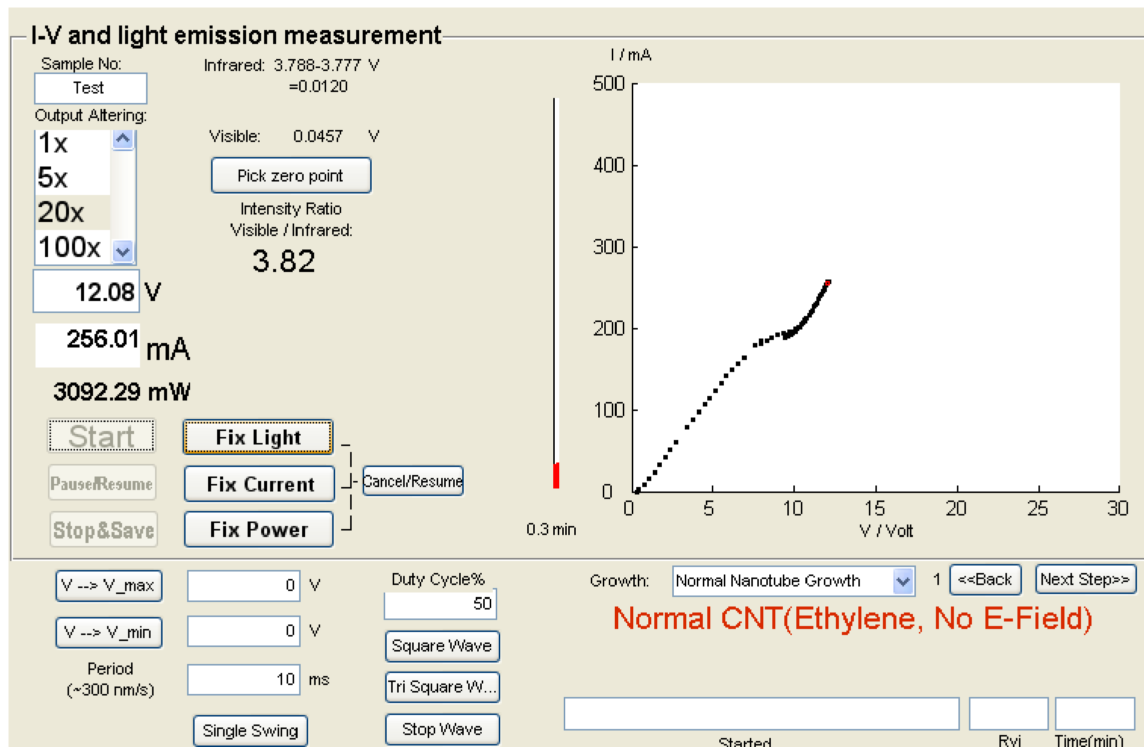

Figure C.3: Control program user interface

C.5 Nanopositioner and Its Control Program

The nanopositioner is a 2-axis linear piezoelectric step motor driven stage (Mechonics® MS 15). It has a minimum step size of roughly 15 nm. The size of the nanopositioner is only 15 mm $\times$ 15 mm $\times$ 12.5 mm, but with 3.5 mm travel range.

The nanopositioner control program is written to direct the movement of the stage to follow a certain path. The program is written in Microsoft® Visual C++. The brief flow chart is illustrated in Figure C.4. After installing the driver, ftd2xx.dll can be loaded explicitly, and commands can be sent through it. The chipset FT232R translate the data from USB to standard serial port RS232 signal. The signal is then sent to a microcontroller for generating control voltage for the nanopositioner.

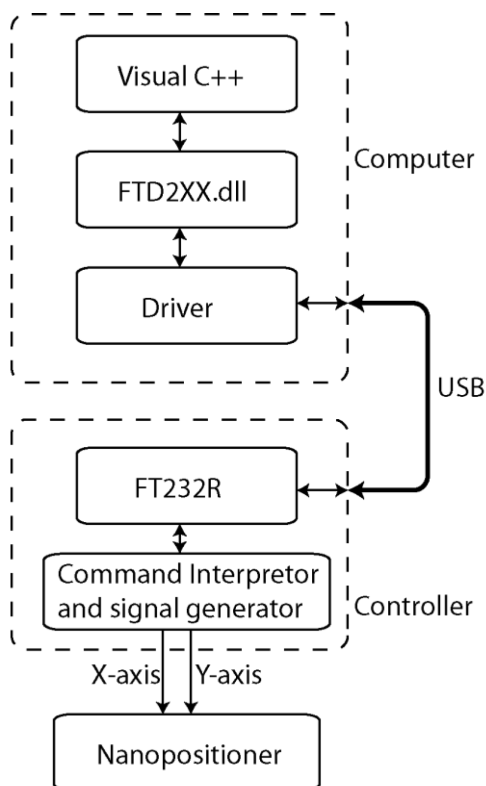

Figure C.4: Nanopositioner control program flow chart.

A user interface is designed to facilitate the control (Figure C.5). The running path is read from a text file with the coordinates of the points on the path.

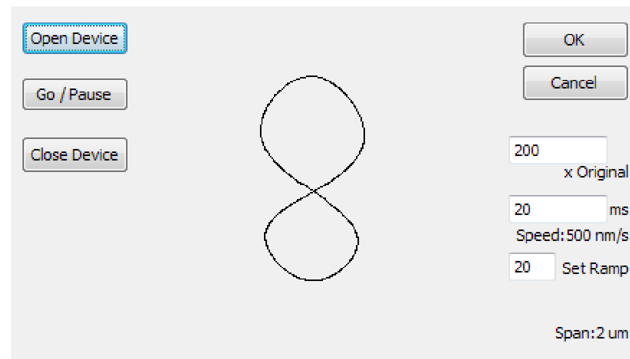

Figure C.5: The user interface for nanopositioner control program.

Bibliography

[1] O. M. Koo, *et al.*, "Role of nanotechnology in targeted drug delivery and imaging: a concise review," *Nanomedicine,* vol. 1, pp. 193-212, Sep 2005.

[2] K. A. Dick, "A review of nanowire growth promoted by alloys and non-alloying elements with emphasis on Au-assisted III-V nanowires," *Progress in Crystal Growth and Characterization of Materials,* vol. 54, pp. 138-173, 2008.

[3] A. K. Wanekaya, *et al.*, "Nanowire based electrochemical biosensors," *Electroanalysis,* vol. 18, pp. 533-550, 2006.

[4] Y. Li, *et al.*, "Nanowire electronic and optoelectronic devices," *Materials Today,* vol. 9, pp. 18-27, 2006.

[5] C. Thelander, *et al.*, "Nanowire-based one-dimensional electronics," *Materials Today,* vol. 9, pp. 28-35, 2006.

[6] R. Hardman, "A toxicologic review of quantum dots: toxicity depends on physicochemical and environmental factors," *Environmental health perspectives,* vol. 114, p. 165, 2006.

[7] D. Loss and D. P. DiVincenzo, "Quantum computation with quantum dots," *Physical Review A,* vol. 57, p. 120, 1998.

[8] A. P. Alivisatos, *et al.*, "Quantum dots as cellular probes," *Annu. Rev. Biomed. Eng.,* vol. 7, pp. 55-76, 2005.

[9] A. Leo. (2002). *The State of Nanotechnology*. Available: http://www.technologyreview.com/computing/12862/

[10] J. Tersoff, *et al.*, "Self-organization in growth of quantum dot superlattices," *Physical Review Letters,* vol. 76, pp. 1675-1678, 1996.

[11] M. Grundmann, *et al.*, "InAs/GaAs pyramidal quantum dots: Strain distribution, optical phonons, and electronic structure," *Physical Review B,* vol. 52, p. 11969, 1995.

[12] M. Reed, *et al.*, "Observation of discrete electronic states in a zero-dimensional semiconductor nanostructure," *Physical Review Letters,* vol. 60, pp. 535-537, 1988.

[13] J. Wang, "Carbon-nanotube based electrochemical biosensors: a review," *Electroanalysis,* vol. 17, pp. 7-14, 2005.

[14] J. N. Coleman, *et al.*, "Small but strong: A review of the mechanical properties of carbon nanotube-polymer composites," *Carbon,* vol. 44, pp. 1624-1652, 2006.

[15] C. Lam, *et al.*, "A review of carbon nanotube toxicity and assessment of potential occupational and environmental health risks," *CRC Critical Reviews in Toxicology,* vol. 36, pp. 189-217, 2006.

[16] J. P. Salvetat, *et al.*, "Elastic and shear moduli of single-walled carbon nanotube ropes," *Physical Review Letters,* vol. 82, pp. 944-947, 1999.

[17] L. Langer, *et al.*, "Quantum transport in a multiwalled carbon nanotube," *Physical Review Letters,* vol. 76, pp. 479-482, 1996.

[18] K. S. Novoselov, *et al.*, "Electric field effect in atomically thin carbon films," *Science,* vol. 306, pp. 666-9, Oct 22 2004.

[19] K. S. Novoselov, *et al.*, "Two-dimensional gas of massless Dirac fermions in graphene," *Nature,* vol. 438, pp. 197-200, Nov 10 2005.

[20] A. K. Geim and K. S. Novoselov, "The rise of graphene," *Nature Materials,* vol. 6, pp. 183-191, Mar 2007.

[21] K. S. Novoselov, *et al.*, "Two-dimensional atomic crystals," *Proceedings of the National Academy of Sciences of the United States of America,* vol. 102, pp. 10451-10453, Jul 26 2005.

[22] A. K. Geim, "Graphene: status and prospects," *Science,* vol. 324, pp. 1530-4, Jun 19 2009.

[23] R. Martel, *et al.*, "Single-and multi-wall carbon nanotube field-effect transistors," *Applied Physics Letters,* vol. 73, p. 2447, 1998.

[24] M. Menon and D. Srivastava, "Carbon nanotube “T junctions”: nanoscale metal-semiconductor-metal contact devices," *Physical Review Letters,* vol. 79, pp. 4453-4456, 1997.

[25] V. Derycke, *et al.*, "Carbon nanotube inter-and intramolecular logic gates," *Nano Letters,* vol. 1, pp. 453-456, 2001.

[26] R. Saito, *et al.*, *Physical properties of carbon nanotubes* vol. 3: Imperial College Press London, 1998.

[27] A. Berezhkovskii and G. Hummer, "Single-file transport of water molecules through a carbon nanotube," *Physical Review Letters,* vol. 89, p. 64503, 2002.

[28] L. Chico, *et al.*, "Pure carbon nanoscale devices: nanotube heterojunctions," *Physical Review Letters,* vol. 76, pp. 971-974, 1996.

[29] M. Fujii, *et al.*, "Measuring the thermal conductivity of a single carbon nanotube," *Physical Review Letters,* vol. 95, p. 65502, 2005.

[30] A. Javey, *et al.*, "Ballistic carbon nanotube field-effect transistors," *Nature,* vol. 424, pp. 654-657, Aug 7 2003.

[31] S. J. Tans, *et al.*, "Room-temperature transistor based on a single carbon nanotube," *Nature,* vol. 393, pp. 49-52, 1998.

[32] A. Bachtold, *et al.*, "Logic circuits with carbon nanotube transistors," *Science,* vol. 294, p. 1317, 2001.

[33] A. Javey, *et al.*, "Carbon nanotube transistor arrays for multistage complementary logic and ring oscillators," *Nano Letters,* vol. 2, pp. 929-932, 2002.

[34] S. Li, *et al.*, "Carbon nanotube transistor operation at 2.6 GHz," *Nano Letters,* vol. 4, pp. 753-756, 2004.

[35] P. Qi, *et al.*, "Toward large arrays of multiplex functionalized carbon nanotube sensors for highly sensitive and selective molecular detection," *Nano Letters,* vol. 3, pp. 347-351, 2003.

[36] J. Li, *et al.*, "Carbon nanotube sensors for gas and organic vapor detection," *Nano Letters,* vol. 3, pp. 929-933, 2003.

[37] S. Chopra, *et al.*, "Selective gas detection using a carbon nanotube sensor," *Applied Physics Letters,* vol. 83, p. 2280, 2003.

[38] W. Choi, *et al.*, "Fully sealed, high-brightness carbon-nanotube field-emission display," *Applied Physics Letters,* vol. 75, p. 3129, 1999.

[39] Q. Wang, *et al.*, "A nanotube-based field-emission flat panel display," *Applied Physics Letters,* vol. 72, p. 2912, 1998.

[40] Q. Wang, *et al.*, "Flat panel display prototype using gated carbon nanotube field emitters," *Applied Physics Letters,* vol. 78, p. 1294, 2001.

[41] A. Bianco, *et al.*, "Applications of carbon nanotubes in drug delivery," *Current Opinion in Chemical Biology,* vol. 9, pp. 674-679, 2005.

[42] N. W. S. Kam, *et al.*, "Nanotube molecular transporters: internalization of carbon nanotube-protein conjugates into mammalian cells," *Journal of the American Chemical Society,* vol. 126, pp. 6850-6851, 2004.

[43] A. A. Bhirde, *et al.*, "Targeted killing of cancer cells in vivo and in vitro with EGF-directed carbon nanotube-based drug delivery," *ACS Nano,* vol. 3, pp. 307-316, 2009.

[44] Z. Liu, *et al.*, "Drug delivery with carbon nanotubes for in vivo cancer treatment," *Cancer research,* vol. 68, p. 6652, 2008.

[45] Y. Zhang, *et al.*, "Experimental observation of the quantum Hall effect and Berry's phase in graphene," *Nature,* vol. 438, pp. 201-4, Nov 10 2005.

[46] K. S. Novoselov, *et al.*, "Room-temperature quantum Hall effect in graphene," *Science,* vol. 315, p. 1379, 2007.

[47] Y. M. Lin*, et al.*, "Operation of graphene transistors at gigahertz frequencies," *Nano Letters,* vol. 9, pp. 422-426, 2008.

[48] T. Mueller*, et al.*, "Graphene photodetectors for high-speed optical communications," *Arxiv preprint arXiv:1009.4465,* 2010.

[49] F. Schedin*, et al.*, "Detection of individual gas molecules adsorbed on graphene," *Nature Materials,* vol. 6, pp. 652-655, Sep 2007.

[50] X. Wang*, et al.*, "Transparent, conductive graphene electrodes for dye-sensitized solar cells," *Nano Letters,* vol. 8, pp. 323-327, 2008.

[51] B. Dabbousi*, et al.*, "(CdSe) ZnS core-shell quantum dots: synthesis and characterization of a size series of highly luminescent nanocrystallites," *The Journal of Physical Chemistry B,* vol. 101, pp. 9463-9475, 1997.

[52] L. E. Greene*, et al.*, "Solution-grown zinc oxide nanowires," *Inorganic chemistry,* vol. 45, pp. 7535-7543, 2006.

[53] A. M. Morales and C. M. Lieber, "A laser ablation method for the synthesis of crystalline semiconductor nanowires," *Science,* vol. 279, p. 208, 1998.

[54] S. Park and R. S. Ruoff, "Chemical methods for the production of graphenes," *Nature Nanotechnology,* vol. 4, pp. 217-224, 2009.

[55] S. H. Dalal*, et al.*, "Controllable growth of vertically aligned zinc oxide nanowires using vapour deposition," *Nanotechnology,* vol. 17, pp. 4811-4818, Oct 14 2006.

[56] J. Kong*, et al.*, "Chemical vapor deposition of methane for single-walled carbon nanotubes," *Chemical Physics Letters,* vol. 292, pp. 567-574, Aug 14 1998.

[57] J.-H. Park and T. S. Sudarshan, *Chemical vapor deposition*. Materials Park, OH: ASM International, 2001.

[58] C. H. See and A. T. Harris, "A review of carbon nanotube synthesis via fluidized-bed chemical vapor deposition," *Industrial & engineering chemistry research,* vol. 46, pp. 997-1012, 2007.

[59] H. O. Pierson, *Handbook of chemical vapor deposition*, 2nd ed. Norwich, NY: Noyes Publications, 1999.

[60] H. O. Pierson, *Handbook of chemical vapor deposition (CVD) : principles, technology, and applications*. Park Ridge, N.J., U.S.A.: Noyes Publications, 1992.

[61] R. S. Wagner and W. C. Ellis, "Vapor-Liquid-Solid Mechanism of Single Crystal Growth (New Method Growth Catalysis from Impurity Whisker Epitaxial + Large Crystals Si E)," *Applied Physics Letters,* vol. 4, pp. 89-&, 1964.

[62] The research on TEM started in the 1930s. The TEM was further developed at Siemens and was commericalized in 1939.

[63] H. J. Dai, "Carbon nanotubes: opportunities and challenges," *Surface Science,* vol. 500, pp. 218-241, Mar 10 2002.

[64] L. Alvarez*, et al.*, "Growth mechanisms and diameter evolution of single wall carbon nanotubes," *Chemical Physics Letters,* vol. 342, pp. 7-14, Jul 6 2001.

[65] H. C. Choi, *et al.*, "Efficient formation of iron nanoparticle catalysts on silicon oxide by hydroxylamine for carbon nanotube synthesis and electronics," *Nano Letters,* vol. 3, pp. 157-161, Feb 2003.

[66] L. Ding, *et al.*, "Growth of high-density parallel arrays of long single-walled carbon nanotubes on quartz substrates," *Journal of the American Chemical Society,* vol. 130, pp. 5428-5432, Apr 23 2008.

[67] J. Zhang, *et al.*, ""Cloning" of Single-Walled Carbon Nanotubes via Open-End Growth Mechanism," *Nano Letters,* vol. 9, pp. 1673-1677, Apr 2009.

[68] S. Jin, *et al.*, "Mechanism and Kinetics of Spontaneous Nanotube Growth Driven by Screw Dislocations," *Science,* vol. 328, pp. 476-480, Apr 23 2010.

[69] R. P. Manginell, *et al.*, "In-Situ Monitoring of Micro-Chemical Vapor Deposition : Experimental Results and Spice Modeling," in *Technical Digest of Solid-State Sensor and Actuator Workshop*, Hilton Head Island, South Carolina, 1998, pp. 371-374.

[70] R. P. Manginell, *et al.*, "Selective, Pulsed CVD of Platinum on Microfilament Gas Sensors," in *Technical Digest of Solid-State Sensor and Actuator Workshop*, Hilton Head Island, South Carolina, 1996, pp. 23-27.

[71] T. Kawano, *et al.*, "An electrothermal carbon nanotube gas sensor," *Nano Letters,* vol. 7, pp. 3686-3690, Dec 2007.

[72] O. Englander, *et al.*, "Local synthesis of silicon nanowires and carbon nanotubes on microbridges," *Applied Physics Letters,* vol. 82, pp. 4797-4799, Jun 30 2003.

[73] O. Englander, *et al.*, "Electric-field assisted growth and self-assembly of intrinsic silicon nanowires," *Nano Letters,* vol. 5, pp. 705-708, Apr 2005.

[74] S. W. Lee, *et al.*, "Layer-by-Layer Assembly of All Carbon Nanotube Ultrathin Films for Electrochemical Applications," *Journal of the American Chemical Society,* vol. 131, pp. 671-679, Jan 21 2009.

[75] J. Liu, *et al.*, "Fullerene pipes," *Science,* vol. 280, pp. 1253-1256, May 22 1998.

[76] B. Long, *et al.*, "Ultra-fast and scalable sidewall functionalisation of single-walled carbon nanotubes with carboxylic acid," *Chemical Communications,* pp. 2788-2790, 2008.

[77] S. M. Huang, *et al.*, "Ultralong, well-aligned single-walled carbon nanotube architectures on surfaces," *Advanced Materials,* vol. 15, pp. 1651-1655, Oct 2 2003.

[78] J. P. Holman, *Heat transfer*, 9th ed. New York: McGraw-Hill, 2002.

[79] B. H. Hong, *et al.*, "Quasi-continuous growth of ultralong carbon nanotube arrays," *Journal of the American Chemical Society,* vol. 127, pp. 15336-15337, Nov 9 2005.

[80] G. Zhang, *et al.*, "Ultra-high-yield growth of vertical single-walled carbon nanotubes: Hidden roles of hydrogen and oxygen," *Proc Natl Acad Sci U S A,* vol. 102, pp. 16141-5, Nov 8 2005.

[81] F. P. Incropera, *Fundamentals of heat and mass transfer*, 6th ed. Hoboken, NJ: John Wiley, 2007.

[82] N. J. Nielsen, "History of Thinkjet Printhead Development," *Hewlett-Packard Journal,* vol. 36, pp. 4-10, 1985.

[83] M. A. Northrup*, et al.*, "DNA amplification with a microfabricated reaction chamber," *Proc. 1997 International Conference on Solid-State Sensors and Actuators,* pp. 81-88, 1993.

[84] B. W. Chui*, et al.*, "Low-stiffness silicon cantilevers for thermal writing and piezoresistive readback with the atomic force microscope," *Applied Physics Letters,* vol. 69, pp. 2767-2769, Oct 28 1996.

[85] J. H. Daniel*, et al.*, "Silicon microchambers for DNA amplification," *Sensors and Actuators A-Physical,* vol. 71, pp. 81-88, Nov 1 1998.

[86] M. U. Kopp*, et al.*, "Chemical amplification: Continuous-flow PCR on a chip," *Science,* vol. 280, pp. 1046-1048, May 15 1998.

[87] P. W. Atkins, *Physical chemistry*, 5th ed. New York: W.H. Freeman, 1994.

[88] Z. Yao*, et al.*, "High-field electrical transport in single-wall carbon nanotubes," *Physical Review Letters,* vol. 84, pp. 2941-2944, Mar 27 2000.

[89] Q. Zhou and L. Lin, "Enhancing Mass Transport for Synthesizing Single-Walled Carbon Nanotubes via Micro Chemical Vapor Deposition," *Journal of MicroElectroMechanical Systems,* vol. 20, pp. 9-11, February 2011.

[90] J. Bustillo and M. Wasilik. *Microlab equipment manual for STS*. Available: http://nanolab.berkeley.edu/labmanual/chap7/7.21sts.pdf

[91] C. Kittel, *Introduction to solid state physics*, 6th ed. New York: Wiley, 1986.

[92] C. Kittel and H. Kroemer, *Thermal physics*, 2d ed. San Francisco: W. H. Freeman, 1980.

[93] J. Kong*, et al.*, "Synthesis of individual single-walled carbon nanotubes on patterned silicon wafers," *Nature,* vol. 395, pp. 878-881, Oct 29 1998.

[94] K. Hata*, et al.*, "Water-assisted highly efficient synthesis of impurity-free single-waited carbon nanotubes," *Science,* vol. 306, pp. 1362-1364, Nov 19 2004.

[95] N. R. Franklin*, et al.*, "Patterned growth of single-walled carbon nanotubes on full 4-inch wafers," *Applied Physics Letters,* vol. 79, pp. 4571-4573, Dec 31 2001.

[96] D. N. Futaba*, et al.*, "Kinetics of water-assisted single-walled carbon nanotube synthesis revealed by a time-evolution analysis," *Physical Review Letters,* vol. 95, pp. -, Jul 29 2005.

[97] A. R. Harutyunyan*, et al.*, "Hidden features of the catalyst nanoparticles favorable for single-walled carbon nanotube growth," *Applied Physics Letters,* vol. 90, p. 163120, Apr 16 2007.

[98] S. Helveg*, et al.*, "Atomic-scale imaging of carbon nanofibre growth," *Nature,* vol. 427, pp. 426-429, Jan 29 2004.

[99] J. C. Charlier and S. Iijima, "Growth mechanisms of carbon nanotubes," *Carbon Nanotubes,* vol. 80, pp. 55-80, 2001.

[100] H. T. Liu*, et al.*, "Translocation of Single-Stranded DNA Through Single-Walled Carbon Nanotubes," *Science,* vol. 327, pp. 64-67, Jan 1 2010.

[101] Y. L. Li*, et al.*, "Direct spinning of carbon nanotube fibers from chemical vapor deposition synthesis," *Science,* vol. 304, pp. 276-278, Apr 9 2004.

[102] Q. Zhou and L. Lin, "Micro Chemical Vapor Deposition System: Design And Verification," in *22nd IEEE Intl. Conf. on Micro-Electro-Mechanical Systems*, Italy, 2009, pp. 587-90.

[103] L. W. Lin and M. Chiao, "Electrothermal responses of lineshape microstructures," *Sensors and Actuators a-Physical,* vol. 55, pp. 35-41, Jul 15 1996.

[104] S. Li*, et al.*, "Single quantum dots as local temperature markers," *Nano Letters,* vol. 7, pp. 3102-3105, Oct 2007.

[105] Y. Homma*, et al.*, "Mechanism of bright selective imaging of single-walled carbon nanotubes on insulators by scanning electron microscopy," *Applied Physics Letters,* vol. 84, pp. 1750-1752, Mar 8 2004.

[106] B. Zheng*, et al.*, "Efficient CVD growth of single-walled carbon nanotubes on surfaces using carbon monoxide precursor," *Nano Letters,* vol. 2, pp. 895-898, Aug 2002.

[107] N. R. Franklin and H. J. Dai, "An enhanced CVD approach to extensive nanotube networks with directionality," *Advanced Materials,* vol. 12, pp. 890-894, Jun 16 2000.

[108] K. Takei*, et al.*, "Nanowire active-matrix circuitry for low-voltage macroscale artificial skin," *Nature Materials,* vol. 9, pp. 821-826, Oct 2010.

[109] J. Zhou*, et al.*, "Flexible piezotronic strain sensor," *Nano Letters,* vol. 8, pp. 3035-3040, Sep 2008.

[110] B. J. Kim*, et al.*, "High-Performance Flexible Graphene Field Effect Transistors with Ion Gel Gate Dielectrics," *Nano Letters,* vol. 10, pp. 3464-3466, Sep 2010.

[111] M. C. McAlpine*, et al.*, "High-performance nanowire electronics and photonics on glass and plastic substrates," *Nano Letters,* vol. 3, pp. 1531-1535, Nov 2003.

[112] D.-m. Sun*, et al.*, "Flexible high-performance carbon nanotube integrated circuits," *Nature Nanotechnology,* vol. 6, pp. 156-161, 2011.

[113] T. Durkop*, et al.*, "Extraordinary mobility in semiconducting carbon nanotubes," *Nano Letters,* vol. 4, pp. 35-39, Jan 2004.

[114] M. Radosavljevic*, et al.*, "High-field electrical transport and breakdown in bundles of single-wall carbon nanotubes," *Physical Review B,* vol. 64, p. 241307, Dec 15 2001.

[115] Z. Y. Zhang*, et al.*, "Self-Aligned Ballistic n-Type Single-Walled Carbon Nanotube Field-Effect Transistors with Adjustable Threshold Voltage," *Nano Letters,* vol. 8, pp. 3696-3701, Nov 2008.

[116] K. Bradley, *et al.*, "Flexible nanotube electronics," *Nano Letters,* vol. 3, pp. 1353-1355, Oct 2003.

[117] S. J. Kang, *et al.*, "High-performance electronics using dense, perfectly aligned arrays of single-walled carbon nanotubes," *Nature Nanotechnology,* vol. 2, pp. 230-236, Apr 2007.

[118] F. N. Ishikawa, *et al.*, "Transparent Electronics Based on Transfer Printed Aligned Carbon Nanotubes on Rigid and Flexible Substrates," *ACS Nano,* vol. 3, pp. 73-79, Jan 2009.

[119] M. J. Ha, *et al.*, "Printed, Sub-3V Digital Circuits on Plastic from Aqueous Carbon Nanotube Inks," *ACS Nano,* vol. 4, pp. 4388-4395, Aug 2010.

[120] M. Burghard, *et al.*, "Controlled adsorption of carbon nanotubes on chemically modified electrode arrays," *Advanced Materials,* vol. 10, pp. 584-588, Jun 2 1998.

[121] J. C. Lewenstein, *et al.*, "High-yield selective placement of carbon nanotubes on pre-patterned electrodes," *Nano Letters,* vol. 2, pp. 443-446, May 2002.

[122] S. G. Rao, *et al.*, "Nanotube electronics: large-scale assembly of carbon nanotubes," *Nature,* vol. 425, pp. 36-7, Sep 4 2003.

[123] M. D. Lay, *et al.*, "Simple route to large-scale ordered arrays of liquid-deposited carbon nanotubes," *Nano Letters,* vol. 4, pp. 603-606, Apr 2004.

[124] M. A. Meitl, *et al.*, "Solution casting and transfer printing single-walled carbon nanotube films," *Nano Letters,* vol. 4, pp. 1643-1647, Sep 2004.

[125] K. L. Lu, *et al.*, "Mechanical damage of carbon nanotubes by ultrasound," *Carbon,* vol. 34, pp. 814-816, 1996.

[126] S. Niyogi, *et al.*, "Ultrasonic dispersions of single-walled carbon nanotubes," *Journal of Physical Chemistry B,* vol. 107, pp. 8799-8804, Aug 28 2003.

[127] J. Chen, *et al.*, "Solution properties of single-walled carbon nanotubes," *Science,* vol. 282, pp. 95-98, Oct 2 1998.

[128] A. Ural, *et al.*, "Electric-field-aligned growth of single-walled carbon nanotubes on surfaces," *Applied Physics Letters,* vol. 81, pp. 3464-3466, Oct 28 2002.

[129] Z. Jin, *et al.*, "Ultralow feeding gas flow guiding growth of large-scale horizontally aligned single-walled carbon nanotube arrays," *Nano Letters,* vol. 7, pp. 2073-2079, Jul 2007.

[130] S. Han, *et al.*, "Template-free directional growth of single-walled carbon nanotubes on a- and r-plane sapphire," *Journal of the American Chemical Society,* vol. 127, pp. 5294-5295, Apr 20 2005.

[131] X. L. Liu, *et al.*, "Novel nanotube-on-insulator (NOI) approach toward single-walled carbon nanotube devices," *Nano Letters,* vol. 6, pp. 34-39, Jan 2006.

[132] N. Patil, *et al.*, "Wafer-Scale Growth and Transfer of Aligned Single-Walled Carbon Nanotubes," *IEEE Transactions on Nanotechnology,* vol. 8, pp. 498-504, Jul 2009.

[133] Y. G. Zhang, *et al.*, "Electric-field-directed growth of aligned single-walled carbon nanotubes," *Applied Physics Letters,* vol. 79, pp. 3155-3157, Nov 5 2001.

[134] A. Krishnan, *et al.*, "Young's modulus of single-walled nanotubes," *Physical Review B,* vol. 58, pp. 14013-14019, Nov 15 1998.

[135] S. M. Bachilo, *et al.*, "Structure-assigned optical spectra of single-walled carbon nanotubes," *Science,* vol. 298, pp. 2361-2366, Dec 20 2002.

[136] P. R. Wallace, "The Band Theory of Graphite," *Physical Review,* vol. 71, pp. 476-476, 1947.

[137] F. Wang, *et al.*, "Gate-variable optical transitions in graphene," *Science,* vol. 320, pp. 206-9, Apr 11 2008.

[138] Y. Zhang, *et al.*, "Direct observation of a widely tunable bandgap in bilayer graphene," *Nature,* vol. 459, pp. 820-3, Jun 11 2009.

[139] C. Lee, *et al.*, "Measurement of the elastic properties and intrinsic strength of monolayer graphene," *Science,* vol. 321, pp. 385-8, Jul 18 2008.

[140] K. S. Kim, *et al.*, "Large-scale pattern growth of graphene films for stretchable transparent electrodes," *Nature,* vol. 457, pp. 706-10, Feb 5 2009.

[141] X. Li, *et al.*, "Large-area synthesis of high-quality and uniform graphene films on copper foils," *Science,* vol. 324, pp. 1312-4, Jun 5 2009.

[142] Q. K. Yu, *et al.*, "Graphene segregated on Ni surfaces and transferred to insulators," *Applied Physics Letters,* vol. 93, pp. -, Sep 15 2008.

[143] T. Ohta, *et al.*, "Controlling the electronic structure of bilayer graphene," *Science,* vol. 313, pp. 951-954, Aug 18 2006.

[144] A. C. Ferrari, *et al.*, "Raman spectrum of graphene and graphene layers," *Physical Review Letters,* vol. 97, pp. -, Nov 3 2006.

[145] J. H. Hafner, *et al.*, "Catalytic growth of single-wall carbon nanotubes from metal particles," *Chemical Physics Letters,* vol. 296, pp. 195-202, Oct 30 1998.

[146] S. Huang, *et al.*, "Growth mechanism of oriented long single walled carbon nanotubes using “fast-heating” chemical vapor deposition process," *Nano Letters,* vol. 4, pp. 1025-1028, 2004.

[147] E. Joselevich, *et al.*, "Self-organized nanotube serpentines," *Nature Nanotechnology,* vol. 3, pp. 195-200, Apr 2008.

[148] C. W. Zhou, *et al.*, "Synthesis and device applications of high-density aligned carbon nanotubes using low-pressure chemical vapor deposition and stacked multiple transfer," *Nano Research,* vol. 3, pp. 831-842, Dec 2010.

[149] Y. G. Yao, *et al.*, "Temperature-mediated growth of single-walled carbon-nanotube intramolecular junctions," *Nature Materials,* vol. 6, pp. 283-286, Apr 2007.

[150] S. Bandow*, et al.*, "Effect of the growth temperature on the diameter distribution and chirality of single-wall carbon nanotubes," *Physical Review Letters,* vol. 80, pp. 3779-3782, Apr 27 1998.

[151] C. L. Cheung*, et al.*, "Diameter-controlled synthesis of carbon nanotubes," *Journal of Physical Chemistry B,* vol. 106, pp. 2429-2433, Mar 14 2002.

[152] M. Kumar and Y. Ando, "Chemical Vapor Deposition of Carbon Nanotubes: A Review on Growth Mechanism and Mass Production," *Journal of Nanoscience and Nanotechnology,* vol. 10, pp. 3739-3758, Jun 2010.

[153] N. J. Arfsten, "Sol-Gel Derived Transparent Ir-Reflecting Ito Semiconductor Coatings and Future Applications," *Journal of Non-Crystalline Solids,* vol. 63, pp. 243-249, 1984.

[154] B. G. Lewis and D. C. Paine, "Applications and processing of transparent conducting oxides," *MRS bulletin,* vol. 25, pp. 22-27, 2000.